Are seasonal deposits in spring at the Martian North Pole much shallower than previously thought?

Haifeng Xiao[1], Yuchi Xiao[2], Shu Su[1], Frédéric Schmidt[3,4], Luisa M. Lara[5], Pedro J. Gutierrez[5]

[1]Institute of Geodesy and Geoinformation Science, Technische Universität Berlin, 10553 Berlin, Germany
[2]School of Mechanical Engineering and Electronic Information, China University of Geosciences (CUG), 430074 Wuhan, China
[3]Université Paris-Saclay, CNRS, GEOPS, 91405 Orsay, France
[4]Institut Universitaire de France (IUF), 75231 Paris, France
[5]Instituto de Astrofísica de Andalucía (IAA-CSIC), 18008 Granada, Spain

Key Points:

- We propose to examine the shadow variations of the ice blocks at the Martian North Pole to infer the thickness of the seasonal deposits
- Maximum thickness of the seasonal deposits at the study scarp in MY31 is 1.63±0.22 m to which snowfalls contribute 0.97±0.13 m
- Seasonal deposits at the study scarp are up to 0.8 m shallower than previous measurements during spring

Corresponding author: Haifeng Xiao, Yuchi Xiao, haifengxiao1991@gmail.com; yuchi_xiao@cug.edu.cn

Abstract

The seasonal deposition and sublimation of CO_2 constitute a major element in the Martian volatile cycle. Here, we propose to use the shadow variations of the ice blocks at the foot of the steep scarps of the North Polar Layered Deposits (NPLDs) to infer the vertical evolution of the seasonal deposits at high polar latitudes. We conduct an experiment at a steep scarp centered at (85.0°N, 151.5°E). We show that the average thickness of the seasonal deposits due to snowfalls in Mars Year 31 is 0.97±0.13 m at Ls = 350.7° in late winter, which then gradually decreases in springtime. The large snow depth measured makes us wonder if snowfalls are more frequent and violent than previously thought. Meanwhile, we show that the average frost thickness due to direct condensation in Mars Year 31 reaches 0.64±0.18 m at Ls = 350.7° in late winter and quasi-linearly decreases towards the summer solstice. Combined, the total thickness of the seasonal cover in Mars Year 31 reaches 1.63±0.22 m at Ls = 350.7° in late winter, continuously decreases to 0.45±0.06 m at Ls = 42.8° in middle spring and 0.06±0.05 m at Ls = 69.6° in late spring. These estimates are up to 0.8 m lower than the existing MOLA results during the spring, which can be mainly attributed to MOLA-related biases. In terms of interannual variations, we observe that snow in the very early spring of Mars Year 36 can be 0.36±0.13 m deeper than that in Mars Year 31.

Plain Language Summary

Like Earth, Mars also has seasons. Up to one third of the atmosphere's CO_2 is exchanging with the polar regions through seasonal deposition/sublimation processes. At the steep scarps of the North Polar Layered Deposits (NPLDs), ice fractures can detach and fall to form ice blocks. We propose to use variations in the shadows of these ice blocks, observed in the High Resolution Imaging Science Experiment (HiRISE) images, to infer the thickness evolution of the seasonal deposits. We show that the average thickness of snowfalls at a study scarp is around 1 m in late winter in Mars Year 31. Meanwhile, we show that the average thickness of frosts directly condensed onto the surface reaches ∼0.6 m in late winter and quasi-linearly decreases towards late spring. Combining these two aspects, the gross thickness reaches ∼1.6 m in late winter, decreases to ∼0.4 m in middle spring, and further declines to ∼0.1 m in late spring. Surprisingly, these estimates are up to 0.8 m lower than the existing results during the springtime. It is expected that these proposed approaches can enable us to put important constraints on the Martian volatile cycles.

1 Introduction

Three billion years ago, when life emerged on Earth, the climate of Mars could have been with a thick atmosphere and a circumpolar ocean of liquid water in the northern hemisphere (Head III et al., 1999; Schmidt et al., 2022). Unfortunately, present Mars is barren and arid with

almost all water exists as ice, though it also exists in small quantities as vapor in the atmosphere. The Martian Polar Layered Deposits (PLDs) are predominantly pure water ice accumulated due to periodic orbital forcing (Laskar et al., 2002; Becerra et al., 2017), with a diameter of 1,000 km across and a thickness of a few kilometers (Plaut et al., 2007; Nerozzi & Holt, 2019). The spiral troughs that dissect the deposits contain thousands of visible ice layers with varying ratio of dust that record the Martian climate history in the Late Amazonian (Grima et al., 2009; Becerra et al., 2017). Carving of the troughs are probably related to prevailing katabatic winds that spiral due to the Coriolis effects. The PLDs, together with outlying crater ice deposits (Sori et al., 2022; McGlasson et al., 2023), are the most accessible and complete planetary climate records, making them among the most compelling science targets in the Solar System (I. B. Smith et al., 2020; Becerra et al., 2021). On the steep scarps at the margins of the North Polar Layered Deposits (NPLDs), mass-wasting processes like dust-ice avalanches and ice block falls have been frequently observed (Russell et al., 2008; Fanara et al., 2020b; Su, Fanara, Zhang, et al., 2023; Su, Fanara, Xiao, et al., 2023). The latter is in the form of scattered ice blocks and accumulating apron-like debris at the foot of the scarps. These phenomena represent multiple alternative modes of erosion in addition to sublimation, which are held accountable for mass losses of the polar ice caps. Mass loss rate due to these phenomena can compete with the outward motion due to viscous deformation to shape the NPLDs' rheology and evolution (Sori et al., 2015; Fanara et al., 2020b). In terms of the ice blocks, ice fragments that fall from the steep scarps are mainly protrusions that break due to structural failure once being subject to internal/external triggers, for example, thermal expansion/contraction and then stress-induced polygonal fracturing, the loading/removal of the topping seasonal deposits (Xiao, Stark, Schmidt, Hao, Steinbrügge, et al., 2022), or even the downward katabatic winds (Byrne et al., 2017).

Due to its obliquity (∼25° compared to 23.5° of Earth), there exist seasons on Mars as the planet orbits the Sun. When temperature drops below the CO_2 condensation point (approximately 148 K at average Martian surface pressure, but can range from 130 K to 154 K depending on elevation and season) in the fall and winter, the CO_2 solidifies and accumulates as snow or frosts in the polar regions. Then when the temperature increases during spring, these deposits sublimate into the atmosphere. Each Martian year, up to one third of the atmospheric CO_2 is involved in the seasonal deposition/sublimation process (Leighton & Murray, 1966). There exist two depositional mechanisms, that is, atmospheric precipitation as snowfalls and direct surface condensation as frosts (Määttänen & Montmessin, 2021). The resultant Seasonal South/North Polar Caps (SSPC, SNPC) can laterally extend down to 50°S/N in the beginning of winter under current conditions (Piqueux et al., 2015). Understanding these seasonal processes can place vital constrains on the Martian volatile cycles, and help with determination of the current mass balance of the polar ice reservoirs (Becerra et al., 2021). The thickness of the surficial layer would have important implications for the feasibility or trafficability of future landers, rovers, or helicopters that would drill into the PLDs and decipher the stored paleoclimate of Mars (I. B. Smith et al., 2020; Matthies et al., 2022). Through Mars Climate Sounder (MCS) observations, it is

now believed that water ice particles in the atmosphere can act as condensation nuclei onto which the CO_2 ice condenses and be deposited onto the polar caps along with the CO_2 snowfalls (Alsaeed & Hayne, 2022). Thus, by constraining the quantities of the CO_2 snowfalls, we can also gain insights into the amount of water that can be annually removed from the atmosphere through this scavenging process. These information can also help to determine the current mass balance of the residual north polar cap, that is, whether it is accumulating or ablating. Dynamic geological phenomena associated with sublimation of the SSPC/SNPC, for example, dark fans, polygonal cracks, spiders (South Pole)/furrows (North Pole), and alcoves in the dune fields, can be better modeled and interpreted given meaningful thickness evolution measurements of the overlying seasonal layer (for example, Portyankina et al., 2010; Hansen et al., 2013; Schmidt & Portyankina, 2018; Dundas et al., 2021; Mc Keown et al., 2023). Meanwhile, the amount of mass being seasonally added and removed from the surface is enough to induce significant elastic displacements of the lithosphere (Métivier et al., 2008). Characterizing these displacements through use of current altimetry or future dedicated geodetic missions can place important constraints on the current thermal and rheologic state of the Martian interior (Wagner et al., 2023). The changing mass loads can also cause small but measurable effects on Mars gravity and – through changing mass distribution and moments of inertia – rotation (that is, nutation, polar motion, and length of day variation; Defraigne et al., 2000; Van den Acker et al., 2002; Le Maistre et al., 2023).

The direct depth variation measurements of the seasonal deposits have been made by exploiting dynamic Mars Orbiter Laser Altimeter (MOLA) elevation profiles (D. E. Smith et al., 2001; Aharonson et al., 2004; Xiao, Stark, Schmidt, Hao, Su, et al., 2022; Xiao, Stark, Schmidt, Hao, Steinbrügge, et al., 2022). The MOLA estimates can be easily extended to cover the entire polar regions. D. E. Smith et al. (2001) calculated the height differences of the MOLA heights to median-filtered reference surface at various latitudinal annuli and measured the maximum thickness to be ∼1 m at both poles. Aharonson et al. (2004) fitted sinusoidal curves to the height differences obtained at locations where two MOLA profiles intersect, that is, cross-overs, and estimated the maximum depth variations to be ∼1.5 m at the North Pole and ∼2.5 m at the South Pole. Recently, by reprocessing the MOLA profiles and self-registering them (Xiao, Stark, Steinbrügge, et al., 2022; Xiao, Stark, Steinbrügge, et al., 2021), Xiao, Stark, Schmidt, Hao, Su, et al. (2022); Xiao, Stark, Schmidt, Hao, Steinbrügge, et al. (2022) derived both spatial and temporal thickness variations of the seasonal polar caps with a maximum of about 2.5 m at the south and 1.3 m at the north. In particular, they brought attention to abnormal behavior of the SNPC over the extensive linear dune fields at Olympia Undae, where maximum thickness variations up to 4 m and significant off-season increases and decreases up to 3 m in magnitude have been spotted. Olympia Undae, which roughly spreads from 78°N to 83°N in latitude and 120°E to 240°E in longitude (refer to Figure 4 for its location), is the largest continuous dune field on Mars, with dune percentage coverage typically greater than 80% (Hayward et al., 2010). It is a part of the vast circumpolar dark dune fields that surround the permanent north polar cap,

which are also referred to as the polar erg. However, it should be noted that the MOLA dataset is temporally limited to MY24 and MY25, impeding it to resolve inter-annual changes in the seasonal snow/ice depth.

Andrieu et al. (2018) applied Bayesian inversion techniques involving a radiative transfer model to constrain the impurity content and depth of the SSPC at a dune field of Richardson Crater (72°S, 180°W), and a maximum thickness of ∼0.4 m was found in early southern spring. Currently, they are trying to extend the measurements to the SSPC over the "cryptic region" where features translucent CO_2 slab ice and cold-jetting during the southern spring (refer to Hansen et al. (2010) for the location of this enigmatic region). Raguso & Nunes (2021) performed advanced radar processing techniques to the SHadow RADar (SHARAD) dataset to garner the best possible resolution and Signal-to-Noise Ratio (SNR) and co-registered the subsurface reflectors for estimation of the two-way time delay differences, hence the thickness of the Martian seasonal layer. Unlike MOLA, these measurements were not affected by ephemeris errors of the spacecraft but can be biased by possible presence of slope differential between the surface and the subsurface reference reflectors. Unfortunately, the experimental results are currently unavailable and extension to other regions with rougher surfaces and less distinct subsurface reflectors can be difficult.

Another viable way is to relate the rock shadow length changes in high-resolution optical images to that of the snow/ice depth. The High Resolution Imaging Science Experiment (HiRISE) camera on-board the NASA's Mars Reconnaissance Orbiter (MRO) operates in visible wavelengths, and with a telescopic lens that produces images at resolutions (0.25 m – 1.3 m) never before seen in planetary exploration missions (McEwen, 2005; McEwen et al., 2007). This high-resolution can enable accurate identification of rocks as small as 0.7 m in diameter. The spacecraft operates in a near sun-synchronous orbit, providing images of similar solar azimuth, beneficial for comparison of the shadow lengths that indicates snow/ice depth variations. A HiRISE Digital Elevation Model (DEM) can be derived from a geometric stereo pair acquired on different orbits so that a moderate convergence angle between the two viewing directions is formed (∼10° – ∼25°, McEwen et al., 2007). The camera started to continuously acquire high-resolution pictures of targeted regions on 29 September 2006, obtaining 5 – 20 observations per day, which has led to a high-cadence time series of imagery. Cull et al. (2010) utilized HiRISE images to show that the CO_2 snow/ice thickness reduced from ∼30 cm in early spring to less than 5 cm by middle spring at the Mars Phoenix landing site (68.22°N, 125.70°W). Mount & Titus (2015) also used rock shadow measurements in HiRISE images to infer the seasonal snow/ice depth at three sites of distinct morphologies (at latitudes between 68°N and 75°N). They showed that the effects of moats (circumferential shadows around rocks during springtime) and crowns (accumulation of snow/ice on the tops of rocks) can significantly modify rock shadow measurements and hence snow/ice depth (refer to Figure 3 of Mount & Titus (2015) for a schematic). Therefore, they applied an empirical model for correction and performed error propagation analy-

sis to reflect the uncertainty in the measurements. These snow/ice depth measurements were then combined with visible and thermal observations to calculate the bulk density of the seasonal ice cover over time. Despite its high precision, this approach can be spatially limited to fields where rocks are present on the surface. Unfortunately, at high polar latitudes where maximum snow/ice accumulation happens, rocks are unavailable for the purposes of looking into the seasonal snow/ice thickness evolution.

As aforementioned, the only existing measurement of the seasonal snow/ice depth variations at high latitudes come from MOLA records, which date back to MY24/25. Here, we propose to use shadows of the ice blocks at the foot of the steep scarps as observed in the HiRISE images, complementing that of the rocks, as an alternative way to infer the depth of the seasonal deposits. We show how to relate the length of the ice block shadows to its height using a rigorous geometric model, which is based on orthorectified images and takes both the solar and surface properties into consideration. Building on this model, we present two independent and complementary approaches to shed light on the thickness evolution of the ephemeral deposits: (1) "SUBTRACTing" that subtracts the ice block heights measured in the summer when free of seasonal cover to that in the spring; (2) "BOUNDing" that locates ice blocks that have been completely covered to place lower limits on the thickness of the seasonal deposits, and ice blocks that have not been completely submerged to put upper limits. We carry out the experiments at a scarp centered at (85.0°N, 151.5°E) and show the feasibility of these applications. We note that while "SUBTRACTing" is temporally limited to mid-to-late spring, "BOUNDing" is capable of yielding measurements in late winter and early spring. Beginning in late northern summer, thin haze rapidly develops into the thick water ice clouds known as the polar hood. The polar hood can last from late summer, fall, and all the way to winter, and even early spring (Benson et al., 2011; Navarro et al., 2014; Calvin et al., 2015; Brown et al., 2016). Fortunately, plenty of unobscured HiRISE images are available during late winter and early spring. During experiments with these proposed methods, we observe that moats do not exist around the ice blocks and the depth of the crowns over the ice blocks quasi-linearly decreases to zero when the seasonal deposits completely sublimate back into the atmosphere. Thus, the empirical correction scheme described in Mount & Titus (2015), that by adding the snow/ice thickness increases between consecutive seasons to all prior-season thicknesses, can be inapplicable in our case. We hence make reasonable assumptions and propose to use the widening of the ice blocks as a proxy to approximate and correct for the depth of the crowns over the ice blocks. These assumptions also enable us to decompose the contributions of the snowfalls and direct condensation to the thickness of the seasonal ice deposits and estimate them separately. Our ultimate goal is to apply these approaches to all active scarps at high polar latitudes, and rock fields at lower polar latitudes, to obtain good samplings of the vertical evolution of the SNPC. The expected results can also serve as ground truth to calibrate existing MOLA results and validate contemporary anticipated SHARAD results.

The paper is structured as follows: In Section 2, bundle adjustment and orthorectification of the HiRISE images are introduced. Based on the orthorectified images, the shadowing model of ice blocks resting at the foot of the steep scarps is presented, and the "SUBTRACTing" and "BOUNDing" approaches to obtain thickness evolution of the SNPC are described. The study scarp centered at (85.0°N, 151.5°E) is introduced in Section 3. These are followed by the application of the two independent approaches to ice blocks at the study scarp (Section 4). After that, precision of the "SUBTRACTing" results, automation of the "BOUNDing" approach, interannual variations of snowfalls, estimation and correction for direct condensation effects, possible biases in the MOLA-derived thicknesses, comparison of measured snowfall thickness to that predicted by a snowing model, and prospects of future work are successively presented in Section 5. Finally, conclusions are drawn in Section 6.

2 Methods

To correctly relate an ice block's shadow length to its height, bundle adjustment and subsequent orthorectification of the images should be implemented to remove the image distortions due to oblique viewing angle and topographic relief. For orthorectification to be carried out, a precise DEM has to be made using image matching of the bundle-adjusted stereo pairs. Previous studies using the objects' shadows to infer their heights focused on relatively flat regions without significant undulations and thus assumed the surface to be a horizontal plane (for example, Blackburn et al., 2010; Cull et al., 2010; Mount & Titus, 2015; P. C. Thomas et al., 2016). However, in our case, the slopes in the regions where ice blocks reside in the Basal Unit outcrops, immediately underlying the NPLDs, are significant (up to ∼30°) and have to be considered in the shadowing geometry. The established shadowing model is then used in the proposed "SUBTRACTing" and "BOUNDing" approaches to determine the thickness evolution of the seasonal deposits.

2.1 Bundle adjustment, DEM generation, and image orthorectification

We use the raw and unprocessed HiRISE images, that is, the Experimental Data Record (EDR) products, to do bundle adjustment and produce a DEM of the study region using a stereo pair and the Ames Stereo Pipeline (ASP) software (Beyer et al., 2018; Hepburn et al., 2019). This DEM is then used to orthorectify all the available images. We note that Reduced Data Record (RDR) products also exist that are radiometrically-corrected images resampled to a standard map projection. However, these RDR images lack the required geometric stability for stereo processing. The sequential procedures applied are: (1) Mosaicking the individual 10 Charged-Coupled Devices (CCDs) together to single images which includes de-jittering and radio-calibration; (2) Bundle adjusting all available images to correct for errors in camera position and orientation (extrinsics only) and make them internally consistent. Feature points are matched across images. A feature point can be identified in multiple overlapping images, it is equivalent to the

concept that a bundle of light rays can intersect at a single triangulated point on the ground. In reality, the intersection can be imperfect due to residual errors. In bundle adjustment, each triangulated ground point is projected back into the cameras. Then, the sum of squares of residuals between the pixel coordinates of the feature points and the locations of the projected points, that is, reprojection errors, are minimized through a robust least squares solver:

$$\{\hat{\mathbf{R}}, \hat{\mathbf{t}}, \hat{\mathbf{P}}\} = \min \sum_{i=1}^{n} \sum_{j=1}^{m} \left(\mathbf{u}_{ij} - \pi\left(\mathbf{C}_j, \mathbf{R}_j \mathbf{P}_i + \mathbf{t}_j\right)\right)^2 , \tag{1}$$

where $\mathbf{u}_{ij}$ is the observed tie point image coordinate in pixel, $\mathbf{P}_i$ is the 3D coordinate of the i^{th} ground point (a total of n), and $\mathbf{C}_j$ is the center coordinate of the j^{th} camera (a total of m). Meanwhile, $\mathbf{R_j}$ and $\mathbf{t_j}$ denote the rotation and translation operations to the j^{th} camera, $\pi\left(\mathbf{C}_j, \mathbf{R_j}\mathbf{P}_i + \mathbf{t}_j\right)$ is the reprojection operator that obtains the reprojected image coordinate in pixel of the ground point. Parameters to be adjusted are listed on the left of the equation; (3) Locating conjugate feature points through image matching techniques and derive corresponding disparity values. Sub-pixel correlation in image matching is performed to refine the disparity map, which is then converted to heights of the object ground points; (4) Gridding the point cloud of object heights to a DEM. This DEM is then applied to orthorectify all of the HiRISE images in the depositional area of the ice blocks. We note that the bundle adjustment lacks absolute ground control points and only tie points are used to improve the internal consistency of the images. As a result, there can exist lateral shifts between the DEMs generated in Su, Fanara, Zhang, et al. (2023) using stereo pairs from previous bundle-adjustment and the images from the bundle adjustment in this study. For more details of these processes, refer to the pipeline explained in Su, Fanara, Zhang, et al. (2023).

2.2 Relating the height of an ice block to its shadow length

Figure 1 shows the schematic on the shadowing geometry that we utilize to establish the relationship between the height of the Ice Block (H) and the measured length of the cast shadow as seen in an orthorectified HiRISE image (OPs'). The solar elevation angle is α, while the slope is β. We align the local coordinate system with the bearing of the sloped plane ($O-ABC$). The angle ω measures the angular separation between the sunlight and the orientation of the slope. Without considering the slope, the Ice Block in question casts a shadow OPh on the horizontal plane, coordinates of which can be written as

$$\begin{cases} x\_Ph = H \dfrac{\sin\omega}{\tan\alpha\cos\beta} \\ y\_Ph = H \dfrac{\cos\omega}{\tan\alpha\cos\beta} \end{cases} . \tag{2}$$

Now, we consider the existence of the sloped plane and assume the intersection point of the light over the tip of the Ice Block with the sloped plane to be Ps. As Ps has to be somewhere be-

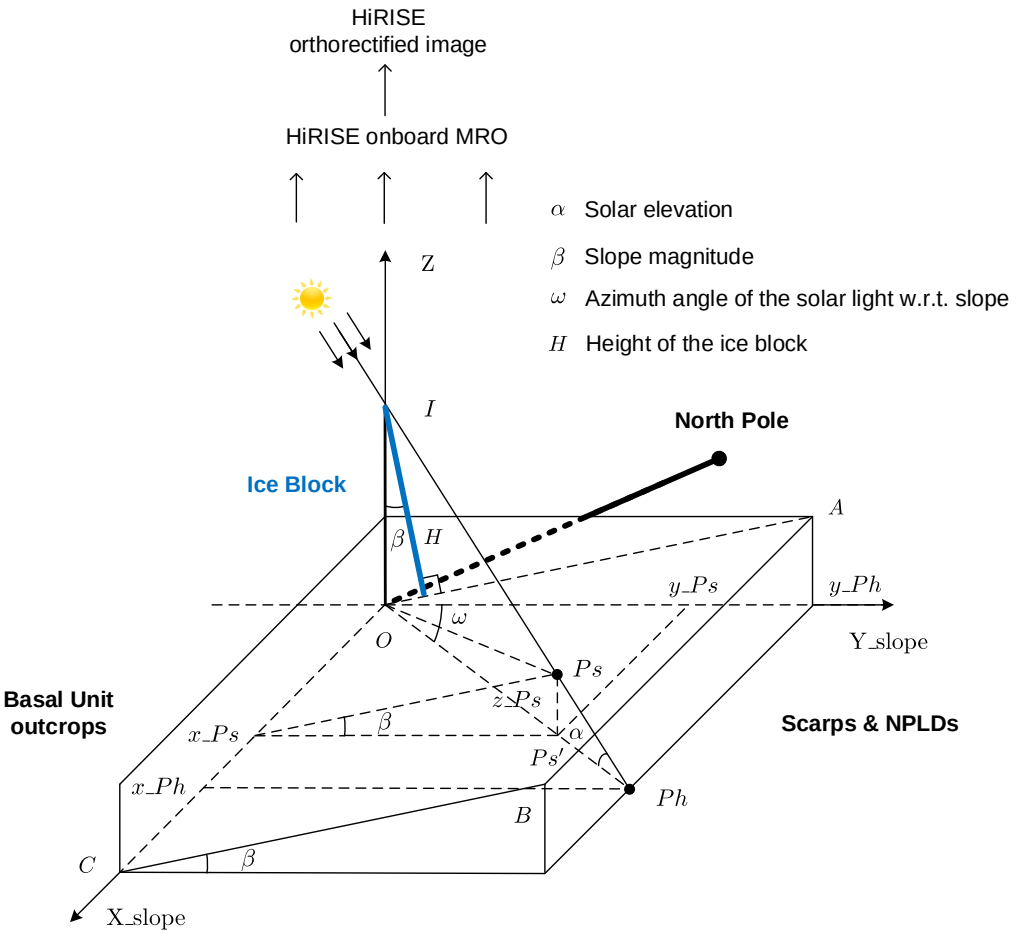

Figure 1: Geometry schematic that illustrates how the solar azimuth, elevation, magnitude and aspect of the slope affect the shadow of the Ice Block situated perpendicular to the slope plane $(O - ABC)$. Ph is the projected point of the Ice Block top onto the horizontal plane, while Ps is the top onto the inclined plane with a slope of β. The angle α denotes the elevation angle of the Sun. The angle ω represents the relative azimuth angle of the solar rays with respect to that of the slope.

275 tween I and Ph, its coordinates can be like

$$\begin{cases} x\_Ps = t \times H \dfrac{\sin\omega}{\tan\alpha\cos\beta} \\ y\_Ps = t \times H \dfrac{\cos\omega}{\tan\alpha\cos\beta} \\ z\_Ps = (1-t) \times H \dfrac{1}{\cos\beta} \end{cases}, \tag{3}$$

277 where t is a scalar between 0 and 1. As can be seen in Figure 1, the ratio of z_Ps and y_Ps
278 equals $\tan\beta$, which leads to

$$t = \frac{\tan\alpha}{\cos\omega\tan\beta + \tan\alpha}, \tag{4}$$

280 and the coordinates of the intersection point on the sloped plane can be written as

$$\begin{cases} x\_Ps = H \dfrac{\sin\omega}{\cos\omega\sin\beta + \tan\alpha\cos\beta} \\ y\_Ps = H \dfrac{\cos\omega}{\cos\omega\sin\beta + \tan\alpha\cos\beta} \\ z\_Ps = H \dfrac{\cos\omega\tan\beta}{\cos\omega\sin\beta + \tan\alpha\cos\beta} \end{cases}. \tag{5}$$

282 The length of the shadow on the slope as measured from the HiRISE orthorectified image is
283 then

$$L_S = \sqrt{x\_Ps^2 + y\_Ps^2} = \frac{H}{\cos\omega\sin\beta + \tan\alpha\cos\beta}. \tag{6}$$

285 Solar azimuth together with the elevation at the acquisition time of the HiRISE image
286 can be calculated by exploiting the information stored in the Spacecraft, Planet, Instrument,
287 Camera-matrix, and Events (SPICE) kernels (Acton, 1996). Specifically, we access `pck00009.tpc`
288 Planetary Constant Kernel for orientation and shape of Mars. Meanwhile, we use the `mar063.bsp`
289 file of the generic planet ephemeris to estimate relative position of Mars with respect to the Sun
290 at a given time stamp. Slope magnitude and aspect at the Ice Block's location can be approx-
291 imated by evaluating the elevation values within a 3×3 window in the HiRISE DEM gener-
292 ated in this study. The azimuthal difference of the solar illumination with respect to bearing
293 of the local slope, ω that falls within $[0°,\ 180°]$, can be related to the measured solar azimuth
294 (φ) and slope aspect (μ) as shown in Figure S1. For the north polar stereographic projection
295 centered at the North Pole, the projected body-fixed coordinates of the Ice Block with latitude
296 ϕ and longitude L can be written as

$$\begin{cases} x_{bf} = \dfrac{2R\cos\phi\sin L}{1+\sin\phi} \\ y_{bf} = \dfrac{2R\cos\phi\cos L}{1+\sin\phi} \end{cases}. \tag{7}$$

298 Once we know the map coordinates of the Ice Block, the analytical expression of ω can be de-
299 rived as follows:

$$\begin{aligned} \omega &= |\pi/2 - (\varphi - \varepsilon - \pi/2) - \mu| = \left|\pi - (\varphi - \arctan\frac{x_{bf}}{y_{bf}}) - \mu\right| \\ &= |\pi - (\varphi - (\pi - L)) - \mu| \\ &= |2\pi - \varphi - L - \mu|, \end{aligned} \tag{8}$$

301 where the angle ε denotes the intersection angle between the map north and the direction for
302 the Ice Block in question to the North Pole (Figure S1).

2.3 The "SUBTRACTing" approach

By measuring the shadow lengths of the ice blocks in the orthorectified images, combined with auxiliary information on the solar and slope conditions, we can infer the ice block heights above the snow/ice cover during spring or the bare ground surface during summer using Equation 6. As the HiRISE images can span eight Mars Years (MY), or more than 13 Earth years, during which the heights of the ice blocks can slowly shrink due to tumbling and aeolian erosion. Thus, we use the ice block heights obtained at the temporally adjacent northern summer as the reference to infer the depth of the seasonal cap in the springtime. When there exist multiple ice block height measurements within a single summer, their average is taken as the reference value, as a way to reduce measurement errors. See a detailed discussion in Section 5.1. Finally, acquired time-dependent depth values are plotted against the solar longitude for examination of their evolution patterns. Here, solar longitude (Ls) is used to express the seasonality on Mars and $0^\circ < \mathrm{Ls} < 90^\circ$ stands for northern spring, $90^\circ < \mathrm{Ls} < 180^\circ$ for northern summer, $180^\circ < \mathrm{Ls} < 270^\circ$ for northern fall, and $270^\circ < \mathrm{Ls} < 360^\circ$ for northern winter. We term this approach as "SUBTRACTing", as it basically subtracts the ice block heights measured in the summer to that measured in the spring to gauge the seasonal snow/ice depth in sprintime.

Criteria for selection of the ice blocks as a reference to invert for the thickness variations of the seasonal deposits are as follows: (1) Ice blocks are high enough as not to be submerged by the seasonal snow/ice; (2) Ice blocks shaped like triangular prisms are the ideal candidates. The shadows in these cases run parallel to the ridge lines of the ice blocks. Sticky ice blocks, and so their shadows, are also considered solid options. The peaks on the ice blocks and in their shadows are normally easy to identify. In both of these cases, the effects of accumulation of snow particles over the ice block tops are minimized. However, it should be noted that the formation of a layer on the tops of the ice blocks, that is crowning, due to direct condensation of frosts can still take place (Section 5.4); (3) The ice blocks can tumble under gravity of its own and the seasonal layer, or even be triggered by the katabatic winds down from the polar caps. Furthermore, erosion due to winds can slowly shrink the size of the ice blocks. Thus, it is required that the morphology of the ice blocks and their heights should not significantly change during the bracketing summers. For triangular-prism-like ice blocks, the lengths of the shadow are treated as the distances between the parallel block crest lines and shadow edge lines along the solar azimuth at the acquisition times of the images. For peaked ice blocks, the lengths of the shadow are measured as that of the lines connecting tips of the shadows and their corresponding points along the terminators, that is, boundary lines separating the sunlit and shadowed portions of the ice blocks. When the latter is blurry, then we fix the starting points of the measuring lines at the shadow tips, tweak them to be parallel to the solar azimuth, and determine their ending points as the intersections between the lines and the respective terminators.

2.4 The "BOUNDing" approach

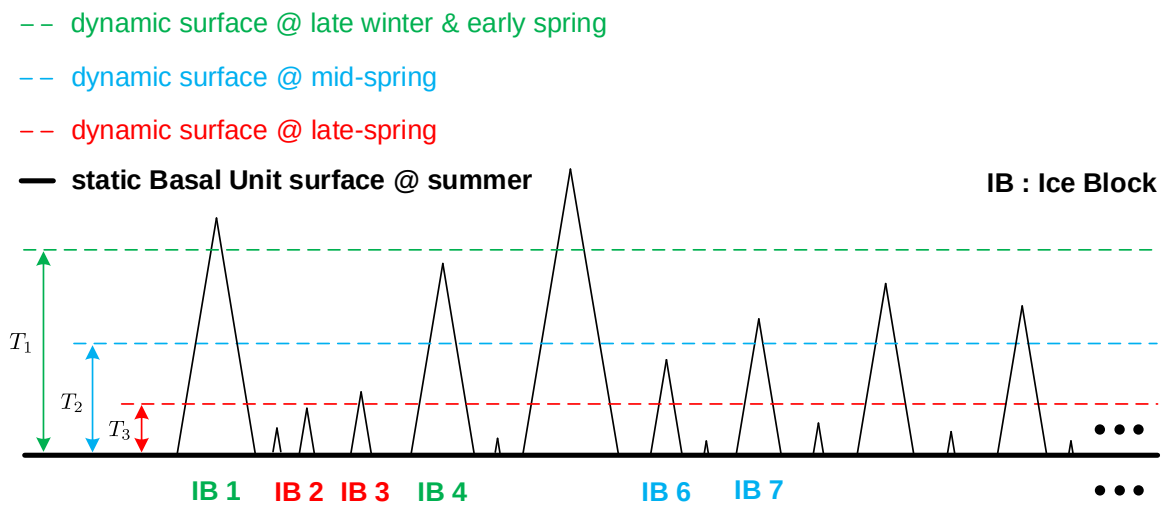

Figure 2: Illustration of an alternative and independent approach employed to constrain the depth of the seasonal deposits ("BOUNDing"). Instances of ice blocks of various sizes and heights are randomly placed over the Basal Unit. It should be noted that this plot is a simplified illustration as in reality smaller ice blocks are much more frequently observed than larger ones (Fanara et al., 2020b). Meanwhile, only peak-shaped ice blocks are presented so as we can assume no snow particles on top of the ice blocks. T_i denotes the varying thickness of the seasonal layer at different epochs.

Although HiRISE images without the impact of the polar hood can be acquired during late winter and early spring, the outlines of the shadows cannot be unambiguously identified due to unfavourable solar elevation angles, leading to failed application of the proposed "SUBTRACTing" approach. Meanwhile, the bundle adjustment can fail with images acquired in late winter or early spring as small-scale features stay covered by the thick seasonal deposits.

Here we devise an independent approach for measuring the depth of the seasonal deposits, which is capable of inferring the thickness during late winter and early spring (Figure 2). This approach takes advantage of relatively large quantity of ice blocks that cluster in specific regions (see the inset in Figure 5 for an example). The main idea behind it is that an ice block that has been completely covered means that the thickness of the seasonal layer exceeds the height of the ice block (a lower bound). Similarly, an ice block that has not been completely covered means that the thickness of the seasonal layer is lower than the ice block height (an upper bound). However, to place the strongest constraints, we have to locate the locally highest ice blocks that have been completely submerged and the locally lowest ice blocks that still

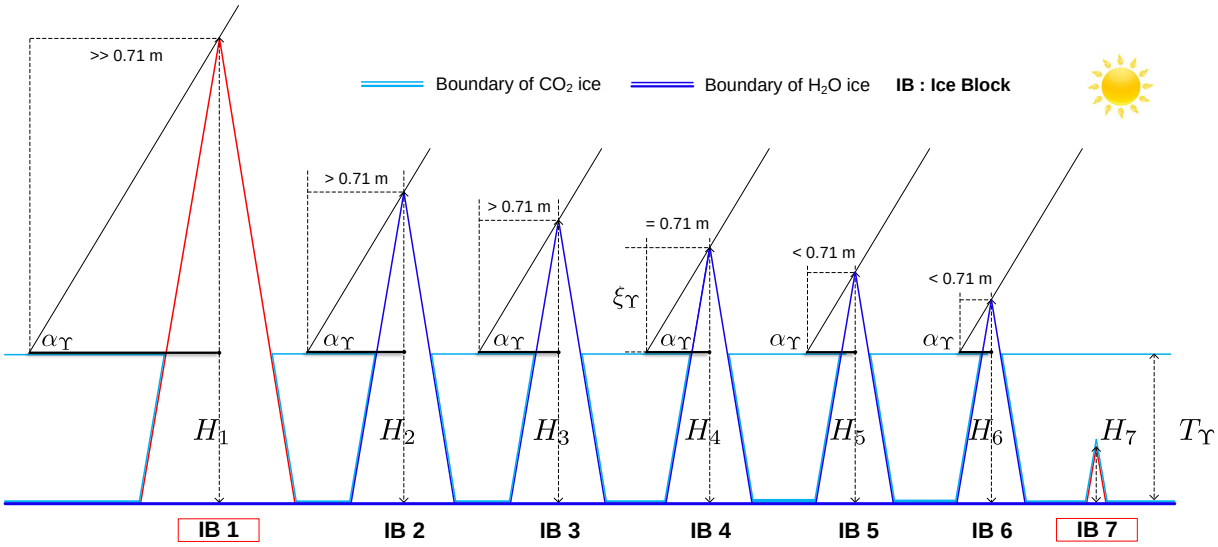

Figure 3: Schematic showing the offset inherited in the derived bounding constraints on the thickness of the seasonal layer at Ls = $\Upsilon°$ in late winter or spring from the "BOUNDing" approach. IBs 2 and 3 are examples of the locally smallest ice blocks visually determined to be uncovered by the seasonal layer to place upper bounds on its thickness (T_Υ). Meanwhile, IBs 5 and 6 are examples of the locally largest ice blocks visually identified to be completely covered with the aim to place the corresponding lower bounds. IBs 1 and 7 marked in red are representative ice blocks that are respectively too large and too small to put tight bounds on the thickness of the seasonal layer, which are thus not included in our analysis. The criterion by which we visually determine if an ice block is fully covered or not is if its shadow length is greater than the identification threshold of 2.83 pixels, or 0.71 m when the spatial resolution of the image is 0.25 m. Thus, the height of the bounding ice block during summertime (H_m, $m = 1, 2, 3, \cdots, 7$) always offsets the thickness of the seasonal deposits by a magnitude of ξ_Υ. This offset can be shown in the ideal case of IB 4 where its shadow length exactly equals the threshold of 2.83 pixels, which can then precisely constrain the seasonal deposits' thickness to be $T_\Upsilon = H_4 - \xi_\Upsilon$. The offset, that is $-\xi_\Upsilon$, can be related to the spatial resolution of the image and the solar elevation angle as in Equation 10. The boundaries for different types of ices are just for illustration purposes as there also exists directly condensed and CO_2-snowfall-scavenged water ice within the seasonal deposits (Appéré et al., 2011; Alsaeed & Hayne, 2022).

stick out the frozen layer. We only select peaked and triangular-prism-shaped ice blocks to minimize the impact of accumulation of snow particles over the ice blocks which otherwise can bias the thickness inversion (Section 5.4). As shown in Figure 2, snow/ice deposits are deepest in late winter and early spring with a thickness of T_1, then as the solar insolation increases with time, CO_2 starts to sublimate and the thickness starts to decline and reach T_2 at mid-spring and T_3 in late spring, respectively. Surface is free of the seasonal layer during the adjacent summer where the heights of the ice blocks can be measured using the geometric model presented in Section 2.2. For T_1, we can utilize IBs 4 and 1 to place the lower and upper bounds, respectively. IB 4 is the locally highest ice block that has been completely covered during late winter and early spring, and IB 1 is the locally lowest ice block that has not been completely submerged. In a similar way, we can locate the ice blocks, marked using corresponding colors in Figure 2, to place bounds on T_2 and T_3, respectively. The mathematical expressions can be put as follows:

$$\begin{cases} T_1 \in [\, H_4,\, H_1 \,] \\ T_2 \in [\, H_6,\, H_7 \,] \\ T_3 \in [\, H_2,\, H_3 \,] \end{cases}, \tag{9}$$

where H_{m} denotes the height of IB m measured in the adjacent summer. We term this alternative approach as "BOUNDing" for simplicity and to distinct it from the "SUBTRACTing" approach that subtracts the ice block heights in the summer to that in the spring (Sections 2.3).

Attention should be drawn to the fact that the pixel size of HiRISE (down to 0.25 m) limits the detection of shadows under 0.71 m in length ($2\sqrt{2} = 2.83$ pixels). As such, when we determine a locally shortest ice block that has not been completely submerged or a locally tallest ice block that has been completely covered, it has already stuck out the seasonal layer at least or at most by

$$\xi_{\Upsilon} = 2\sqrt{2} \times sr \times \tan \alpha_{\Upsilon} \,. \tag{10}$$

Here, ξ_{Υ} denotes magnitude of the offset at Ls $= \Upsilon^{\circ}$ during late winter or spring. The variable sr represents the spatial resolution of the images which is mostly 0.25 m but can also be 0.5 m for that acquired in late winter and early spring. The symbol α_{Υ} denotes the solar elevation angle at the acquisition of the image with seasonal snow/ice cover. A schematic illustrating the offset is shown in Figure 3. We correct the derived thickness bounds for the offset of $-\xi_{\Upsilon}$ otherwise they would be systematically higher than that derived from the "SUBTRACTing" approach.

For illustration purposes, abstract probability distributions of bounding constraints at specific solar longitudes are computed using the Kernel Density Estimation (KDE; Silverman, 1986). In our case, we perform the KDE process using the Gaussian kernel (κ) and use the Silverman's rule to compute an optimal bandwidth of σ to ensure moderate smoothness of the obtained den-

sity distribution:

$$\rho_\kappa(x) = \frac{1}{N\sigma}\sum_{i=1}^{N}\kappa\left(x - x_j;\sigma\right) \quad \text{with} \quad \kappa(x;\sigma) \propto \exp\left(-\frac{x^2}{2\sigma^2}\right), \tag{11}$$

where N is the total number of ice block height measurements, that is x_j, used to set upper or lower limits on the seasonal snow/ice depth. Violin plots are used for visualization purpose. We have also tried the Improved Sheather Jones (ISJ) algorithm for choosing the bandwidth which should be used when data is far from normal or multimodal (Botev et al., 2010). Unfortunately, the limited number of available constraints in our case prevents its effective application.

For statistically significant number of constraints, the thickness of the seasonal deposits at a specific solar longitude can be expected to fall within the interval formed by medians of the lower and upper bounds. To obtain more realistic uncertainty estimates, we take the standard errors of the median bounds into consideration using a scaled Median Absolute Deviation (SMAD; Leys et al., 2013). The SMAD is related to the median of the absolute deviations from the samples' median as

$$\mathrm{SMAD}_\Upsilon = sf \times \mathrm{Md}\left[\left|\mathbf{T}_\Upsilon - \mathrm{Md}\left[\mathbf{T}_\Upsilon\right]\right|\right], \tag{12}$$

where $\mathbf{T}_\Upsilon$ denotes the sample vector which contains all the thickness constraints at $\mathrm{Ls} = \Upsilon^\circ$ in late winter or spring, $\mathrm{Md}\left[\,\right]$ is the median operator, and $sf = 1.4826$ is the scale factor. The scaled metric can be treated as a consistent estimator similar to the standard deviation of a Gaussian distribution. We extend the median lower bound downwards and the median upper bound upwards to obtain the adjusted bounding range:

$$\Theta_\Upsilon^{\mathrm{T}} = \left[\mathrm{Md}_\Upsilon\_\mathrm{lb} - \frac{3\times\mathrm{SMAD}_\Upsilon\_\mathrm{lb}}{\sqrt{N_\Upsilon\_\mathrm{lb}}},\ \mathrm{Md}_\Upsilon\_\mathrm{ub} + \frac{3\times\mathrm{SMAD}_\Upsilon\_\mathrm{ub}}{\sqrt{N_\Upsilon\_\mathrm{ub}}}\right], \tag{13}$$

where $\mathrm{Md}_\Upsilon\_\mathrm{lb}$ and $\mathrm{Md}_\Upsilon\_\mathrm{ub}$ denote the medians of the lower and upper bounds at $\mathrm{Ls} = \Upsilon^\circ$, respectively. Meanwhile, N_Υ_lb and N_Υ_ub denote the number of available lower and upper bounds at $\mathrm{Ls} = \Upsilon^\circ$, respectively.

3 Study area

Ice blocks analyzed in this study lie at the bottom of an equator-facing steep scarp. The scarp is centered at (85.0°N, 151.5°E) with a total length of ~20 km (refer to its location in Figure 4). This scarp is the same as that studied in Su, Fanara, Zhang, et al. (2023) and termed Scarp 1. The scarp is visually distinguishable by its bright water ice layers (Figure 5). The relatively flat top of the NPLDs features a residual layer of mostly dust-free water ice and can grow to a few meters at most (Figure 4). Over the surface a homogeneous pitted texture at length scales of 10 to 20 m is revealed, which appears to be the result of differential sublimation. Fallen ice blocks from the steep scarp reside at the surface of the Basal Unit. A typical example of a clustering of ice blocks is shown in Figure 5. The Basal Unit is a low-albedo, interbedded sandy and icy deposits that lie stratigraphically below the NPLDs (Grima et al., 2009; T. Brothers

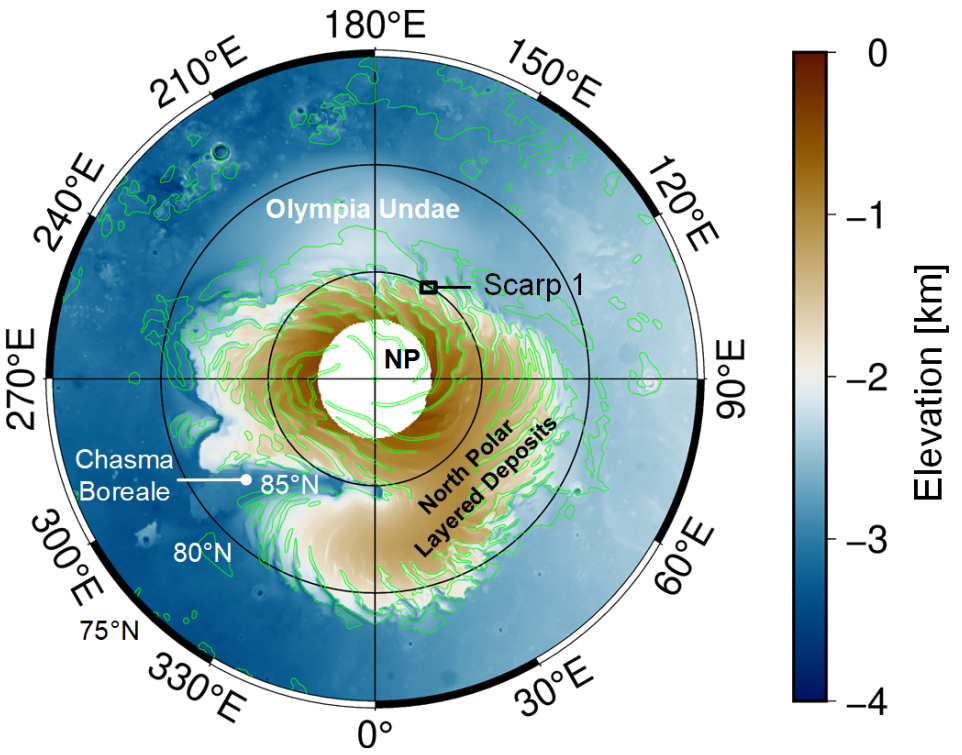

Figure 4: Topography of the Martian North Pole represented by the reference DEM from reprocessed and then self-registered MOLA altimetric profiles (Xiao, Stark, Schmidt, et al., 2021). The elevation is referenced to a Martian ellipsoid with an equatorial radius of 3,396.19 km and a mean polar radius of 3,376.20 km. The missing coverage poleward of 87°N is due to a lack of nadir-pointing profiles, a limitation related to the orbital inclination of the spacecraft. The map projection is north polar stereographic, with coverage poleward of 75°N and a spatial resolution of 1 km/pixel. The Residual North Polar Cap (green polygons), Chasma Boreale, and the study site (Scarp 1) are marked.

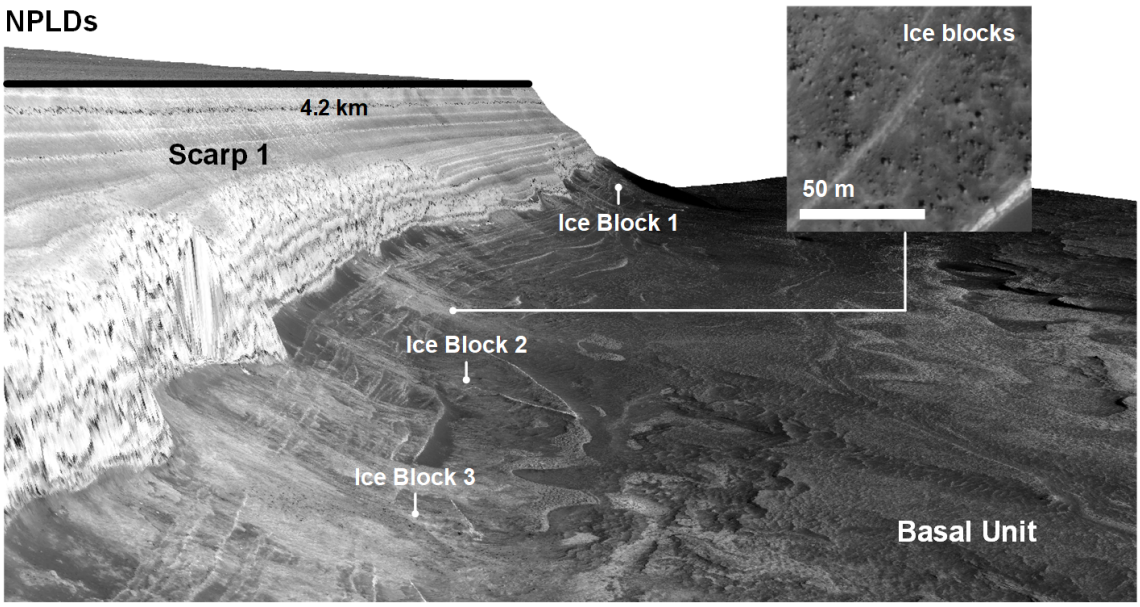

Figure 5: Illustration of the NPLDs and ice blocks at the foot of the steep scarp (Scarp 1) by a 3D view with the HiRISE image acquired during the summertime of MY29 (`PSP_009648_2650_RED`) draped on the HiRISE DEM generated in this study (no vertical exaggeration). Elevation difference from top of the NPLDs to the Basal Unit at the bottom is ∼600 m. Site is centered at (85.0°N, 151.5°E). Wide patches and aprons of debris are readily visible at the foot of the scarp. Inset map shows typical examples of ice blocks at foot of the scarp. It should be noted that the Basal Unit outcrops where ice blocks reside can still feature significant terrain slope (up to ∼30°). We mark the locations of Ice Blocks 1, 2, and 3 used for the purpose of this study. For reference, the distance between Ice Blocks 1 and 3 is 4,564 m.

et al., 2015), and may be one of the largest reservoirs of water-ice on Mars after the PLDs (Ojha et al., 2019). The Basal Unit outcrops beneath Scarp 1 belong to the Cavi unit where it transitions into the NPLDs (S. Brothers et al., 2018; Nerozzi et al., 2022). Although the majority of the ice blocks originate from steep scarps of the NPLDs, some of them can also source from the upper part of the Basal Unit with a slope of up to 30° (Su, Fanara, Zhang, et al., 2023).

4 Results

4.1 Bundle adjustment, DEM generation, and image orthorectification

A total of 50 images are available for Ice Blocks 1, 2, and 3 with a pixel size ranging from 0.25 m (39) to 0.50 m (11). Most of them (33) were acquired from 2010 to 2013 (MY30 – 32) with the earliest coverage extended to 2008 (MY29) and the latest ones taken during 2021 (MY36). These images are bundled adjusted all together. Unfortunately, the bundle adjustment fails to rectify 8 images acquired in late winter or early spring when the seasonal layer is thick, due to a lack of small-scale features and "distorted" feature shapes owning to distinct illumination conditions with respect to the rest of the images. Then, the stereo pair `ESP_018905_2650_RED` and `ESP_019222_2650_RED` acquired on 8 August 2010 and 2 September 2010 in the summer of MY30 is used to create a DEM (the same pair as used in Su, Fanara, Zhang, et al. (2023)). The stereo pair respectively imaged the Scarp 1 area with spacecraft rolls of $-3.6°$ and $-15.5°$ to achieve a good base-to-height ratio for the purpose of obtaining a reliable 3D model of the surface. The emission angles for these two images are 4.0° and 17.0°, respectively. These images were acquired relatively close in time, with an interval of 25 Earth days, which can minimize differences in solar illumination and surface properties between the stereo pairs. Similarities between the stereo pair can aid in the image matching and parallax determination processes to reconstruct the object heights. The DEM is gridded with 1×1 m pixels (Figure 5). Limited interpolation spikes and long lines due to CCD seams have been spotted while inspecting the hillshade generated from the DEM, verifying the correctness and reliability of the bundle adjustment and image matching processes. The bundled-adjusted images are then automatically orthorectified using the aforementioned DEM and used for measurements of the shadows. Visual examination of the orthorectified images show they mutually align well at their overlapping portions. In combination with solar conditions at the acquisition times of the images, local slope and aspect are extracted from this DEM for converting the shadow length variations to temporal thickness evolution of the seasonal CO_2 layer.

4.2 Snow/ice thickness in middle-to-late spring from "SUBTRACTing"

We identify three reference ice blocks at Scarp 1 for the purpose of measuring the seasonal snow/ice depth evolution at these specific spots. All of these three ice blocks meet the eligibility criteria. Meanwhile, they are capable of yielding the largest number of reliable and self-consistent thickness measurements among 10 candidates. The other ice blocks are not included in our anal-

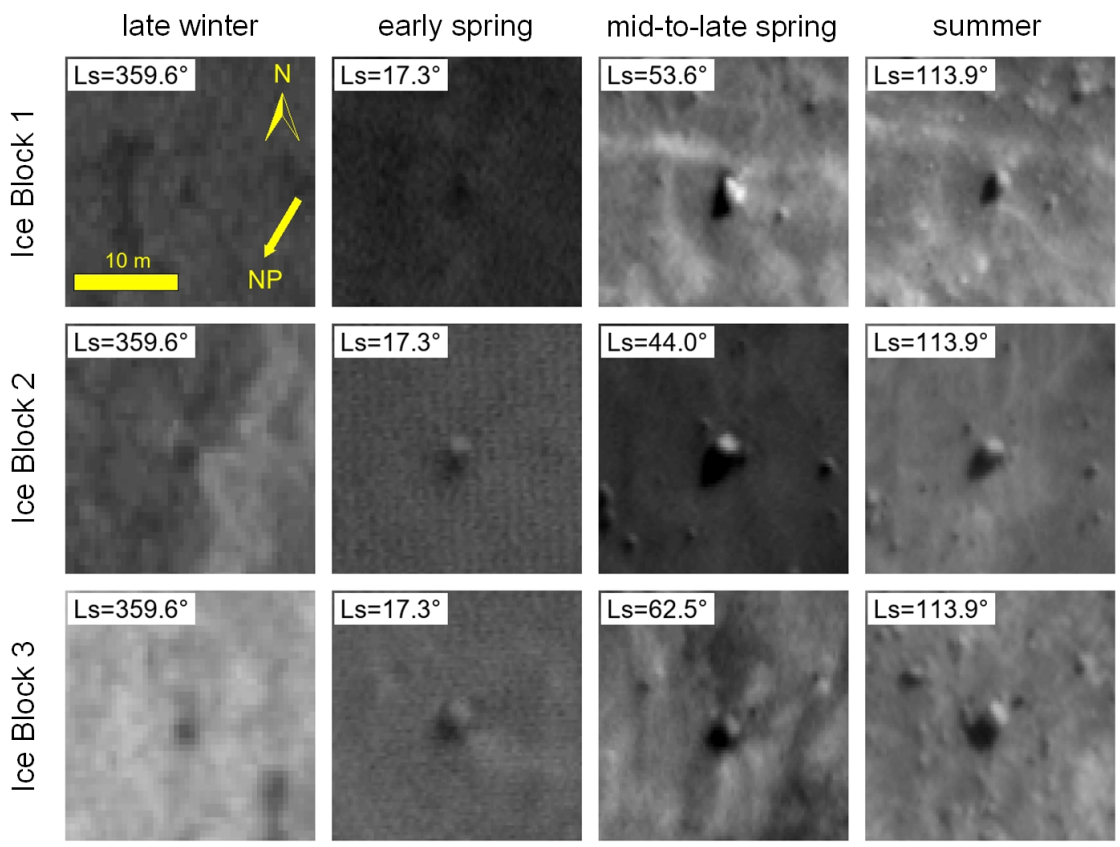

Figure 6: Images of Ice Blocks 1, 2, and 3 (centered at the sub-frames) during different seasons from late winter to summer. The images used are `ESP_032856_2650_RED` at Ls = 359.6° in MY31, `ESP_024509_2650_RED` at Ls = 17.3° in MY31, `ESP_016439_2650_RED` at Ls = 44.0° in MY30, `ESP_016716_2650_RED` at Ls = 53.6° in MY30, `ESP_034610_2650_RED` at Ls = 62.5° in MY32, and `ESP_053730_2650_RED` at Ls = 113.9° in MY34, respectively. The projection adopted is polar stereographic centered at the North Pole. The north of the projected map and direction to the North Pole are marked. Illumination is to the bottom-left corner. Note that ice blocks in springtime feature no circumferential shadows that are indicative of moating.

ysis due to large oscillations of the measured thicknesses there and wider temporal gaps between them. We term the selected three ice blocks as Ice Block 1 (84.984°N, 151.907°E), Ice Block 2 (85.006°N, 151.231°E), and Ice Block 3 (85.008°N, 151.072°E), respectively. Refer to Figure 5 for their locations. The distance between Ice Blocks 1 and 2 is 3,745 m, 832 m between Ice Blocks 2 and 3, and 4,564 m between Ice Blocks 1 and 3. Regional slope at Ice Blocks 1, 2, and 3 are around 11°, 2.5°, and 6°, which are generally gentle compared to that right at the foot of the scarp which can be up to 30°. This can be conceived as ice blocks tend to stop and reside where terrain is flat or when barricaded by obstacles along their paths. Typical HiRISE images of these ice blocks from late winter and spring, when the surface is covered with seasonal deposits, to summer, when the seasonal layer completely sublimates away, are shown in Figure 6. Ice Block 3 is triangular-prism-shaped while the other two feature clear peaks. Ice Blocks 1, 2, and 3 are relatively stable over MY29 to MY36, with average summer heights of ∼1.2 m, ∼1.4 m, and ∼1.8 m, respectively (Section 5.1). During late winter, with the Sun being less than ∼5° above the horizon, the CO_2 snow/ice is the thickest. Significant portion of the ice blocks are submerged by the seasonal deposits, and there exists no clear and unique identification of their cast shadows. This situation does not improve much at the very early of spring and only until early-to-mid spring, when the deposits gradually sublimate back to the atmosphere, we can unambiguously distinct the shadows of the target ice blocks from the background. Continuing into the summer, the surface is entirely free of the seasonal deposits and the surrounding smaller ice blocks reappear.

At Ice Block 1, the images used, solar and slope conditions, along with the ice block heights and seasonal snow/ice depth are summarized in Table S1. The number of valid measurements during northern spring can vary from three in MY32 and MY36 and five in MY31 to six in MY30. All measurements except for one in MY31 fall within 35° and 70° in solar longitude. Some observations during the springtime have been excluded in the analysis due to bad image quality or no clear identification of the shadows. The curves generally feature decreasing trends, consistent with the phenomenon that during spring the sun rises above the horizon and the solar insolation increases with time. It is interesting to note that MY30/32 and MY31/36 share similar patterns, respectively. However, both patterns reach a thickness of ∼0.35 m at around Ls = 37.5°. The maximum difference between these two patterns is limited to be within ∼0.2 m. The uncertainty of the thickness inversion is about 0.11 m as illustrated in Section 5.1, these interannual differences could thus not be confirmed from a statistical point of view. For Ice Blocks 2 and 3, the images used, solar and slope conditions, along with the ice block heights and snow/ice depth are summarized in Tables S2 and S3, respectively. Their thickness evolution results are shown in Figure 7. They share similar trends with that of Ice Block 1, although the interannual dispersions are much more obvious than that of Ice Block 1 (but still limited to be less than ∼0.2 m). The depth inversion uncertainties at these two ice blocks are 0.10 m and 0.16 m, respectively (Section 5.1). Thus, these multiyear variations could not be confidently confirmed. For all of the three ice blocks, the earliest measurements fall within 20° and 25° in solar lon-

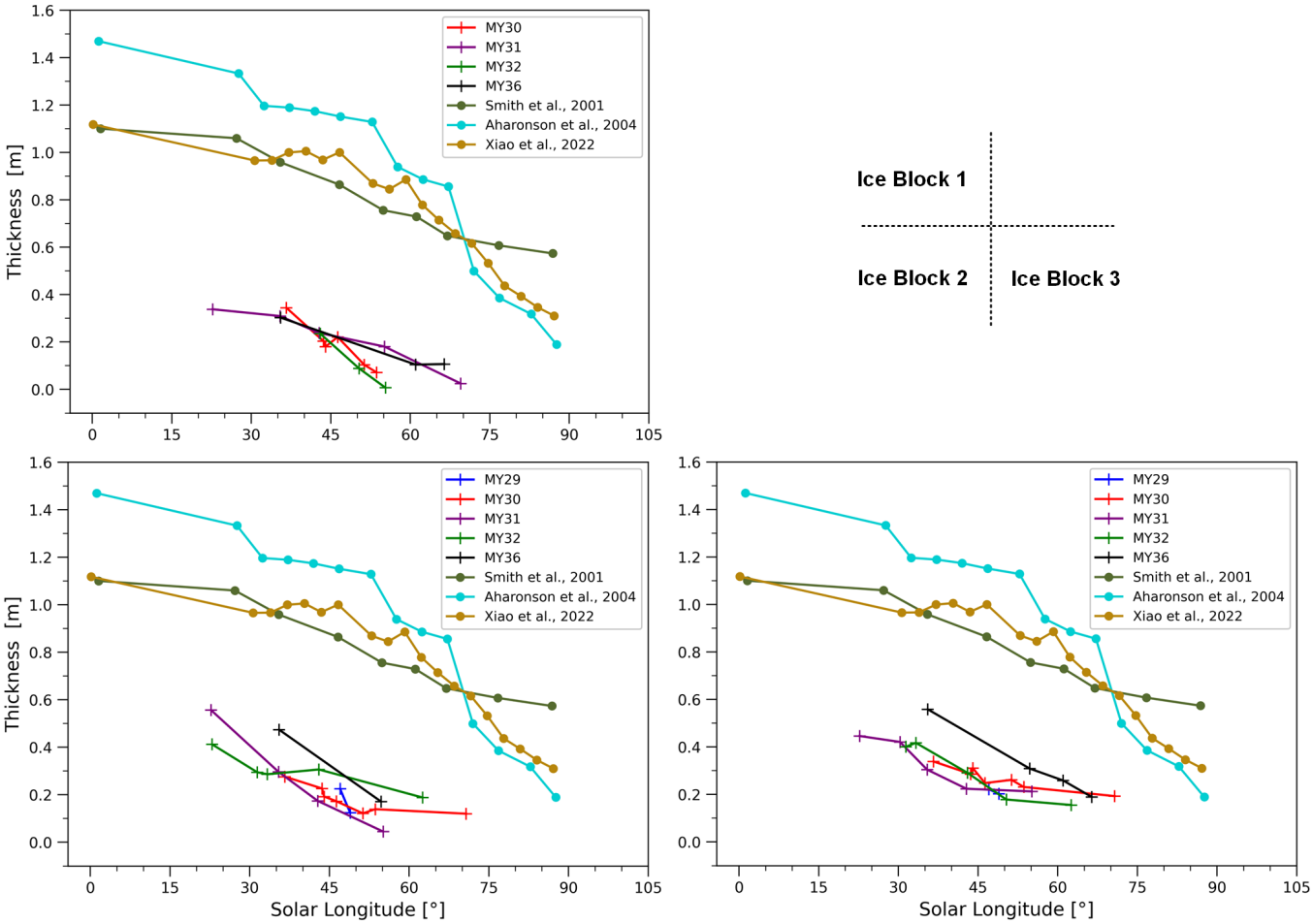

Figure 7: Upper left: Seasonal snow/ice thickness from MY30 to MY36 for Ice Block 1 at Scarp 1 (85.053°N, 151.833°E) during the northern spring. Bottom left: Seasonal snow/ice thickness evolution from MY29 to MY36 for Ice Block 2. Bottom right: Seasonal snow/ice thickness evolution from MY29 to MY36 for Ice Block 3. Measurements from this study are marked by crosses, and previous MOLA results are marked by dots. It should be noted that for D. E. Smith et al. (2001), the result shown is along the latitudinal annulus centered at 85.5°N. For Aharonson et al. (2004), it is the latitudinal annulus centered at 86°N.

gitude. There are images acquired in late winter and early spring, but as the elevation angle of the solar rays is less than 10°, the images are dimly-lit and attempts to measure the shadow length have failed. Furthermore, the bundle adjustment of these images can fail and no orthorectified versions are available for the measurements. These issues can be circumvented by the "BOUNDing" approach for which the thickness measurements are extended to cover late winter and early spring (Section 4.3).

Three previous MOLA results in the springtime of MY25, that is, D. E. Smith et al. (2001) at the latitudinal annulus 85.5°N, Aharonson et al. (2004) at the latitudinal annulus 86°N, and Xiao, Stark, Schmidt, Hao, Steinbrügge, et al. (2022) at the grid element centered at (85°N, 155°E) and of size 0.5° in latitude and 10° in longitude are shown for comparison (Figure 7). Before Ls = 70°, the results from D. E. Smith et al. (2001) and Xiao, Stark, Schmidt, Hao, Steinbrügge, et al. (2022) are generally consistent with each other, with a maximum thickness of ∼1.1 m at the beginning of spring and declining with time. Interestingly, all of the MOLA results consistently predicted a depth of ∼0.64 m at around Ls = 70°, before which the thickness measurements of Aharonson et al. (2004) are consistently the largest. When approaching summer solstice (Ls = 90°), all of the MOLA results feature non-zero thickness values, with that of D. E. Smith et al. (2001) being as high as ∼0.6 m. These deviations are considered outliers due to biases in the MOLA results as discussed in Section 5.5. Surprisingly, these MOLA results are consistently higher, by a magnitude of up to ∼1 m, than our measurements using shadows of the ice blocks. However, it should be noted that at this point the effects of direct condensation onto the tops of the ice blocks have not been considered, and the thickness measurements can be viewed as that contributed solely by snowfalls. These aspects are thoroughly discussed in Section 5.4. Possible explanations of the remaining offsets after the correction for these effects are examined in Section 5.5.

4.3 Snow/ice thickness in late winter and spring from "BOUNDing"

At Scarp 1, HiRISE images taken in late winter are available only in MY31. Thus, we apply the "BOUNDing" approach to all the images in MY31 with an attempt to place bounds on the snow/ice thickness all the way from late winter to spring, at solar longitudes of 7.0° , 17.3°, 22.7°, 30.3°, 35.4°, 42.8°, 55.1°, 69.5°, and 350.7°, respectively. The corresponding images are `ESP_024232_2650_RED`, `ESP_024509_2650_RED`, `ESP_024654_2650_RED`, `ESP_024865_2650_RED`, `ESP_025010_2650_RED`, `ESP_025221_2650_RED`, `ESP_025577_2650_RED`, `ESP_025999_2650_RED`, and `ESP_032632_2650_RED`, respectively. The solar elevation angles during acquisitions of these images are 7.9°, 12.2°, 14.3°, 17.3°, 19.2°, 21.7°, 25.3°, 28.3°, and 0.9° (late winter), respectively. The results obtained during late winter and early spring serve the purpose of filling the temporal gap of the "SUBTRACTing"-derived results. Meanwhile, the results obtained during mid-to-late spring can cross-validate the "SUBTRACTing"-derived results and check if the thickness measurements obtained at Scarp 1 are indeed much lower than the MOLA-derived values.

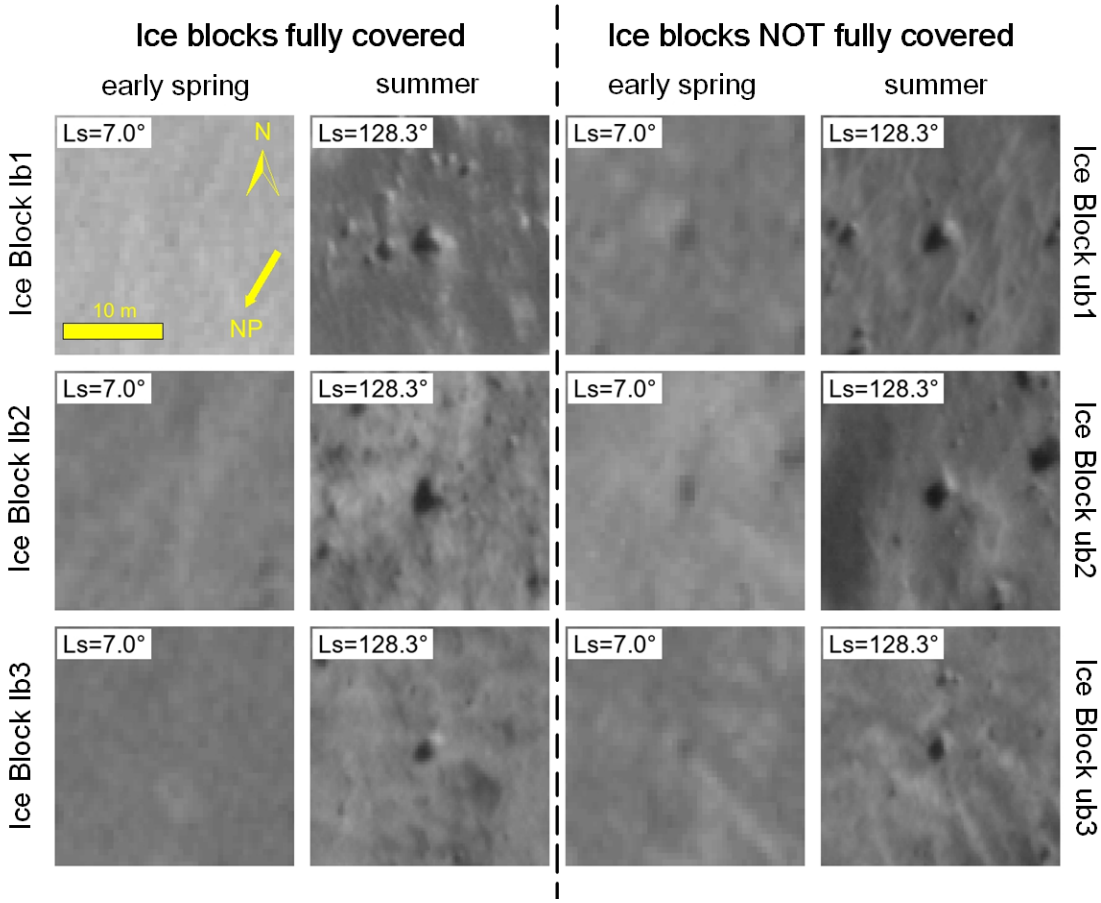

Figure 8: Images of example bounding ice blocks (centered at the sub-frames) at Ls = 7.0° in early spring and Ls = 128.3° in summer in MY31, respectively. The images used are `ESP_024232_2650_RED` and `ESP_027674_2650_RED`, respectively. These ice blocks are utilized to place bounds on the thickness of the seasonal snow/ice cover at Ls = 7.0°. The subscript "lb" means the ice block has been totally submerged and is capable of placing a lower bound on the thickness. Similarly, the subscript "ub" indicates the ice block in question has not been completely submerged and is capable of placing an upper bound on the thickness. Map projection and scale are as in Figure 6. Illumination is to the bottom-left corner.

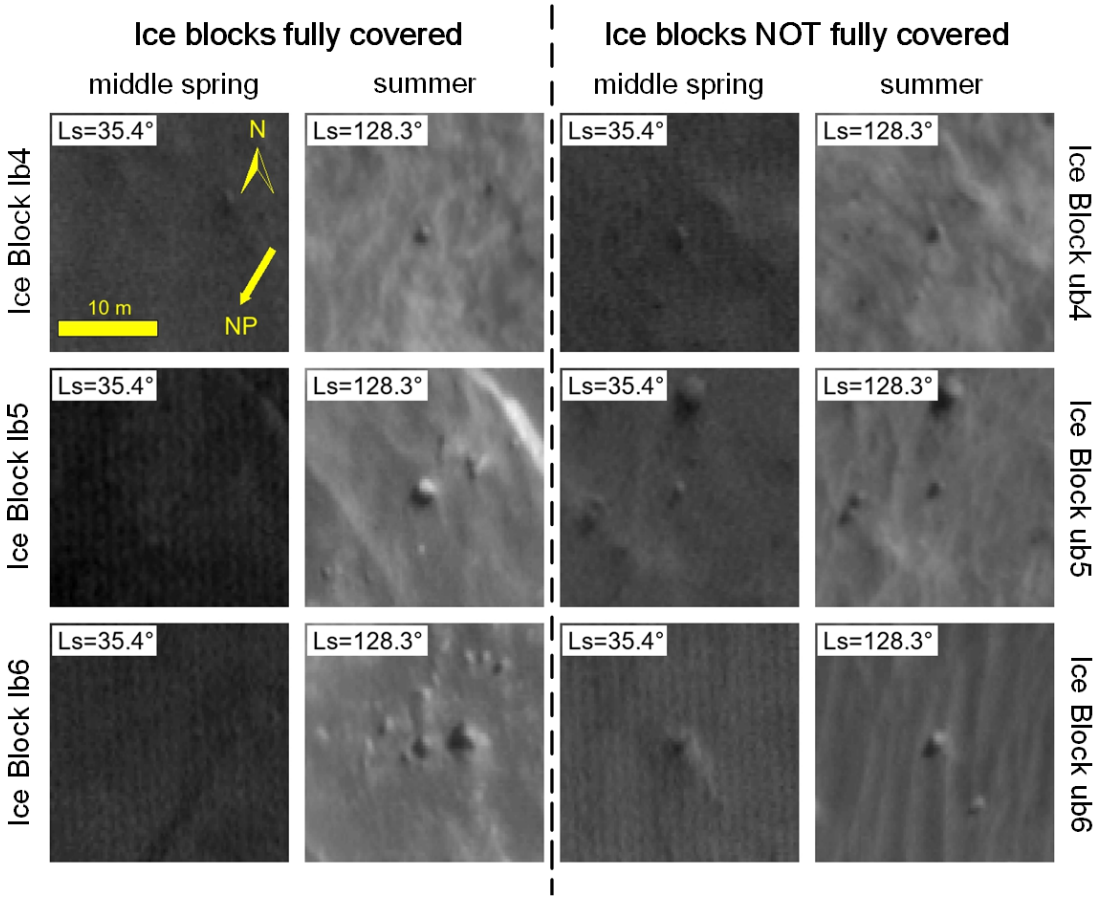

Figure 9: Images of three example bounding ice blocks (centered at the sub-frames) at Ls = 35.4° in middle spring and Ls = 128.3° in summer in MY31, respectively. The images used are `ESP_025010_2650_RED` and `ESP_027674_2650_RED`, respectively. These ice blocks are utilized to place bounds on the thickness of the seasonal snow/ice cover at Ls = 35.4°. Map properties and meaning of the subscripts in the ice block names are as in Figures 6 and 8. Illumination is to the bottom-left corner.

For late winter and early spring images acquired at Ls = 7.0°, Ls = 17.3°, and Ls = 350.7° that fail to be rectified during the bundle adjustment and subsequent orthorectification, we georeference them to the summer image taken at Ls = 128.3° in MY31 (`ESP_027674_2650_RED`). For this purpose, we select a total of around 10 control points that are homogeneously distributed over the image. These tie points are chosen to be stable ice blocks, corner points of protrusions from layers of the icy stratigraphy in the scarp, and large-scale topographic features over the Basal Unit outcrops. The affine transformation is then applied to tie these image to the summer one when is free of the seasonal layer. We proceed to select the locally tallest ice blocks, that is, with the longest shadows, and locally shortest ice blocks over Scarp 1. After that, the heights of these bounding ice blocks are measured in the summer image and serve as constraints on the seasonal snow/ice depth.

For demonstration purpose, we show example ice blocks used to bound the thickness of the seasonal cover at Ls = 7.0° in early spring and Ls = 35.4° in middle spring in MY31, respectively. At Ls = 7.0°, we display three example ice blocks that have been fully submerged, termed Ice Blocks lb1, lb2, and lb3, which can then indicate the minimum snow/ice depth in the Scarp 1 region (left panel in Figure 8). During the early spring, images reveal no texture related to the underlying ice blocks, demonstrating that the ice blocks have been completely buried underneath. Their heights measured in the subsequent summer when surface is free of seasonal deposits stand at 0.97 m, 1.02 m, and 0.93 m, respectively. After the correction of $-\xi_\Upsilon = -0.20$ m, these values become 0.77 m, 0.82 m, and 0.73 m, respectively. We proceed to showcase three other ice blocks that have not been fully submerged, named Ice Blocks ub1, ub2, and ub3, and hence can put upper limits on the snow/ice depth (right panel in Figure 8). Their heights measured at the coming summer stand at 1.20 m, 1.12 m, and 1.10 m, respectively. After the correction of $-\xi_\Upsilon = -0.20$ m, these values become 1.00 m, 0.92 m, and 0.90 m, respectively. These lower and upper bounds are extremely self-consistent with mean values of 0.77 m and 0.94 m, respectively. Thus, thickness of the seasonal layer at Ls = 7.0° is most likely to be within 0.77 m to 0.94 m. At Ls = 35.4° during middle spring in MY31, we show three example ice blocks that have been fully submerged, termed Ice Blocks lb4, lb5, and lb6, respectively. Their heights can place lower limits on the snow/ice depth in the Scarp 1 region (left panel in Figure 9). Their heights measured at the coming summer stand at 0.53 m, 0.61 m, and 0.56 m, respectively. After the correction of $-\xi_\Upsilon = -0.25$ m, these values become 0.28 m, 0.36 m, and 0.31 m, respectively. We then illustrate three other example ice blocks that have not been fully submerged, named Ice Blocks ub4, ub5, and ub6, and hence can render indication as to the maximum snow/ice depth (right panel in Figure 9). Their heights measured at the coming summer are 0.64 m, 0.64 m, and 0.70 m, respectively. After the correction of $-\xi_\Upsilon = -0.25$ m, these values become 0.39 m, 0.39 m, and 0.45 m, respectively. These bounding values are largely self-consistent with deviations of less than 0.1 m. Thickness of the seasonal layer at Ls = 35.4° is most likely to be within 0.32 m to 0.41 m.

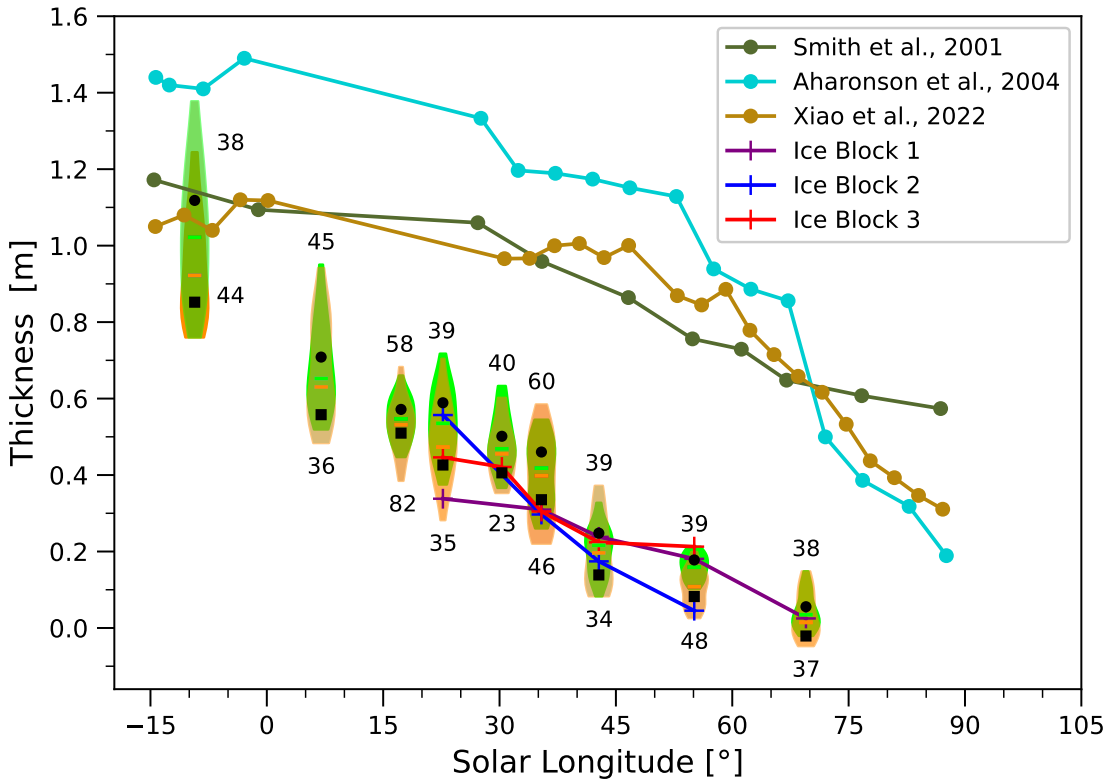

Figure 10: Results from both "SUBTRACTing" and "BOUNDing" in MY31, and their comparison to the existing MOLA results. The "SUBTRACTing" results for Ice Blocks 1, 2, and 3 are marked by crosses and connected by broken lines. The "BOUNDing" results have been corrected for the offset of $-\xi_\Upsilon$, and are represented by the violin plots with medians of the upper and lower limits shown as horizontal lines. Upper bounds shown in lime while lower bounds in orange, and the corresponding number of bounding ice blocks adopted are marked alongside the violin plots. Black squares and dots denote adjusted bounds in consideration of the standard errors of the median constraints. For simplicity and temporal continuity, the constraints obtained at Ls = 350.7° in late winter are plotted at Ls = −9.3°.

The bounding ice blocks used are quasi-uniformly distributed along Scarp 1 between 150.82°E and 151.95°E in longitude (Figure S2). Majority of them horizontally fall within 100 m to 600 m away from the foot of the scarp. The number of bounding ice blocks used at each solar longitude ranges from 23 at Ls = 30.3° to 82 at Ls = 17.3° (marked in Figure 10). The resulting correction of $-\xi_{\Upsilon}$ ranges from −0.02 m at Ls = 350.7° to −0.38 m at Ls = 69.5°. The corrected results from "BOUNDing" in MY31, in comparison to that from "SUBTRACTing" in MY31 and MOLA dataset in MY25, are shown in Figure 10. Note that the "SUBTRACTing" yield results for Ice Blocks 1, 2, and 3 (Section 4.2), while the "BOUNDing" results represent large-scale average constrains measured at tens of bounding ice blocks distributed over Scarp 1 (Figure S2). Ice Blocks 1, 2, and 3, at more than 1.2 m, are much higher than that of the bounding ice blocks, which are at a similar level with depth of the seasonal deposits to be constrained. The "BOUNDing" approach can yield estimates in late winter and early spring while "SUBTRACTing" are temporally limited to mid-to-late spring. Thickness bounded by median limits are highest during late winter with values most likely falling between 0.92 m and 1.02 m at Ls = 350.7°, then that decrease to be between 0.63 m and 0.65 m at Ls = 7.0° in early spring, between 0.20 m and 0.22 m at Ls = 42.8° in middle spring, and gradually decrease to be within 0.01 m and 0.03 m at Ls = 69.5° in late spring. The thin layer at Ls = 69.5° is not in conflict with the statement of Piqueux et al. (2015) that the area of the SNPC shrunk to zero at around Ls = 80° in MY31. Differences between upper and lower limits are smaller than 0.1 m at all examined solar longitudes, demonstrating the high precision of the average thickness estimates from "BOUNDing" approach. Apart from shadow length measurement errors and the inclusion of overly tall (in the uncovered case) or short (in the completely covered case) bounding ice blocks, dispersion of the thickness constraints at each examined solar longitude can to some extent reflect regional variability of the snow/ice depth. The bulk upper and lower constraints overlap well at all examined solar longitudes. This can be partially attributed to, other than the aforementioned factors, the tendency that ice blocks used to derive lower bounds are more likely to be located where feature thicker snow/ice cover, while that for generating the upper bounds more frequently fall within regions with shallower snow/ice deposits. The adjusted bounds taking into consideration of the standard errors of the medians from Equation 13 are represented by black squares and dots in Figure 10, respectively. The updated bounding intervals feature half ranges from 0.03 m at Ls = 17.3° to 0.13 m at Ls = 350.7°, and with typical values of ∼0.05 m (Table S4). The measurements from "BOUNDing" are largely consistent with that from "SUBTRACTing", especially when considering the uncertainty of the latter which ranges from 0.10 m to 0.16 m (Section 5.1). This demonstrates the feasibility and correct implementation of the proposed approaches. Interestingly, both of these results offset the MOLA ones by up to 1 m. However, it should be noted the overlying layers over the ice blocks due to direct condensation have not been considered in the "SUBTRACTing" and "BOUNDing" models. These thickness measurements thus represent the sole contribution by the snowfalls. Estimation of

these effects and the correspondent correction of the "BOUNDing" thickness constraints in MY31 are discussed and described in Section 5.4.

5 Discussion

5.1 Long-term stability of the ice block heights and precision of the "SUBTRACTing" thickness measurements

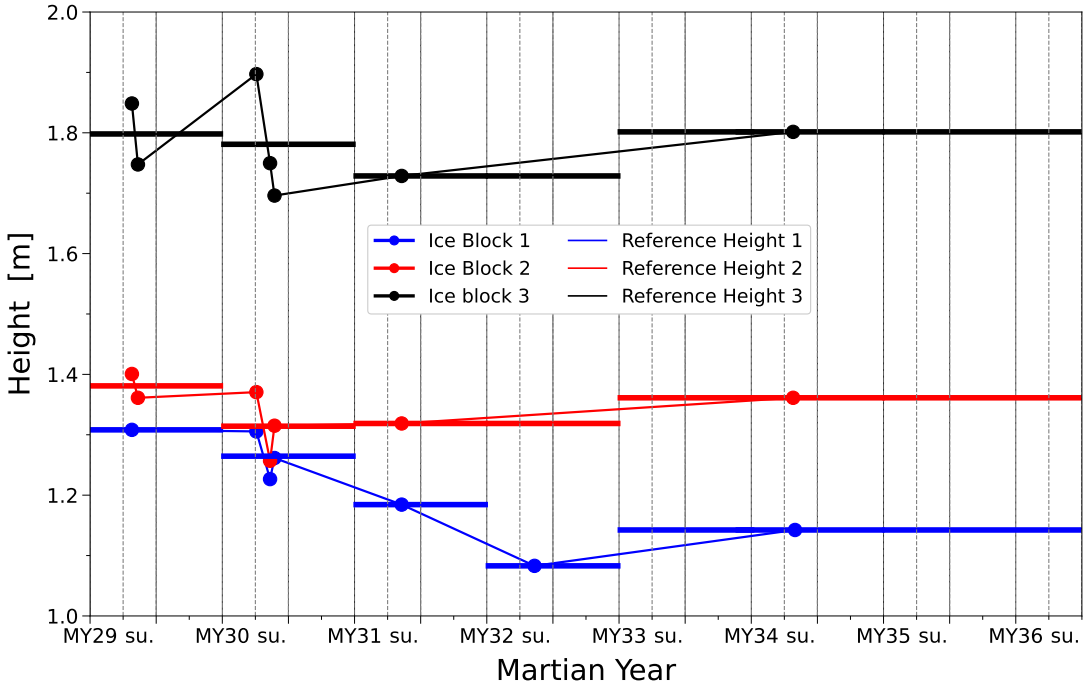

Figure 11: Ice block heights (dots) measured at summertime when free of snow/ice cover and the resultant reference heights (horizontal lines), the latter of which are used for the calculation of the CO_2 snow/ice thickness in the springtime. Note that there exists no height measurements in MY33, MY35, and MY36 due to the lack of image coverage, and the measurement at the adjacent MY34 is used instead as the reference height. Temporal separation between contiguous ticks in the horizontal axis is 90° in solar longitude, that is, a Martian season. su. is the abbreviation for summer.

Here, we discuss the stability of the heights of Ice Blocks 1, 2, and 3 which are used as reference when computing the snow/ice thickness during the springtime. We also discuss the precision of the resultant thickness measurements from the "SUBTRACTing" method.

Ice block heights measured when the CO_2 snow/ice cover completely sublimated in various summers are shown as dots in Figure 11. Summer images used are marked in bold in Tables S1, S2, and S3 for Ice Blocks 1, 2, and 3, respectively. When multiple ice block height measurements exist within the same summer, their average is taken as the reference value (hori-

zontal lines in Figure 11). The bare heights of Ice Blocks 1, 2, and 3 are generally stable with variations within ∼0.1 m for Ice Blocks 2 and 3 but can be up to 0.2 m for Ice Block 1. It is worthy to note that these heights generally exhibit a gentle decline from MY29 to MY33, after which an increase in MY34 can be spotted. These long-term decreases in ice blocks heights could be due to tumbling under its own gravity or that triggered by external forces. Meanwhile, aeolian erosion may also be responsible. To mitigate the effects of quasi-stability, we assign the heights measured at temporally adjacent summers as the baseline for inverting for thickness of the seasonal deposits during the spring (Figure 11). While it is reasonably to speculate their decreases in heights due to wind erosion and disintegration of the upper parts due to condensation/sublimation of the seasonal ice cover, we hardly find any physical explanations for their growth. Thus, we attribute these abnormal height increases to potential errors in the reference measurements. The induced systematic biases in the thickness values obtained in the springtime for Ice Blocks 1, 2, and 3 are then 0.06 m, 0.05 m, and 0.07 m, respectively.

To look into the random errors that can also deteriorate the precision of our thickness measurements, we combine two types of observables. If there are two or more height measurements during each Martian summer, the inconsistencies between measurement pairs are used as a reasonable gauge of the random errors. Additionally, we examine the repeatability between thickness measurement pairs in the springtime if their temporal separations are within an empirical threshold of 5° in solar longitude. In this case, seasonal snow/ice sublimation within these relatively short timespans can be neglected and the aforementioned deviations from zero can gain us insights into the precision of our measurements. The standard deviation is calculated as follows:

$$\sigma_H = \sqrt{\frac{1}{n-1}\sum_{i=1}^{n}\left(\frac{\Delta H_i}{2}\right)^2}\,, \tag{14}$$

where ΔH_i represents the i^{th} qualified height discrepancy, out of a total of n, to be evaluated. We scale the random error σ_H by a factor of three for the metric to be robust. For Ice Block 1, there are three qualified values during the summers and seven values during the springs. The random error of Ice Block 1 is 0.09 m. For Ice Block 2, there are five qualified height discrepancies during the summers and nine values during the springs, respectively. And, the random error of Ice Block 2 is calculated at 0.09 m, which is the same as that of Ice Block 1. Meanwhile, for Ice Block 3, five qualified values are available during the summertime and nine during the springtime. The random error of Ice Block 3 stands at 0.15 m.

We proceed to calculate the Mean Square Error (MSE) that takes into consideration of both the systematic bias expressed as ε_H and random error, expressed as $3\sigma_H$, at each of the three locations. These quantities are related as

$$\mathrm{MSE}(\hat{T}) = \mathbb{E}\left[(\hat{T}-T)^2\right] = \mathrm{Var}(\hat{T}) + \mathrm{Bias}^2(\hat{T}) = 9\sigma_H^2 + \varepsilon_H^2\,, \tag{15}$$

where T denotes the thickness measurement during springtime. The square roots of the MSE errors for thickness measurements for Ice Blocks 1, 2, and 3 are 0.11 m, 0.10 m, and 0.16 m,

respectively. The uncertainty of our thickness measurements from ice blocks can thus be ∼0.1 m at the best scenarios, which is on similar level with the statement from Mount & Titus (2015). These empirical uncertainties represent the cumulative impacts of a combination of factors such as variations in image quality and solar condition, uncertainties in HiRISE DEMs, image orthorectification errors, and shadow length measurement errors.

Although these precision statistics do not allow unambiguous confirmation of possible seasonal thickness variations over multiple years (up to ∼0.2 m), they do validate the notion that no significant thickness variations exist in middle-to-late springs from MY29 to MY36. In addition, it strengthens the statement that our thickness measurements are much lower than previous MOLA results. This statement is independently verified using the "BOUNDing" approach as shown in Section 4.3.

5.2 Characteristics of the "BOUNDing" approach and its automation

Compared to "SUBTRACTing", the "BOUNDing" approach avoids the need to clearly identify and accurately measure the shadow length of the ice blocks during late winter and spring. Instead, one only needs to check if there exist cast shadows around the ice blocks to decide whether they have been completely covered or not. That is a delightful advantage over the "SUBTRACTing" approach, especially during late winter or early spring when the shadow boundaries of the ice blocks can be unidentifiable due to low solar elevation and thick seasonal layer. This advantage means that images obtained during wintertime and springtime are not necessarily required to be bundled adjusted and orthorectified, which can greatly boost computation efficiency. In fact, bundle adjustment can fail with images acquired in late winter or early spring which cannot be utilized in the "SUBTRACTing" approach. For these aforementioned reasons, the "BOUNDing" approach can temporally extend to cover late winter and early spring. Unfortunately, "BOUNDing" can be difficult to implement during late spring as the snow/ice depth shrinks to a low level. In such case, the bounding ice blocks along with their shadows required to place the lower and upper limits become too small to be resolved in the HiRISE images. In addition, the strength of the constraints that can be placed by the "BOUNDing" approach depends on the height gap between the bounding ice blocks. For scarps with good concentration of ice blocks, the precision of the obtained thickness constraints would be satisfying. Further improvement can be expected by spatial averaging of the thickness bounds over a large area. However, "BOUNDing" can fail in regions where number of ice blocks are limited or the distribution of the ice block heights does not overlap with the seasonal snow/ice thickness to be constrained, for example, in fields where only debris and extremely small ice blocks remain. Despite various merits of "BOUNDing" over "SUBTRACTing", these two approaches can be complementary to each other. For temporal extension to late winter and early spring, and spatial extension to a large set of ice block clusterings at individual scarps, automatic version of "BOUNDing" would be the choice. However, in case high spatial resolution is required within regions of interest, for example, over spe-

cific surface features, or when available ice blocks are scarce, "SUBTRACTing" should be applied instead. Meanwhile, in a situation when both approaches can work, their results at mid-to-late springtime can be used for cross-validation purposes.

We would like to stress that "BOUNDing" can actually be applied to all good-quality images acquired from MY29 on and form thickness evolution time series in multiple years (Section 4.3). Unfortunately, that would require a tremendous amount of efforts to manually identify the proper bounding ice blocks and measure their shadows in the summer images. As such, we plan to build on previously-developed automatic software for this purpose, by combining computer vision for delineating the shape of the ice blocks (Fanara et al., 2020a,b) with Convolutional Neural Networks for identifying newly-placed ice blocks (Su, Fanara, Xiao, et al., 2023). In order to infer their corresponding heights, extracted horizontal boundary of the ice blocks can be fitted using ellipsoids, triangular prisms, circular cones, or pyramids according to the delineated shape of the shadows. These software programs are established and well maintained in Institute of Geodesy and Geoinformation Science, Technische Universität Berlin. Existing tools that automatically locate and measure boulders on Mars (for example, Golombek et al., 2008; Nagle-McNaughton et al., 2020; Hood et al., 2022), will be adapted for detecting ice blocks and used for cross-validation purposes. The main idea is to automatically identify the ice blocks, exclude newly-formed ice blocks, and determine the corrected ratio of the ice blocks that have not been completely submerged during late winter and spring as compared to that in the summer. Meanwhile, the approximated sizes of the ice blocks, including approximated vertical dimension, during the summertime should be automatically determined. Then, we can statistically relate the detected ratio to the thickness of the seasonal ice layer according to probability distribution of the ice block heights:

$$\int_{T_\Upsilon}^{H_{\max}} p(H)\, dH = \Delta\,, \quad s.t. \quad \int_{0}^{H_{\max}} p(H)\, dH = 1\,, \tag{16}$$

where T_Υ is the thickness of the seasonal layer at Ls $= \Upsilon^\circ$ corresponding to the acquisition time of a specific HiRISE image, $H_{\max}$ is the maximum height of the ice blocks within an examined region, and $p(H)$ is the normalized probability density of the ice block heights. Meanwhile, Δ is the software-determined quantity ratio of ice blocks that have not been fully submerged at Ls $= \Upsilon^\circ$. It should be noted that Equation 16 should be in its discretized form as the number of ice blocks within an interest region does not reach infinity. The expected advantage of this automatic approach, tentatively termed automatic "BOUNDing", is the capability to be efficiently applied to entire set of active scarps across the North Pole (refer to Section 5.7 for locations) and to monitor the depth evolution in real time once a HiRISE image beams back to Earth. An additional merit would be that it can completely avoid the cumbersome procedure of measuring dimensions of the shadows, as required in "SUBTRACTing" and "BOUNDing".

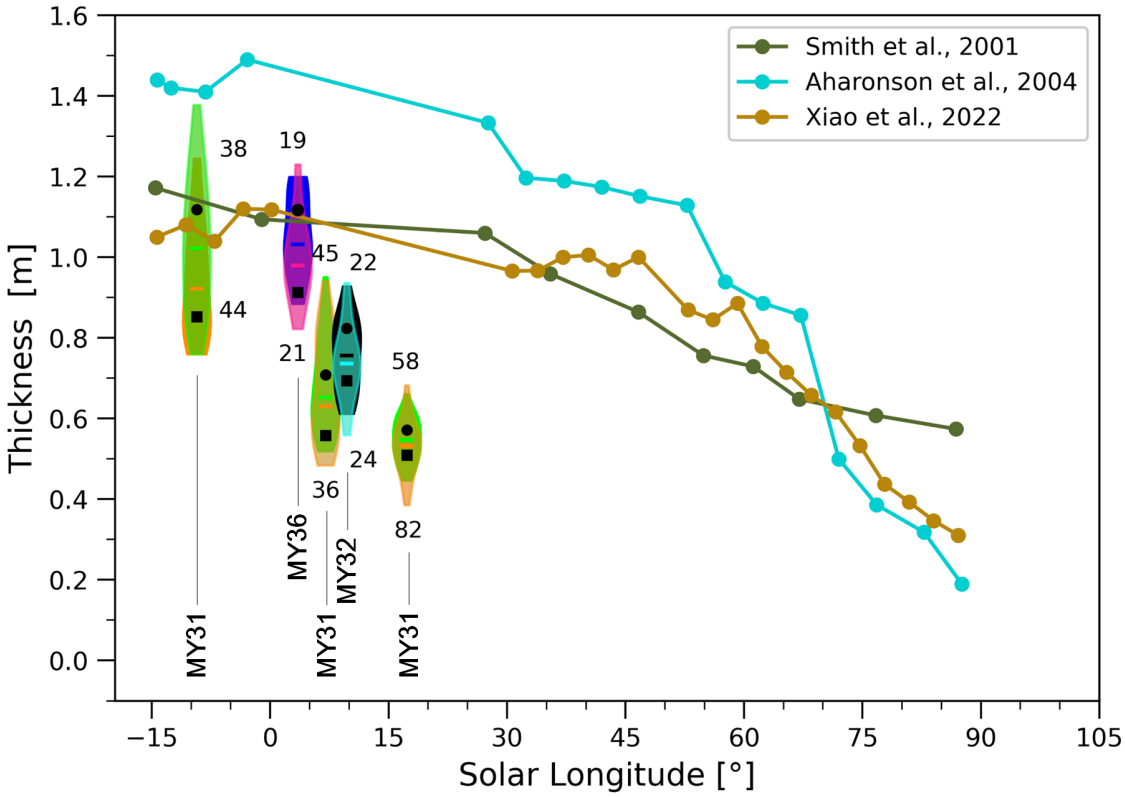

Figure 12: Comparison of thickness results in early springs of MY31 (same as in Figure 10), MY32, and MY36 from the "BOUNDing" approach. The bounding limits have been corrected for the offset of $-\xi_\Upsilon$. The results are represented by the violin plots with medians of the upper and lower limits shown as horizontal lines. The corresponding number of bounding ice blocks adopted are marked alongside the violin plots. Black squares and dots denote adjusted bounds in consideration of the standard errors of the median constraints (Equation 13). For simplicity and temporal continuity, the constraints obtained at Ls = 350.7° in late winter of MY31 are plotted at Ls = −9.3°. Existing MOLA results are shown for reference.

5.3 Interannual snowfall variations from "BOUNDing"

Due to high precision of the "BOUNDing" method over scarp-scale area, we proceed to apply it to examine possible interannual thickness variations in the very early spring (before Ls = 10°) when the seasonal layer is among the thickest. After excluding images with bad quality, only `ESP_024232_2650_RED` acquired at Ls = 7.0° in MY31, `ESP_033120_2650_RED` at Ls = 9.7° in MY32, and `ESP_068224_2650_RED` at Ls = 3.5° in MY36 are available. For MY31 and MY32, the same summer reference image is used (`ESP_027674_2650_RED`) and the corrections of $-\xi_\Upsilon = -0.20$ m and $-\xi_\Upsilon = -0.22$ m are respectively applied to the overestimated thickness values. For MY36, the summer image acquired in MY34 is used (`ESP_053730_2650_RED`) and a correction of $-\xi_\Upsilon = -0.08$ m is adopted. Bounding ice blocks are selected over the entire Scarp 1. The corrected results and their comparison are shown in Figure 12. The results at Ls = 350.7° and Ls = 17.3° in MY31 are also shown alongside that at Ls = 7.0° in MY31 to illustrate the general depth evolution trend during the beginning of spring (same as in Figure 10). The median depth bound at Ls = 9.7° in MY32 is from 0.74 m to 0.76 m. Meanwhile, the median depth bound at Ls = 3.5° in MY36 ranges from 0.98 m to 1.03 m, which is ∼0.36 m larger than between 0.63 m and 0.65 m at Ls = 7.0° in MY31. Considering the adjusted bounds at the examined solar longitudes in MY31 and MY36 (black squares and dots in Figure 12), the interannual variation of ∼0.36 m can be deemed credible. Indeed, treating the thickness bounds at MY31 and MY36 as being independent, the propagated uncertainty associated with the MY31 to MY36 thickness variation is 0.13 m. A supporting evidence is that there exist plenty of ice blocks that are visually detectable at Ls = 7.0° in MY31 can stay completely covered at Ls = 3.5° in MY36. We can also see in the plot that all of the examined thickness values are lower than the existing MOLA results, by a magnitude of 0.1 m to 1 m. However, we note again that the effects of crowning layers on top of the ice blocks due to direct condensation have not been considered in the applied "BOUNDing" model. As such, the detected multiyear thickness variation refers to that solely induced by the snowfalls (Section 5.4). This is the first time that an interannaul variation in the amount of Martian snowfalls is detected, stressing the importance of carrying out long-term monitoring of the Martian volatile and dust cycles.

5.4 Crown depth estimation and correction in MY31

In the presented geometric models (Figures 1, 2 and 3), we have not attempted to correct for the effects of moating and crowning. For rocks, moats form in the fall while they are still warm with stored heat energy from summertime solar insolation (Mount & Titus, 2015). Snow/ice falling around the warm rocks will sublime, leaving a void. Moating has been extensively observed around the rocks in the dune fields (Mount & Titus, 2015), which can be attributed to the large contrast in thermal inertia of rocks (relatively high) and sands (relatively low). The ice blocks fallen from the NPLDs, as investigated in our case, are made mainly of water ice, which feature very high thermal inertia. However, the upper layer of the Basal Unit

771 deposits where the ice blocks reside is presumably composed of previously fallen ice blocks, lead-
772 ing to its sloped surface at the foot of the NPLDs. Evidence has it that the potentially active
773 scarps generally feature a higher overall slope from Basal Unit outcrop top to bottom than the
774 potentially quiescent ones (Russell et al., 2010). As a result, the contrast in thermal inertia be-
775 tween the ice blocks and the underlying Basal Unit top layer should be limited. Thus, exten-
776 sive moating well into the springtime should be unlikely. Indeed, we have not observed any in-
777 stance of moating around the ice blocks during springtime with typical examples shown in Fig-
778 ures 6, 8, and 9. The formation of a topping ice layer, that is, crowning, has been properly ac-
779 counted for when using shadowing of the rocks to invert for thickness evolution of the seasonal
780 snow/ice deposits (Mount & Titus, 2015). For rocks, crowns form in the winter, after they have
781 lost sufficient heat and are expected to be most prevalent in early to mid-spring. If crowns form
782 then the measured shadow length will be longer than in the case without, making the uncor-
783 rected rock height larger and thus reducing the calculated snow/ice thickness. For ice blocks,
784 the crowning can also happen and should be properly accounted for. Indeed, we have observed
785 systematic widening of the ice block walls in the HiRISE images which is due to direct conden-
786 sation of CO_2 as frosts (Figure 13).

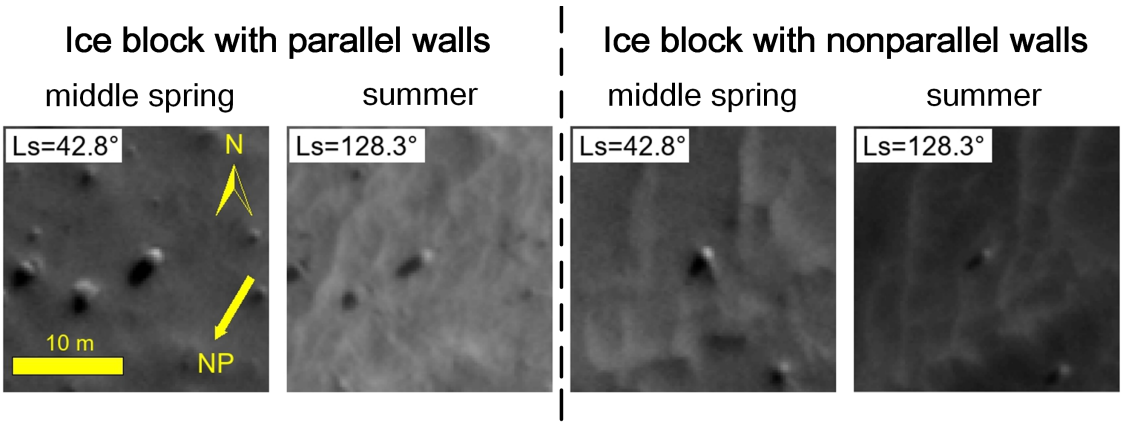

Figure 13: Images of example ice blocks (centered at the sub-frames) used to deduce depth of topping crowns. Acquisition time stamps of the images are Ls = 42.8° in middle spring and Ls = 128.3° in summer in MY31, respectively. The images used are `ESP_025221_2650_RED` and `ESP_027674_2650_RED`, respectively. Left panel shows an ice block with parallel walls and its shadow, the thinning of which from middle spring to summer is obvious. Right panel refers to the change of a cone-shaped ice block. Map projection and scale are as in Figures 6, 8, and 9. Illumination is to the bottom-left corner.

787 Mount & Titus (2015) corrected for the crowning and moating by adding the increases
788 in snow/ice depths between consecutive solar longitudes to all prior depths. This forces the ice
789 depth to either decrease or remain the same between different solar longitudes, and the corrected
790 values serve as minimum bounds to the seasonal snow/ice depth. The representative ice depth

curve before correction in their study features significant increases during middle-to-late spring (Figure S3 in Mount & Titus (2015)). However, in our case we have not seen significant off-season increases (Figures 7, 10, and 12), so the results should not change much after incorporating their correction scheme. This indicates that the depths of the crowns over the ice blocks in this study likely quasi-linearly decrease to zero right at when the seasonal deposits completely sublimate back into the atmosphere. To conclude, the correction scheme described in Mount & Titus (2015) can be inapplicable in our case. We thus propose an original way to estimate and correct for the effects of the crowning on top of the ice blocks. The proposed correction scheme relies on three reasonable assumptions: (1) Atmospheric deposition as snowfalls do not accumulate over the top of the selected spiky ice blocks and over steep ice block walls. In fact, it is known that aeolian processes can redistribute the carbon dioxide snow crystals into topographic lows, damping the topography (Mount & Titus, 2015). Ice blocks shaped like triangular prisms or feature lone peaks are used in the demonstration of the "SUBTRACTing" and "BOUNDing" approaches (Figures 6, 8, and 9), which makes significant accumulation of snow particles over the ice blocks unlikely. Thus, the crowns in our case can be solely composed of directly condensed frosts; (2) Frosts through direct condensation are homogeneously distributed around the ice blocks and their adjacent surroundings. This hypothesis can be corroborated by the fact that there exist limited thermal contrast between the ice blocks and the Basal Unit outcrops where they reside on. It is further justified by similar depths of ice block crowns at a specific solar longitude over the entire scarp, as illustrated in Figure 14; (3) Negligible moating around the ice blocks, as previously demonstrated in this section. These assumptions mean that the contributions of the snowfalls and frosts to the thickness of the seasonal ice deposits can be decomposed and estimated separately. The thickness measurements from "SUBTRACTing" and "BOUNDing" (T_Υ at Ls $= \Upsilon^\circ$) can be considered as merely contributed by snowfalls (Figures 7, 10, and 12). Indeed, if there exists no snowfall, then the shadow length of the ice blocks would remain unchanged and thickness measurements from "SUBTRACTing" and "BOUNDing" should all equal zero. These assumptions also enable us to use the widening of the ice blocks as a proxy to approximate the depths of the crowning frost layers over the ice blocks (T^{c}_Υ at Ls $= \Upsilon^\circ$). The total thickness of the seasonal layer then can be calculated as the sum of T_Υ and T^{c}_Υ.

To approximate the depths of the crowns, we first examine the widening of cylinder-shaped ice blocks with parallel walls, mostly vertical walls, during late winter and spring as compared to their dimensions during the summertime when the enveloping seasonal CO_2 frost layer completely sublimates away. A typical example of these particular ice blocks is shown in Figure 13. Within the portion of the shadow with parallel bounding lines, the width of the shadow, and hence that of the ice block itself, can be directly measured along any transverse line running perpendicular to the solar illumination. Then, the crown depth at Ls $= \Upsilon^\circ$ can be approximated by

$$\hat{T}^{\mathrm{c}}_\Upsilon = \frac{W^1_\Upsilon - W^2}{2}\,, \tag{17}$$

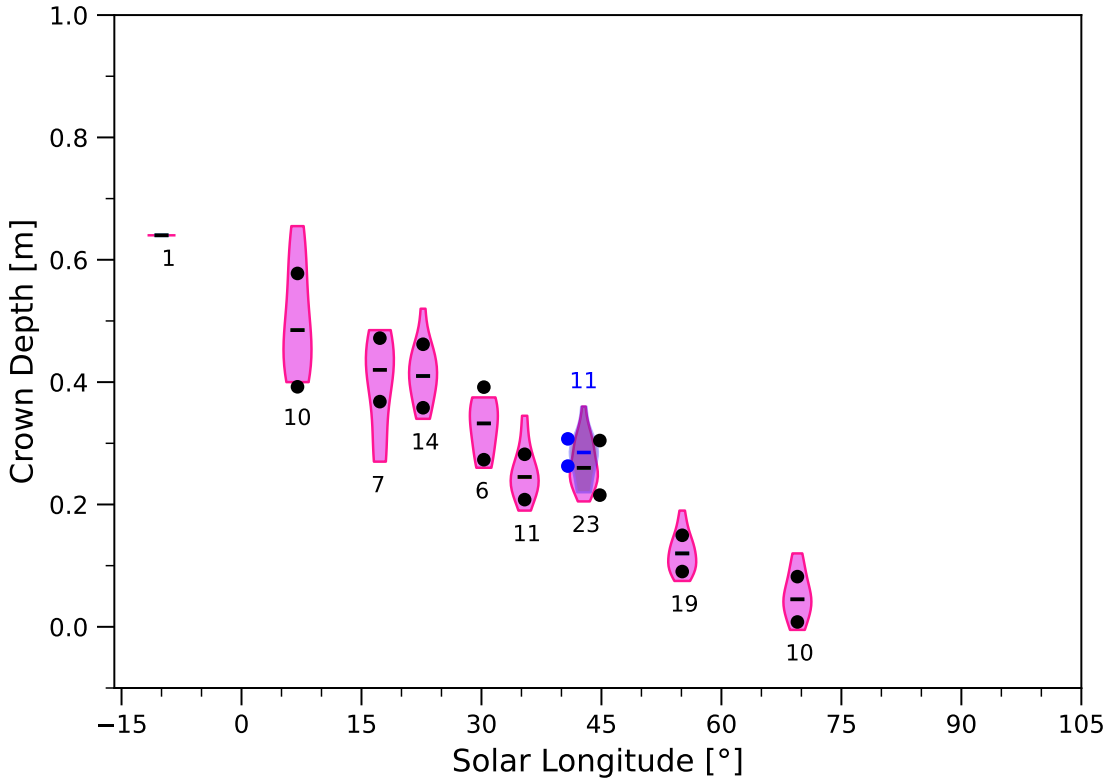

Figure 14: Depth estimates of the crowns from direct condensation over Scarp 1 in MY31, as represented by the violin plots with medians shown as horizontal lines. The corresponding number of independent measurements are marked alongside the violin plots. Pink violins represent measurements using ice blocks with parallel walls and the blue one at Ls = 42.8° refers to that from ice blocks with nonparallel walls. Black and blue dots denote derived bounding intervals by taking into account of the standard errors of the medians. For simplicity and temporal continuity, the single constraint obtained at Ls = 350.7° in late winter is plotted at Ls = −9.3°.

where W^1_Υ is the width of the shadow of the ice block during late winter or spring, and W^2 denotes that of the same ice block during summertime. Temporal evolution of the crown depth over the late winter and spring in MY31 is illustrated in Figure 14. The abstract probability distribution of crown depth measurements at a specific solar longitude is approximated using Equation 11 and represented using a pink violin. At Ls = 42.8°, the image features the best sharpness and the most measurements are made (a total of 23), with a median value of 0.26 m. In contrast, at Ls = 350.7° in late winter the image is the most severely blurred and only one valid measurement is obtained with a value of 0.64 m. For early spring images acquired at Ls = 7.0° and Ls = 17.3°, the dispersions of the measurements are relatively large due to degraded quality associated with still low solar elevation angles. As can be seen in the plot, the crown depth quasi-linearly decreases from 0.64 m at Ls = 350.7° in late winter, 0.26 m at Ls = 42.8° in middle spring, to 0.045 m at Ls = 69.5° in late spring. The approximately quasi-linearly declining trend corroborates our previous conjecture in the light of limited middle-to-late spring thickness increases present in our uncorrected results. Like it has been done in Equation 13, we derive adjusted bounding intervals for the most likely crown depths at Ls = Υ° by taking the standard errors of the medians into account:

$$\Theta^c_\Upsilon = \left[\mathrm{Md}^c_\Upsilon - \frac{3 \times \mathrm{SMAD}^c_\Upsilon}{\sqrt{N^c_\Upsilon}},\ \mathrm{Md}^c_\Upsilon + \frac{3 \times \mathrm{SMAD}^c_\Upsilon}{\sqrt{N^c_\Upsilon}} \right], \tag{18}$$

which are marked as black dots in Figure 14. The half ranges of these bounding intervals are from 0.02 m at Ls = 55.1° to 0.09 m at Ls = 7.0°, with typical values on the order of 0.05 m (Table S4). The limited dispersions in crown depths, or ice block widening, over the entire scarp at individual solar longitudes can to some extent reflect the spatial uniformity of the directly condensed layer in the vertical dimension. This serves as an additional line of evidence to justify our second assumption that the directly condensed frost layer is of the same thickness over the ice blocks and their adjacent surroundings. The estimated 0.64 m deep frost layer due to direct condensation in late winter is significantly shallower than the snow layer with a thickness of 0.97±0.13 m (Section 4.3). In terms of thickness and volume, the snowfalls can make up 60.2% of the seasonal deposits in late winter. However, assuming the crowns to be slab ice that features a density greater than or equal to 1,190 kg/m^3 (≤26% porosity, ≥8,000 μm grains) and the snow to feature a density of less than or equal to 420 kg/m^3 (≥74% porosity, ≤1,000 μm grains) (Mount & Titus, 2015), then snowfalls should account for less than 34.9% of the seasonal deposits in terms of mass during late winter.

As majority of the ice blocks used in the demonstration of the "SUBTRACTing" and "BOUNDing" methods are peaked or triangular-prism-shaped, we wonder if similar amount of frosts is directly condensed onto these nonparallel walls. Thus, we also look into the widening of the cone-shaped ice blocks. The schematic of the geometry with shadow width measuring points marked is illustrated in Figure 15. As the boundaries of the shadows of these peaked ice blocks are triangular-shaped, shadow width measurements have to be made at properly adjusted positions so that they can be directly compared to reveal the widening. From Equation 6, the relation between

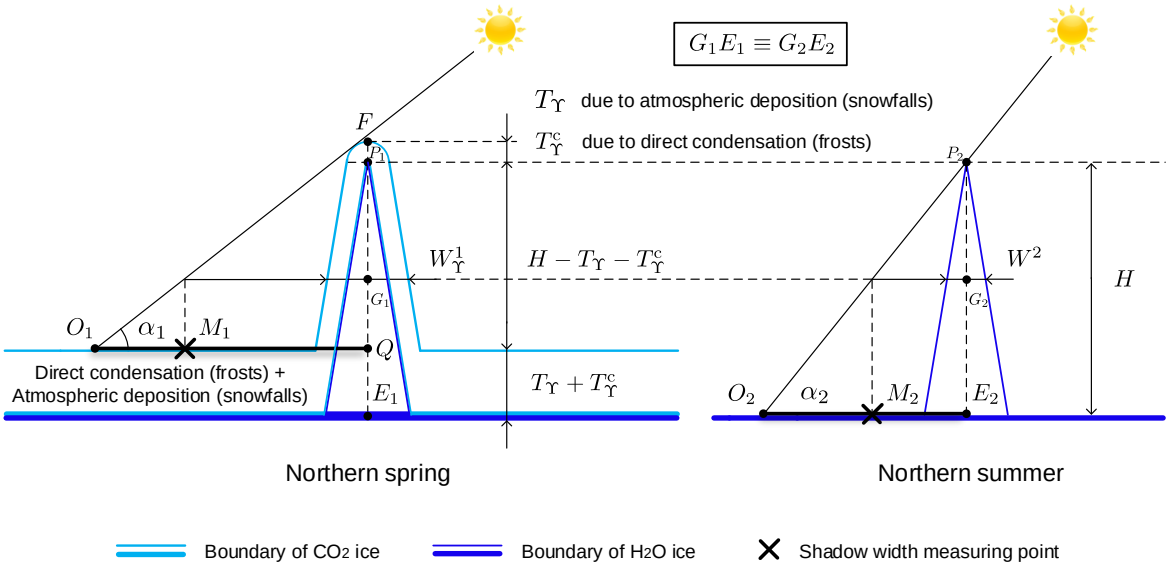

Figure 15: Schematic showing how to measure the width widening of a cone-shaped ice block at Ls = $\Upsilon°$. In spring, the ice block and its surrounding surface are covered with a layer of CO_2 deposits, with a thickness of T^c_Υ over the former and $T_\Upsilon + T^c_\Upsilon$ over the latter. The variable T_Υ denotes the thickness of the seasonal deposits accumulated by snowfalls, and T^c_Υ the contribution from direct condensation as frosts. During summertime, the seasonal deposits have completely sublimated back into the atmosphere and allows the bare height of the ice block (H) to be estimated. Slope and aspect of the local terrain are neglected. Locations of the shadow width measurements to be compared are marked by black crosses which ensure $G_1E_1 \equiv G_2E_2$. Note that directly condensed and CO_2-snowfall-scavenged water ice particles within the seasonal deposits are not marked.

867 the height of the ice block (H) and the measured shadow length (L_S) in the summer image can
868 be written as follows:

869 $$H = L_S \times (\cos\omega \sin\beta + \tan\alpha \cos\beta)\,. \tag{19}$$

870 To simplify the model, we only use ice blocks situated over gentle slopes of less than 5°. Ne-
871 glecting the slope in Equation 19, that is $\beta = 0$, then it reduces to be

872 $$H = O_2E_2 \times \tan\alpha_2\,, \tag{20}$$

873 where O_2E_2 is the shadow length of the ice block when it is free of seasonal CO_2 snow/ice in
874 the summertime (Figure 15). We now define δ_1 and δ_2 as the ratios of the distances from the
875 shadow top to the width measuring point along the solar illumination to the full shadow length
876 at spring and summer images, respectively. From the geometry of the ice block and the over-
877 lying seasonal layer, these two ratios can be defined as follows:

878 $$\begin{cases} \delta_1 = \dfrac{O_1M_1}{O_1Q} = \dfrac{G_1Q}{FQ} = \dfrac{G_1Q}{H - T_\Upsilon} \\ \delta_2 = \dfrac{O_2M_2}{O_2E_2} = \dfrac{G_2E_2}{P_2E_2} = \dfrac{G_2E_2}{H} \end{cases}. \tag{21}$$

879 where T_Υ is the average depth of the seasonal layer at Scarp 1 from the "BOUNDing" approach
880 at Ls $= \Upsilon°$ (Figure 10). What we need to do is determine δ_2 given a known δ_1, satisfying $G_1E_1 \equiv$
881 G_2E_2. From the definition of δ_1, we know

882 $$G_1Q = (H - T_\Upsilon) \times \delta_1\,. \tag{22}$$

883 Then P_1G_1 can be related to G_1Q as

884 $$P_1G_1 = H - T_\Upsilon - \check{T}^{\mathrm{c}}_\Upsilon - G_1Q = H - T_\Upsilon - \check{T}^{\mathrm{c}}_\Upsilon - (H - T_\Upsilon) \times \delta_1\,, \tag{23}$$

885 where $\check{T}^{\mathrm{c}}_\Upsilon$ is the a priori crown depth and we set it to be the median value of the measurements
886 from inspecting the ice blocks with parallel walls (black horizontal lines in Figure 14):

887 $$\check{T}^{\mathrm{c}}_\Upsilon = T^{\mathrm{c}}_\Upsilon\,. \tag{24}$$

888 The ratio δ_2 can be calculated by relating to P_1G_1 and the ratio δ_1 as

889 $$\delta_2 = \frac{H - P_2G_2}{H} = \frac{H - P_1G_1}{H} = \frac{T_\Upsilon + \check{T}^{\mathrm{c}}_\Upsilon + (H - T_\Upsilon) \times \delta_1}{H}\,. \tag{25}$$

890 Taking the extreme of $\delta_1 = 0$, then $\delta_2 = \dfrac{T_\Upsilon + \check{T}^{\mathrm{c}}_\Upsilon}{H}$. Adopting another extreme of $\delta_1 = 1$,
891 then $\delta_2 = \dfrac{H + \check{T}^{\mathrm{c}}_\Upsilon}{H} > 1$ which is reasonable as the width in the summer image cannot be mea-
892 sured. Finally, widths are measured along the traverse lines crossing the shadow measuring points
893 and running perpendicular to the sunlight in the spring (W^1_Υ) and summer images (W^2), re-
894 spectively. The depth of the crown over the ice block can be approximated again by utilizing
895 Equation 17. If $\hat{T}^{\mathrm{c}}_\Upsilon - \check{T}^{\mathrm{c}}_\Upsilon \leq 0.1$ m, then their average is taken as the measured crown depth
896 over the ice block in question, that is $\hat{T}^{\mathrm{c}}_\Upsilon \leftarrow \dfrac{\hat{T}^{\mathrm{c}}_\Upsilon + \check{T}^{\mathrm{c}}_\Upsilon}{2}$. Else, the a priori crown depth is up-
897 dated $\check{T}^{\mathrm{c}}_\Upsilon \leftarrow \hat{T}^{\mathrm{c}}_\Upsilon$ and the iteration is started again to make sure the difference between the a

898 priori value and posterior estimate reduces to within 0.1 m. This approach using the cone-shaped
899 ice blocks pre-requires clear identification of the triangular-shaped shadow boundary and thus
900 permits much less valid estimates than those using the ice blocks with parallel walls. In fact,
901 it is inapplicable to images acquired in late winter and early spring. Here, we only apply this
902 approach to the image acquired at Ls = 42.8° which features the best quality in MY31. We
903 obtain a total of 11 valid measurements that range from 0.22 m to 0.36 m, with a median of
904 0.29 m (blue violin in Figure 14). One of these measurements reaches convergence after two it-
905 erations while all the rest satisfy the stopping criterion after just one iteration. These measure-
906 ments overlap well with those obtained using ice blocks with parallel walls with a median of
907 0.26 m. Meanwhile, the bounding interval in light of the standard error of the median constraint
908 is highly consistent with that from the ice blocks with parallel walls (blue and black dots in Fig-
909 ure 14, respectively). That means the steepness of the ice block walls does not significantly in-
910 fluence the depth of the directly condensed frosts. This conclusion also corroborates our sec-
911 ond assumption that the thickness of the directly condensed frosts is the same over the ice block
912 walls and top, which permits us to use the widening of the ice blocks as a proxy to approximate
913 the depths of the overlying crowns.

914 Eventually, we correct the snowfall thickness measurements from "BOUNDing" in MY31
915 for these direct condensation effects (Figure 16). The total thickness of the seasonal deposits
916 at Ls = Υ° is calculated as follows:

917 $$T_\Upsilon^{\text{sum}} = T_\Upsilon + \hat{T}_\Upsilon^{\text{c}} = \frac{\bar{\Theta}_\Upsilon^{\text{T}} + \bar{\Theta}_\Upsilon^{\text{c}}}{2}, \tag{26}$$

918 with its bounding interval set by treating the snowfall thickness estimates and the crown depths
919 as two independent variables:

920 $$\Theta_\Upsilon^{T_\Upsilon^{\text{sum}}} = \left[T_\Upsilon^{\text{sum}} - \frac{\sqrt{\Delta\Theta_\Upsilon^{\text{T}\,2} + \Delta\Theta_\Upsilon^{\text{c}\,2}}}{2},\ T_\Upsilon^{\text{sum}} + \frac{\sqrt{\Delta\Theta_\Upsilon^{\text{T}\,2} + \Delta\Theta_\Upsilon^{\text{c}\,2}}}{2} \right], \tag{27}$$

921 where $\bar{\Theta}_\Upsilon^{\text{T}}$ and $\Delta\Theta_\Upsilon^{\text{T}}$ denote the average and range of the bounding interval for the snowfall thick-
922 nesses from the "BOUNDing" approach (Equation 13 and Figure 10), respectively. Meanwhile,
923 $\bar{\Theta}_\Upsilon^{\text{c}}$ and $\Delta\Theta_\Upsilon^{\text{c}}$ are the average and range of the crown depth bounding interval by examining
924 the ice blocks with parallel walls (Equation 18 and Figure 14), respectively. For Ls = 350.7°
925 in late winter, there exists no bound interval for the crown depth as there is only one valid es-
926 timate. We then tentatively set its interval range to be two times that at the proximate Ls =
927 7.0°. The bounding intervals from Equation 27 are shown as error bars in Figure 16. The cor-
928 rected thickness stands at 1.63 m with a half interval range of 0.22 m at Ls = 350.7° in late
929 winter, 0.45 m with a half interval range of 0.06 m at Ls = 42.8° in middle spring, and decreases
930 to 0.06 m with a half interval range of 0.05 m at Ls = 69.6° in late spring. A majority of the
931 bounding interval half ranges are less then 0.1 m (Table S4). The offsets between these corrected
932 thicknesses and existing MOLA results are thus significantly reduced. At late winter, our thick-
933 ness estimate of 1.63±0.22 m is ∼0.5 m above that of D. E. Smith et al. (2001) and Xiao, Stark,
934 Schmidt, Hao, Steinbrügge, et al. (2022). However, it is compatible with that of Aharonson et

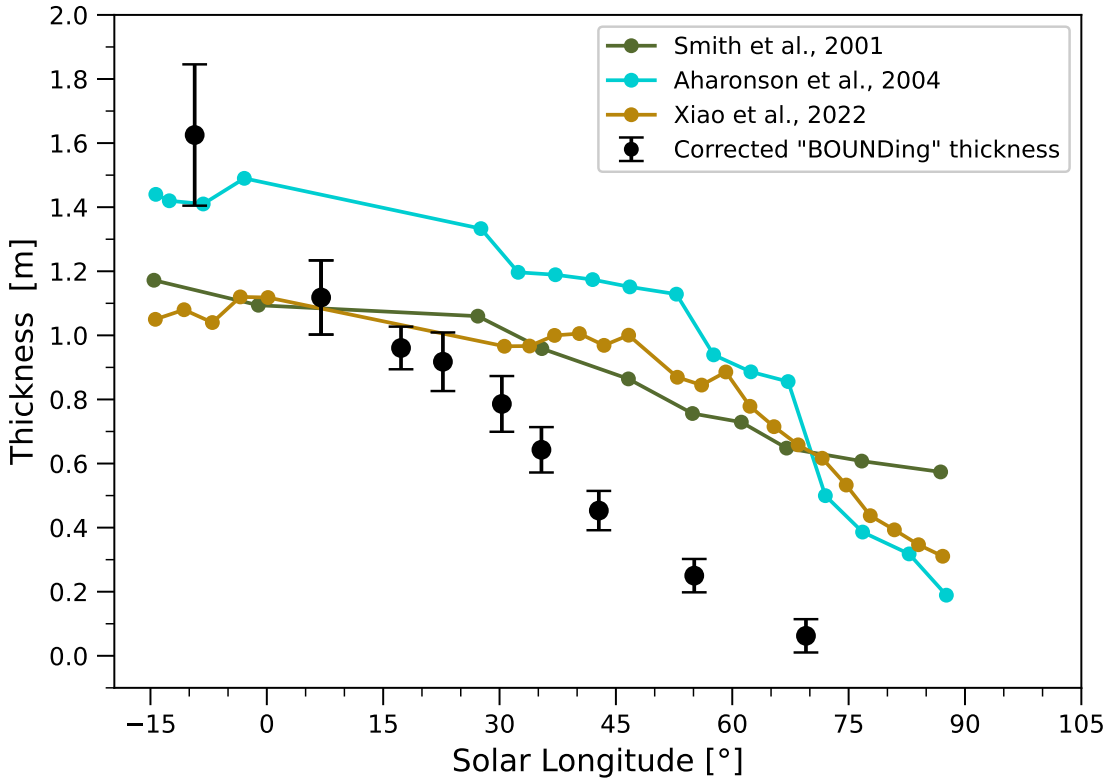

Figure 16: Thickness evolution of the seasonal layer in MY31 from "BOUNDing" after the correction for the crowns over the ice blocks, and their comparison to the existing MOLA results. Uncertainty bars denote the accumulated errors from both the uncorrected thickness measurements and the crown depth estimates. For simplicity and temporal continuity, the constraints obtained at Ls = 350.7° in late winter of MY31 are plotted at Ls = −9.3°.

al. (2004) considering the associated uncertainty of ∼0.2 m. Then, the thickness estimates in this study quasi-linearly decline towards summer solstice. In comparison, the MOLA results decline more gently than ours before Ls =∼ 60° in late spring. The gap between our results and the MOLA ones thus forms at the beginning of sprig and enlarges to be up to 0.8 m at late spring. These lingering offsets and possible reasons behind are thoroughly discussed in the subsequent Section 5.5.

From late winter to spring, the solar elevation angle increases and so does the solar insolation. If assuming the albedo and average density of the seasonal deposits to be constant throughout winter and spring, then the slope of the thickness evolving curve should increase with time. The not-so-varying declining rate of our curve as in Figure 16 thus indicates the combined effects of density variations, like densification due to gravity-induced self-compaction and re-crystallization (Eluszkiewicz et al., 2005; Mount & Titus, 2015; Xiao, Stark, Schmidt, Hao, Steinbrügge, et al., 2022), and albedo variations that take place in the seasonal deposits (Pommerol et al., 2013; Gary-Bicas et al., 2020). Indeed, we note that thickness evolution of the seasonal deposits at the three study sites in Mount & Titus (2015) features distinct trends during the spring: quasi-constant thinning rate at Phoenix's landing site (68°N, 233°E); temporally decelerating thinning rate at a dune field labeled Dunes (75°N, 282°E); temporally accelerating thinning rate at a crater site called Louth (70°N, 103°E).

5.5 Comparison to previous MOLA results

Inconsistencies up to 0.4 m exist between the existing MOLA results (Figures 7 and 10). The difference between the curve of Xiao, Stark, Schmidt, Hao, Steinbrügge, et al. (2022) and that of Aharonson et al. (2004) could mainly be attributed to different post-correction strategies utilized to correct for the global temporal bias in the MOLA dataset. This bias has been observed at all latitudes, and it features a peak-to-peak amplitude of 2 m and a phase that resembles the synodic period of Mars (Xiao, Stark, Steinbrügge, et al., 2022). Xiao, Stark, Schmidt, Hao, Steinbrügge, et al. (2022) corrected for the bias assuming it to be constant at the North Pole and equals that obtained at annulus 50°N. In contrast, Aharonson et al. (2004) parameterized the systematic biases of the MOLA tracks by 3D overlapping polynomials and inverted the coefficients by minimizing height residuals at cross-overs equatorward of 57°S/N and that acquired within 15 Earth days in the North Pole. Essentially, their correction for this global temporal bias at the North Pole was extrapolated from the polynomials fitted within 57°S/N. D. E. Smith et al. (2001) differentiated the thickness variation in each polar annulus to that acquired at 60°S/N to correct for the global temporal bias. Their thickness variation is surprisingly lower compared to the other MOLA results, which may arise from additional smoothing they have applied. Unfortunately, Xiao, Stark, Steinbrügge, et al. (2022) confirmed latitude-dependence of the global temporal bias in the MOLA heights, and the simple treatment of it by assuming it to be constant in the polar regions can introduce temporal bias into the MOLA

thickness evolution curves. It is imperative that we pin down the root cause for this global temporal bias and correct the MOLA heights for it at the local scale in the future.

After the correction for direct condensation effects, offsets up to ∼0.8 m in magnitude between the results using shadowing of the ice blocks and the available MOLA results can still be observed during the spring of MY31 (Section 5.4). Here we discuss several aspects that could possibly be responsible for these offsets: (1) Discrepancies in geographical and year-to-year coverage that exist between the results. Result from D. E. Smith et al. (2001) represents the average pattern at latitudinal annulus 85.5°N, and that of Aharonson et al. (2004) at latitudinal annulus 86°N. Meanwhile, result from Xiao, Stark, Schmidt, Hao, Steinbrügge, et al. (2022) is representative of thickness evolution at a grid element of size 0.5° in latitude and 10° in longitude. Furthermore, MOLA results date back to MY24/25 while results in this study are from MY29 to MY36. Therefore, geographical differences and inter-annual variability might partially contribute to the offsets; (2) Biases related to the MOLA results. Wang & Ingersoll (2002) made a map of the north polar regions of Mars using the Mars Global Surveyor (MGS) Mars Orbiter Camera (MOC) wide-angle swaths at Ls = 111° right after the summer solstice in MY25. No apparent seasonal deposits can be observed at that time outside of the NPLDs. Meanwhile, Piqueux et al. (2015) carried out continuous tracking of the SNPC edges at multiple Mars Years using MGS Thermal Emission Spectrometer (TES) and showed that it completely sublimated away at around Ls = 80° in late spring of MY25. Thus, the biases are at least ∼0.60 m (D. E. Smith et al., 2001), ∼0.35 m (Aharonson et al., 2004), and ∼0.41 m (Xiao, Stark, Schmidt, Hao, Steinbrügge, et al., 2022) for these MOLA results, respectively. In fact, various complicated processes can affect and bias the MOLA results, for example, pulse saturation due to high albedo of the polar ice, the absence of a variable gain amplifier, and limited recording digital ranges (Neumann et al., 2001, 2003), interference of the laser pulses with dynamic and rough surface, incomplete correction for the global temporal bias, and penetration of the laser pulses into the translucent and sloped slab ice (Xiao, Stark, Schmidt, Hao, Steinbrügge, et al., 2022). Unfortunately, each of these listed factors is difficult to model and quantify; (3) Interannual variations. Possible variations in the quantities of snowfalls and frosts can exist between MY24/25 (acquisition time of MOLA footprints) and MY31 (for example, Figure 12). However, these multiyear variations should generally decrease with time in spring as the seasonal layer thins and finally vanishes, which contradicts the observed temporal evolution of the offset. To conclude, there exists strong evidence to argue that a large portion of these discrepancies result from biases inherited in the MOLA dataset.

5.6 Comparison to predicted snowfall quantities

In this section, we discuss our measured snowfall thickness as compared to that predicted by a simple CO_2 cloud settling model using atmospheric profiles acquired by MCS onboard the MRO (Alsaeed & Hayne, 2022). We now know that the snowfall rates are significantly larger

in the north than those in the south, because the former features larger surface air pressure and a thicker water ice polar hood that can serve as condensation nuclei for the CO_2 snowfalls (Gary-Bicas et al., 2020; Alsaeed & Hayne, 2022). Alsaeed & Hayne (2022) concluded that the CO_2 snowfall equivalent thickness accumulated throughout fall and winter is on the order of several millimeters poleward of 65°N. Surprisingly, these theoretical values are two orders of magnitude smaller than the measured ∼0.97±0.13 m thick snow layer during late winter at Scarp 1. The depth of ∼0.97±0.13 m due to snowfalls even significantly exceeds that of the frost layer due to direct condensation (0.64±0.18 m m at late winter). However, it's worth mentioning that there exist gaps in the MCS data in the lowest atmosphere (approximately up to 5 km in altitude) where the instrument cannot probe through the optically thick clouds. This means that the effects of localized storms which can rapidly drive up snowfall rates were not captured in Alsaeed & Hayne (2022). In addition, zonal averaging applied in the MCS analysis can further erase out local aggregation of the snowfalls. Thus, the theoretical thickness values from Alsaeed & Hayne (2022) can only be considered as the lower limits. Then, it should be interesting to obtain snowfall thicknesses at active scarps over the entire North Pole (Section 5.7) and check if our measurements are consistently way higher than the modeled ones. If yes, that would mean the snowfalls on Mars are much more frequent and violent than we thought and the cloud settling model applied by Alsaeed & Hayne (2022) is missing some important ingredients. As the condensed water ice particles serve as condensation nuclei for the CO_2 particles during atmospheric deposition, higher CO_2 snowfall rates then mean a larger fraction of the Martian water cycle happens through this scavenging mechanism at the poles.

5.7 Availability of ice blocks across the North Pole

Here we discuss the spatial availability of the ice blocks as to examine the maximum coverage of upcoming mass-application of the proposed approaches.

Russell et al. (2010, 2012) examined HiRISE images covering ∼70 Basal Unit outcrops around the NPLDs for scattered ice blocks and debris on Basal Unit slopes, and qualitatively grouped a total of 20 potentially active outcrops into three categories in terms of "likelihood of recent mass-wasting activity". None of the peripheral scarps without Basal Unit exposure features likely mass-wasted NPLD detritus at their base (Russell et al., 2012). This indicates an important role the Basal Unit may play in steepness of the scarps and the related mass wasting processes. These active scarps are spatially limited to be within 80°N and 85°N. In addition, there exists no active scarps in Gemina Lingula and Gemini Scopuli due to the lack Basal Unit outcrops (Fishbaugh & Head III, 2005; Nerozzi et al., 2022). However, the number of HiRISE observations available was relatively small back then in 2012.

We seek to carry out a comprehensive search for scarps with ice blocks where our approach can be potentially applicable to get insights into the condensation/sublimation cycle of the polar seasonal deposits. The search is done by merely examining the available HiRISE images.

Note that there also exist other optical images captured by Mars Express's High Resolution Stereo Camera (HRSC; Neukum & Jaumann, 2004), the MRO Context Camera (CTX; Malin et al., 2007), and the ExoMars Trace Gas Orbiter (TGO) Colour and Stereo Surface Imaging System (CaSSIS; N. Thomas et al., 2017). However, the best resolution of these images can range from 4 to 12.5 m/pixel, which is not enough to even capture the ice blocks with maximum size of ∼5 m (Fanara et al., 2020b). The search combines two aspects of efforts: (1) We locate all of the sites over the NPLDs and their close vicinity where have been observed for at least five times, and randomly select a summer image for visual inspection of fallen ice blocks. Multiple images of the same sites can facilitate the cross-validation of the obtained snow/ice thickness values and enable insights into the interannual depth variations (Section 5.3). It should be noted that these regions of interest are not limited to steep marginal scarps, but can also cover spiral troughs that expose stratigraphic layers (Figure 4), ice-filled craters over the residual polar cap, dynamic dune fields, and so forth; (2) We make use of the topographic information from a reference DEM gridded from updated and adjusted MOLA profiles (Xiao, Stark, Schmidt, Hao, Steinbrügge, et al., 2022), and examine all available summer images that overlap with indicated sloped surfaces (with slope greater than an empirical threshold of 15°). If there are visible ice blocks, then we mark the corresponding scarp as positive. We set no height constraints on the ice blocks as they should be at least tall enough to resolve the thin layer of seasonal deposits during middle-to-late northern spring. Actually, the pixel size of HiRISE (down to 0.25 m) limits the detection of ice blocks and shadows under 0.71 m in size and length, respectively ($2\sqrt{2}$=2.83 pixels). Thus, the images themselves have already filtered out small ice blocks. In reality, there should exist a large quantify of these small blocks, as indicated by the frequency-size distribution of detected newly-fallen ice blocks, which generally follows a power law (Fanara et al., 2020b).

The reference DEM is derived based on the co-registration technique (Gläser et al., 2013; Stark et al., 2015). We apply the concept of "self-registration" to improve the positioning of individual laser profiles. A random subset of laser profiles (fixed at 0.25) is selected and then co-registered to a footprint point cloud formed from the remaining profiles. After enough repeats (set to 30), we effectively remove all offsets between the profiles due to residual errors in laser alignment calibration, spacecraft attitude, timing, and trajectory. In Text S1, we perform a probabilistic analysis on the number of iterations needed to be performed in the self-registration process which justifies the repeats for up to 30 times. The DEM is gridded with 1 km in pixel size and cannot fully resolve steep scarps (normally with a width of some hundreds of meters in the images or less depending on the steepness), instead the indicated slopes are average representative over large-scale topography, for example, the transition zone between NPLDs and Basal Unit. The DEM pixels with slope greater than an empirical threshold of 15° are shown in Figure 17. This relatively low threshold is set to ensure that all scarps with ice block presence will lie in the search path. The extracted sloped surfaces include the marginal scarps, with heights that range from 200 m to more than 1,200 m, delineated by Massé et al. (2012). Indeed, this

relatively low threshold also leads to plenty of instances of spiral troughs being indicated as candidates to search for ice blocks.

We locate 138 sites of which there are, at least, 5 different observations and an additional of 210 sites, a majority of which feature no repeated observation or with only one extra coverage, along the sloped surfaces indicated by the MOLA terrain model. The summer images at those sites are manually examined and the ones with presence of ice blocks are shown in Figure 17. A total of 66 images over various locations show signs of recent activity (39 out of 138 and 27 out of 210 from the two categories, respectively). Active scarps with more than or equal to 5 repeated observations cluster in Olympia Rupes (including Scarp 1), Abalos Scopuli, and Boreum Cavus together with Tenius Cavus within Chasma Boreale. Apart from Olympia Rupes and Chasma Boreale, active scarps located through slope indicator extend to Rupes Tenuis and Gemini Scopuli. However, it's worth mentioning that the scarps at Olympia Rupes, Abalos Scopuli, and Chasma Boreale are much more dynamic than those at the other places, as indicated by the large number of aprons of debris and ice blocks spotted there. These mass-wasting activities are spatially correlated with Basal Unit exposure at their base (compare to Figure 2 in Nerozzi et al. (2022)). In contrast, scarps along Rupes Tenuis lack apparent aprons of debris but ice blocks reside right at the layered terrain of the scarps (refer to Inset 1 in Figure 17 for an example). Actually, Rupes Tenuis itself belongs to the exposed Basal Unit, and not the NPLDs. However, to prevent unnecessary confusion, we do not attempt to distinguish these scarps from those of the NPLDs. Scarps in Gemini Scopuli over Gemina Lingula also lack aprons of debris, and ice blocks are large in quantity and extremely uniformly-distributed at close vicinity of the scarps (refer to Inset 2 in Figure 17 for an example). Comparing the summer images in MY29 and MY36 at the location of Inset 2 shows no apparent fracture-caused detachment of fragments over the scarp, indicating these ice blocks, being contiguous to the scarp, may be anteriorly emplaced. The scarps with visible ice blocks spatially cover latitudes from 78°N to 86°N. In terms of longitude, there exist a major gap from 27°E to 117°E over the Gemini Scopuli where Udzha Crater (81.8°N, 75.0°E) is the only site that has been spotted with ice blocks (refer to Figure 17 for location). It should be noted that the complete set of HiRISE images that have been examined do not cover all of the scarps. When searching through the images, only the ones acquired in the summertime have been downloaded and inspected. Additionally, there exist gaps in HiRISE coverage of the scarps which can be expected to be gradually bridged as more upcoming observations have been planned. As such, the set of scarps with presence of ice blocks presented in Figure 17 should stand as the lower limit on the maximum spatial extend of the expected outputs by the proposed approaches.

With ice blocks being spatially limited to high latitudes where the thickest seasonal layer is expected (Xiao, Stark, Schmidt, Hao, Steinbrügge, et al., 2022; Gary-Bicas et al., 2020), rocks at regions surrounding the north polar cap, either over the crater rims or between the dune fields in the polar erg, and at lower latitudes can also be utilized for the purpose of measuring the

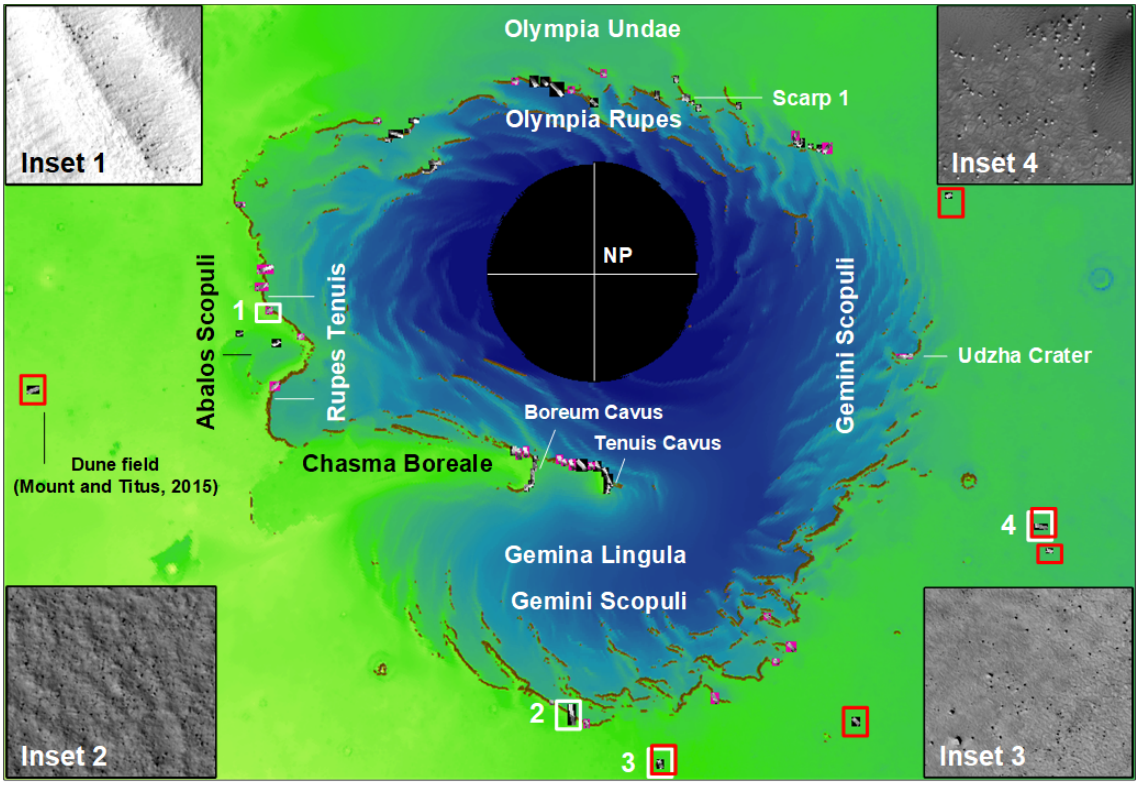

Figure 17: Locations of scarps with presence of ice blocks as examined in the HiRISE images. Locations with slope greater than 15°, represented by dark orange points, are draped over the 1 km/pixel reference DEM from reprocessed and then self-registered MOLA profiles (Xiao, Stark, Schmidt, et al., 2021). Images with the presence of ice blocks at locations where at least five repeated observations have been made by the HiRISE camera are shown with black background. Meanwhile, images examined to feature ice blocks along troughs and scarps indicated by MOLA slope map are exhibited with pink background. Images enclosed by white rectangles are taken as examples and enlarged in the corresponding insets to show the present ice blocks (Insets 1 and 2) and rocks (Insets 3 and 4), respectively. Images enclosed by red rectangles are examples with the presence of rocks in the circumpolar regions, including the polar erg, that is, massive dune fields surrounding the NPLDs. The barchanoid dune field with rocks at (75°N, 282°E), studied in Mount & Titus (2015) to infer the depth of the seasonal deposits, is marked. Names of regions that feature clusterings of scarps with ice blocks are annotated. The Udzha Crater is marked of which only the topmost sharp-edged rims rise above the polar layered deposits to hint at its circular shape. Scarp 1 studied in this paper is also marked for reference.

thickness of the seasonal layer (Cull et al., 2010; Mount & Titus, 2015). Some typical rock sites are enclosed by red rectangles in Figure 17, with Insets 3 and 4 showing zoom-in views of the rocks over the crater rim and between the dune fields, respectively. For large boulders over the craters and their vicinity, they could be ejected during the impacts. The dune field, named Dunes, within which the rocks have been utilized in Mount & Titus (2015) to infer the thickness of the seasonal deposits there is also taken as an example. Unfortunately, no rocks have been spotted between the massive linear dune fields in Olympia Undae where maximum depth up to ∼4 m and off-season thickness variations up to ∼3 m in magnitude have been claimed after examining the dynamic MOLA height records (Xiao, Stark, Schmidt, Hao, Steinbrügge, et al., 2022). Instead, lingering patches of bright materials between the dunes have been spotted which can persist throughout the northern summer. Early evidence suggested that they show more gypsum than water ice signatures (Fishbaugh et al., 2007; Horgan et al., 2009). In addition to gypsum, there might exist other evaporitic minerals as small interannual variations of these bright patches have also been observed.

By establishing the automatic "BOUNDing" approach to circumvent massive demands on human resources and applying it to all available sites with ice blocks and rocks in the polar region, we can obtain good spatial samplings of the thickness evolution of the seasonal deposits and shed comprehensive insights into the long-term vertical growth and retreat of the SNPC. In particular, these results can be used to examine the question that if the seasonal deposits are much shallower than the MOLA-derived results during springtime over the entire Martian North Pole (Section 5.5)? If yes, that means the the average bulk density of the seasonal deposits in spring should be much higher than we thought, which can have implications for snow/ice metamorphism and translucency of the deposits (for example, Eluszkiewicz et al., 2005; Matsuo & Heki, 2009; Mount & Titus, 2015; Xiao, Stark, Schmidt, Hao, Steinbrügge, et al., 2022). The expected measurements can also shed light on the spatially variable proportions of direct condensation as frosts and atmospheric precipitation as snowfalls in forming the seasonal layer. These proportions can help determine if CO_2 snowing storms are much more frequent and violent than we thought (Section 5.6). Meanwhile, "SUBTRACTing" can be applied to specific (relatively tall) ice blocks to look into the thickness evolution at individual spots of interest. Possible significant interannual depth variations with magnitudes of more than 0.2 m can be identified and interpreted in the context of Martian climate change. Those enhanced understandings can place crucial constraints on the Martian volatile cycles and climate models (for example, Mischna et al., 2003; Forget et al., 2013). Meanwhile, the thickness of the seasonal layer can assist in designing of future landers, rovers, or helicopters that are to drill in the spiral troughs and decipher the Late Amazonian climate of Mars stored in the NPLDs (I. B. Smith et al., 2020; Matthies et al., 2022).

5.8 Limitations and outlook

Spatially and temporally inhomogeneous growth and retreat of the seasonal polar caps have been identified and analyzed over various seasons using the MOLA records (Xiao, Stark, Schmidt, Hao, Su, et al., 2022; Xiao, Stark, Schmidt, Hao, Steinbrügge, et al., 2022). Unfortunately, a realistic error propagation is not possible without ground truth for assessment. As a result, the unexpected features observed, for example, exceptionally high maximum depth (∼4 m) and off-season depth trends observed within Olympia Undae, remain to be verified from independent dataset. Indeed, current accuracy assessment of the MOLA results rely merely on indirect evidence, for example, cross-validation of results from various teams or deviations from expected values (normally zero) at specific regions and solar longitudes (D. E. Smith et al., 2001; Aharonson et al., 2004; Xiao, Stark, Schmidt, Hao, Su, et al., 2022; Xiao, Stark, Schmidt, Hao, Steinbrügge, et al., 2022). The large biases in MOLA-derived results during spring as stated in Section 5.5 stress the importance of proper calibration of the MOLA results.

Although temporally limited to late winter and spring (Section 4) and spatially confined to high latitudes (Section 5.7), the results by inspecting the ice blocks and rocks over the North Pole in HiRISE images can serve to calibrate the existing MOLA results. Then, extrapolation of the calibrated MOLA results to uncovered latitudes can be implemented in combination of boundary constraints, for example, CROCUS dates from optical cameras and thermal infrared spectrometers (for example, Schmidt et al., 2009; Piqueux et al., 2015). The term introduced by Kieffer et al. (2000), is a helpful mnemonic marker, which identifies the time in spring at which the snow/ice has completely disappeared. Meanwhile, these expected results can serve as ground truth for validating the processing procedure of the SHARAD radar sounding and altimetric measurements for the purpose of looking into the depth evolution of the seasonal deposits. These radar records harbor the potential to decipher long-term depth evolution patterns of both seasonal polar caps of Mars (for example, Raguso & Nunes, 2021; Steinbrügge et al., 2021). As an ongoing activity, we seek to establish and apply the automatic "BOUNDing" approach to HiRISE images acquired over all active scarps and at fields with presence of rocks at the Martian North Pole (Section 5.7). Meanwhile, we also advocate for more future observations of the HiRISE camera of the active scarps and circumpolar rock fields at the North Pole, including stereo pairs.

The depth evolution curves from "SUBTRACTing" and "BOUNDing" can achieve an uncertainty of better than 0.1 m at best scenarios, which is mainly limited by the spatial resolution of the HiRISE camera (down to 0.25 m). This dictates that delicate interannual variations, for example, less than ∼0.2 m, cannot be confidently detected at the current stage. Thus, future super-resolution cameras to orbit Mars would dramatically enhance the performance of the proposed approaches to delve into the snow/ice depth evolution patterns. Indeed, the Mars Next Orbiter Science Analysis Group (NEX-SAG) already identified a baseline instrument of a super-high-resolution optical imager (HiRISE class at 30 cm/pixel; or even with a better res-

olution of 10 – 15 cm/pixel) to reveal detailed morphology over limited areas for science and site reconnaissance (Zurek et al., 2021). This recommended imager is capable of, for example, capturing stratigraphic details, and thus the Late Amazonian climate records, stored in the polar layered deposits (I. B. Smith et al., 2020) and better observing various surface dynamics such as those related to slopes (Dundas et al., 2021).

Using MOLA-measured thickness variations of the seasonal deposits from Xiao, Stark, Schmidt, Hao, Su, et al. (2022) and Xiao, Stark, Schmidt, Hao, Steinbrügge, et al. (2022), Wagner et al. (2023) modeled the loading-induced lithospheric deflection based on mechanical properties of the Martian interior. They found that the deflection can be up to ∼6 cm in magnitude at the poles and can be unambiguously detected by upcoming Interferometric Synthetic Aperture Radars (InSARs) or next-generation laser altimeters. We note that the thickness variations of the seasonal deposits from MOLA altimetric records were retrieved by examining the surface height changes, which actually represent the combined effects of CO_2 deposition/sublimation and the resultant lithospheric deflection. In contrast, thickness measurements from "SUBTRACTing" and "BOUNDing" are obtained by examining the shadows of the ice blocks and thus remain unaffacted by the lithospheric deflection. It is anticipated that we can extract the periodic lithospheric deflection by comparing the surface height variations from future InSARs or laser altimeters with the seasonal deposit thicknesses from examining the ice blocks. Constraints on the lithospheric deflection can inform us about the structure and rheology of the Martian crust and mantle which have important implications for Mars' thermal history. It will be challenging to differentiate between currently plausible Mars interior models as the precision in measuring the deflection would need to be in the millimeter or even sub-millimeter level (Wagner et al., 2023). However, this proposed concept does harbor some potential by including a large amount of independent surface height variation and snow/ice depth measurements for spatial and temporal averaging purposes. The fact that the lithospheric deflection peaks at high polar latitudes where ice blocks are located further enhances the feasibility of the measuring concept. Meanwhile, a future super-high-resolution optical imager to Mars would greatly build up the prospects (Zurek et al., 2021). A factor that will need to be considered and throughly modeled in the determination of the subtle lithospheric deflection is the solid body tidal deformation from the Sun and Phobos which maximizes at around the equator and reduces to less than 1 cm at the poles (Wagner et al., 2023).

6 Conclusion

We propose to use the shadow variations of the ice blocks at the foot of the NPLD steep scarps, complementing that of the rocks, to infer the vertical evolution of the Martian seasonal deposits. We relate the shadow length of an ice block to its height using a rigorous geometric model, which is based on bundle adjusted and orthorectified high-resolution HiRISE images and takes both the solar and slope properties into consideration. Building on this model, we present

two independent and yet complementary approaches: (1) "SUBTRACTing" that subtracts the ice block heights in the summer to that observed in the spring; (2) "BOUNDing" that locates ice blocks that have been completely covered to place lower limits on the thickness of the seasonal deposits, and ice blocks that still stick out of the seasonal cover to put upper limits. We experimentally apply the methods to a steep scarp centered at (85.0°N, 151.5°E). The results show that the average thickness due to accumulation of snowfalls in MY31 is 0.97±0.13 m at Ls = 350.7° in late winter, 0.64±0.08 m at Ls = 7.0° in early spring, 0.21±0.05 m at Ls = 42.8° in middle spring, and gradually decreases towards summer solstice (Ls = 90°). The maximum snowfall thickness of ∼1 m is two orders of magnitude larger than theoretical values predicted by Alsaeed & Hayne (2022). We proceed to make reasonable assumptions and use the widening of the ice blocks as a proxy to approximate the depth of the directly condensed layer over the ice blocks. We show that average thickness of the frost layer in MY31 reaches 0.64±0.18 m at Ls = 350.7° in late winter, quasi-linearly declines to 0.26±0.03 m at Ls = 42.8° in middle spring and to 0.045±0.035 m at Ls = 69.5° in late spring. We thus show that atmospheric deposition as snowfalls, compared to direct surface condensation as frosts, can even contribute more to the thickness and volume of the seasonal snow/ice layer at Scarp 1 during wintertime. The aggregate thickness of the seasonal deposits at Scarp 1 in MY31 then stands at 1.63±0.22 m at Ls = 350.7° in late winter which then gradually declines to 0.45±0.06 m at Ls = 42.8° in middle spring and 0.06±0.05 m at Ls = 69.5° in late spring. The majority of the associated uncertainties can be better than ∼0.1 m. Compared to the existing MOLA results, our thickness estimates are consistently lower, by a magnitude of up to 0.8 m, throughout the spring. We attribute a large portion of these inconsistencies to biases inherited in the MOLA-derived thickness measurements. The available HiRISE images can temporally span from MY29 to MY36 (2008 to 2021), and we observe the snowfall thickness in the very early spring in MY36 is 1.01±0.10 m, exceeding that in MY31 by a magnitude of 0.36±0.13 m. Building on this study, we will develop automatic version of the approaches and extend the measurements to all scarps with presence of ice blocks, covered by multiple HiRISE images at the same time, at the Martian North Pole. Meanwhile, we will also apply the proposed approaches to the circumpolar regions with presence of rocks to extend the thickness evolution measurements to lower polar latitudes. These expected results can answer the raised question that if the seasonal cap over the entire Martian North Pole during its recession in spring is much shallower than we previously thought? Meanwhile, the proportions of snowfall and frosts in constituting the seasonal deposits over the entire polar region can be expected to be revealed. These future results can also serve as ground truth to calibrate previous MOLA results and validate contemporary anticipated SHARAD results. Besides, these expected outcomes can help to examine the long-term spatial-temporal heterogeneity of the surface-atmosphere exchange and determine the mass balance of the NPLDs. As such, we suggest more frequent targeting of the HiRISE camera to the active scarps where ice blocks exist and circumpolar fields with presence of rocks. Meanwhile, anticipated super-high-resolution optical cameras to Mars would enable unambiguous identification of small in-

terannual depth variations, for example, less than 0.2 m in magnitude, of the seasonal deposits. Thickness measurements from examining the ice blocks, in combination with high-precision surface height variations from future InSARs or laser altimeters, have the potential of inferring the polar dynamic lithospheric deflection which can shed light on the Martian interior.

Acknowledgments

The authors would like to thank Nicholas L. Wagner (Baylor University) and Noora R. Alsaeed (University of Colorado Boulder) for helpful discussions. We also acknowledge the MRO and HiRISE teams for providing the great products that enabled this research. SS thanks the China Scholarship Council (CSC) for financial support of studying in Germany. FS acknowledges support from the "Institut National des Sciences de l'Univers" (INSU), the "Centre National de la Recherche Scientifique" (CNRS), and "Centre National d'Etudes Spatiales" (CNES) through the "Programme National de Planétologie." LML and PJG acknowledge financial support from project PID2021-126365NB-C21 (MCI/AEI/FEDER, UE) and from the grant CEX2021-001131-S funded by MCI/AEI/ 10.13039/501100011033.

Author contributions

Conceptualization: HX; **Formal Analysis**: HX, FS, and PJG; **Funding Acquisition**: HX; **Investigation**: HX and YX; **Methodology**: HX, FS, and PJG; **Project Administration**: HX; **Software**: HX and SS; **Visualization**: HX and YX; **Supervision**: HX, PJG, FS, and LML; **Validation**: HX; **Writing – original draft**: HX; **Writing – review & editing**: HX, SS, PJG, FS, and LML.

Conflict of Interest

The authors declare no conflicts of interest relevant to this study.

Open Research

HiRISE images are available at https://www.uahirise.org/hiwish/browse and https://ode.rsl.wustl.edu/mars/ (accessed on 20 December 2022). The self-registered MOLA reference DEM and thickness variation time series from Xiao, Stark, Schmidt, Hao, Steinbrügge, et al. (2022) at the North Pole are published under https://doi.org/10.17632/x953mzxxvv.1 (Xiao, Stark, Schmidt, et al., 2021, accessed on 12 May 2023). The SPICE kernels used for calculation of the solar condition are available at https://naif.jpl.nasa.gov/pub/naif/pds/data/mgs-m-spice-6-v1.0/mgsp_1000/data/ (accessed on 18 March 2023).

References

Acton, C. H. J. (1996). Ancillary data services of NASA's Navigation and Ancillary Information

Facility. *Planetary and Space Science*, *44*(1), 65-70. doi: 10.1016/0032-0633(95)00107-7

Aharonson, O., Zuber, M. T., Smith, D. E., Neumann, G. A., Feldman, W. C., & Prettyman, T. H. (2004). Depth, distribution, and density of CO_2 deposition on Mars. *Journal of Geophysical Research: Planets*, *109*(E5). doi: 10.1029/2003JE002223

Alsaeed, N., & Hayne, P. O. (2022). Transport of water into the polar regions of Mars through scavenging by CO_2 snowfall. *Journal of Geophysical Research: Planets*, *127*(11), e2022JE007386. doi: 10.1029/2022JE007386

Andrieu, F., Schmidt, F., Douté, S., & Chassefière, E. (2018). Ice state evolution during spring in Richardson crater, Mars. *Icarus*, *315*, 158–173. doi: 10.1016/j.icarus.2018.06.019

Appéré, T., Schmitt, B., Langevin, Y., Douté, S., Pommerol, A., Forget, F., ... Bibring, J.-P. (2011). Winter and spring evolution of northern seasonal deposits on Mars from OMEGA on Mars Express. *Journal of Geophysical Research: Planets*, *116*(E5). doi: 10.1029/2010JE003762

Becerra, P., Smith, I. B., Hibbard, S., Andres, C., Bapst, J., Bramson, A. M., ... Yoldi, Z. (2021). Past, present, and future of Mars polar science: Outcomes and outlook from the 7th International Conference on Mars Polar Science and Exploration. *Planetary Science Journal*, *2*(5), 209. doi: 10.3847/PSJ/ac19a5

Becerra, P., Sori, M. M., & Byrne, S. (2017). Signals of astronomical climate forcing in the exposure topography of the North Polar Layered Deposits of Mars. *Geophysical Research Letters*, *44*(1), 62–70. doi: 10.1002/2016GL071197

Benson, J. L., Kass, D. M., & Kleinböhl, A. (2011). Mars' north polar hood as observed by the Mars Climate Sounder. *Journal of Geophysical Research: Planets*, *116*(E3). doi: 10.1029/2010JE003693

Beyer, R. A., Alexandrov, O., & McMichael, S. (2018). The Ames Stereo Pipeline: NASA's open source software for deriving and processing terrain data. *Earth and Space Science*, *5*(9), 537–548. doi: 10.1029/2018EA000409

Blackburn, D. G., Bryson, K. L., Chevrier, V. F., Roe, L. A., & White, K. F. (2010). Sublimation kinetics of CO_2 ice on Mars. *Planetary and Space Science*, *58*(5), 780–791. doi: 10.1016/j.pss.2009.12.004

Botev, Z. I., Grotowski, J. F., & Kroese, D. P. (2010). Kernel density estimation via diffusion. *Annals of Statistics*, *38*(5), 2916-2957. doi: 10.1214/10-AOS799

Brothers, S., Kocurek, G., & Holt, J. (2018). Sequence architecture of the cavi unit, Chasma Boreale, Mars. *Icarus*, *308*, 42–60. doi: 10.1016/j.icarus.2017.06.024

Brothers, T., Holt, J., & Spiga, A. (2015). Planum Boreum basal unit topography, Mars: Irregularities and insights from SHARAD. *Journal of Geophysical Research: Planets*, *120*(7), 1357–1375. doi: 10.1002/2015JE004830

Brown, A. J., Calvin, W. M., Becerra, P., & Byrne, S. (2016). Martian north polar cap summer water cycle. *Icarus*, *277*, 401–415. doi: 10.1016/j.icarus.2016.05.007

Byrne, S., Sori, M., Russell, P., Pathare, A., Becerra, P., Molaro, J., ... Team, H. (2017). Mars polar cliffs: Stressed out and falling apart. In *European Planetary Science Congress* (Vol. 11).

Calvin, W., James, P., Cantor, B., & Dixon, E. (2015). Interannual and seasonal changes in the north polar ice deposits of Mars: Observations from MY 29–31 using MARCI. *Icarus*, *251*, 181–190. doi: 10.1016/j.icarus.2014.08.026

Cull, S., Arvidson, R. E., Mellon, M., Wiseman, S., Clark, R., Titus, T., ... McGuire, P. (2010). Seasonal H_2O and CO_2 ice cycles at the Mars Phoenix landing site: 1. Prelanding CRISM and HiRISE observations. *Journal of Geophysical Research: Planets*, *115*(E4). doi: 10.1029/2009JE003340

Defraigne, P., de Viron, O., Dehant, V., Van Hoolst, T., & Hourdin, F. (2000). Mars rotation variations induced by atmosphere and ice caps. *Journal of Geophysical Research: Planets*, *105*(E10), 24563–24570. doi: 10.1029/1999JE001227

Dundas, C. M., Becerra, P., Byrne, S., Chojnacki, M., Daubar, I. J., Diniega, S., ... Valantinas, A. (2021). Active Mars: A dynamic world. *Journal of Geophysical Research: Planets*, *126*(8), e2021JE006876. doi: 10.1029/2021JE006876

Eluszkiewicz, J., Moncet, J.-L., Titus, T. N., & Hansen, G. B. (2005). A microphysically-based approach to modeling emissivity and albedo of the Martian seasonal caps. *Icarus*, *174*(2), 524–534. doi: 10.1016/j.icarus.2004.05.025

Fanara, L., Gwinner, K., Hauber, E., & Oberst, J. (2020a). Automated detection of block falls in the north polar region of Mars. *Planetary and Space Science*, *180*, 104733. doi: 10.1016/j.pss.2019.104733

Fanara, L., Gwinner, K., Hauber, E., & Oberst, J. (2020b). Present-day erosion rate of north polar scarps on Mars due to active mass wasting. *Icarus*, *342*, 113434. doi: 10.1016/j.icarus.2019.113434

Fishbaugh, K. E., & Head III, J. W. (2005). Origin and characteristics of the Mars north polar basal unit and implications for polar geologic history. *Icarus*, *174*(2), 444–474. doi: 10.1016/j.icarus.2004.06.021

Fishbaugh, K. E., Poulet, F., Chevrier, V., Langevin, Y., & Bibring, J.-P. (2007). On the origin of gypsum in the Mars north polar region. *Journal of Geophysical Research: Planets*, *112*(E7). doi: 10.1029/2006JE002862

Forget, F., Wordsworth, R., Millour, E., Madeleine, J.-B., Kerber, L., Leconte, J., ... Haberle, R. M. (2013). 3D modelling of the early Martian climate under a denser CO_2 atmosphere: Temperatures and CO_2 ice clouds. *Icarus*, *222*(1), 81–99. doi: 10.1016/j.icarus.2012.10.019

Gary-Bicas, C., Hayne, P., Horvath, T., Heavens, N., Kass, D., Kleinböhl, A., ... McCleese, D. (2020). Asymmetries in snowfall, emissivity, and albedo of Mars' seasonal polar caps: Mars Climate Sounder observations. *Journal of Geophysical Research: Planets*, *125*(5), e2019JE006150. doi: 10.1029/2019JE006150

Gläser, P., Haase, I., Oberst, J., & Neumann, G. A. (2013). Co-registration of laser altimeter

tracks with digital terrain models and applications in planetary science. *Planetary and Space Science*, *89*, 111–117. doi: 10.1016/j.pss.2013.09.012

Golombek, M. P., Huertas, A., Marlow, J., Mcgrane, B., Klein, C., Martinez, M., ... Tamppari, L. K. (2008). Size-frequency distributions of rocks on the northern plains of Mars with special reference to Phoenix landing surfaces. *Journal of Geophysical Research: Planets*, *113*(E3). doi: 10.1029/2007JE003065

Grima, C., Kofman, W., Mouginot, J., Phillips, R. J., Hérique, A., Biccari, D., ... Cutigni, M. (2009). North polar deposits of Mars: Extreme purity of the water ice. *Geophysical Research Letters*, *36*(3). doi: 10.1029/2008GL036326

Hansen, C., Byrne, S., Portyankina, G., Bourke, M., Dundas, C., McEwen, A., ... Thomas, N. (2013). Observations of the northern seasonal polar cap on Mars: I. Spring sublimation activity and processes. *Icarus*, *225*(2), 881–897. doi: 10.1016/j.icarus.2012.09.024

Hansen, C., Thomas, N., Portyankina, G., McEwen, A., Becker, T., Byrne, S., ... Mellon, M. (2010). HiRISE observations of gas sublimation-driven activity in Mars' southern polar regions: I. Erosion of the surface. *Icarus*, *205*(1), 283–295. doi: 10.1016/j.icarus.2009.07.021

Hayward, R., Fenton, L., Tanaka, K., Titus, T., Colaprete, A., & Christensen, P. (2010). Mars Global Digital Dune Database: MC–1, US Geological Survey Open-File Report 2010–1170. *US Geological Survey: Flagstaff, AZ, USA*. doi: 10.3133/ofr20101170

Head III, J. W., Hiesinger, H., Ivanov, M. A., Kreslavsky, M. A., Pratt, S., & Thomson, B. J. (1999). Possible ancient oceans on Mars: Evidence from Mars Orbiter Laser Altimeter data. *Science*, *286*(5447), 2134–2137. doi: 10.1126/science.286.5447.2134

Hepburn, A. J., Holt, T., Hubbard, B., & Ng, F. (2019). Creating HiRISE digital elevation models for Mars using the open-source Ames Stereo Pipeline. *Geoscientific Instrumentation, Methods and Data Systems*, *8*(2), 293–313. doi: 10.5194/gi-8-293-2019

Hood, D. R., Sholes, S. F., Karunatillake, S., Fassett, C. I., Ewing, R. C., & Levy, J. (2022). The Martian Boulder Automatic Recognition System, MBARS. *Earth and Space Science*, *9*(9), e2022EA002410. doi: 10.1029/2022EA002410

Horgan, B., Bell III, J., Noe Dobrea, E., Cloutis, E., Bailey, D., Craig, M., ... Mustard, J. (2009). Distribution of hydrated minerals in the north polar region of Mars. *Journal of Geophysical Research: Planets*, *114*(E1). doi: 10.1029/2008JE003187

Kieffer, H. H., Titus, T. N., Mullins, K. F., & Christensen, P. R. (2000). Mars south polar spring and summer behavior observed by TES: Seasonal cap evolution controlled by frost grain size. *Journal of Geophysical Research: Planets*, *105*(E4), 9653–9699. doi: 10.1029/1999JE001136

Laskar, J., Levrard, B., & Mustard, J. F. (2002). Orbital forcing of the Martian Polar Layered Deposits. *Nature*, *419*(6905), 375–377. doi: 10.1038/nature01066

Leighton, R. B., & Murray, B. C. (1966). Behavior of carbon dioxide and other volatiles on Mars. *Science*, *153*(3732), 136–144. doi: 10.1126/science.153.3732.136

Le Maistre, S., Rivoldini, A., Caldiero, A., Yseboodt, M., Baland, R.-m., Beuthe, M., ... Banerdt, W. B. (2023). Spin state and deep interior structure of Mars from InSight radio tracking. *Nature*, 1–5. doi: 10.1038/s41586-023-06150-0

Leys, C., Ley, C., Klein, O., Bernard, P., & Licata, L. (2013). Detecting outliers: Do not use standard deviation around the mean, use absolute deviation around the median. *Journal of Experimental Social Psychology*, *49*(4), 764–766. doi: 10.1016/j.jesp.2013.03.013

Määttänen, A., & Montmessin, F. (2021). Clouds in the Martian atmosphere. In *Oxford Research Encyclopedia of Planetary Science*. doi: 10.1093/acrefore/9780190647926.013.114

Malin, M. C., Bell, J. F., Cantor, B. A., Caplinger, M. A., Calvin, W. M., Clancy, R. T., ... Wolff, M. J. (2007). Context Camera Investigation on board the Mars Reconnaissance Orbiter. *Journal of Geophysical Research: Planets*, *112*(E5). doi: 10.1029/2006JE002808

Massé, M., Bourgeois, O., Le Mouélic, S., Verpoorter, C., Spiga, A., & Le Deit, L. (2012). Wide distribution and glacial origin of polar gypsum on Mars. *Earth and Planetary Science Letters*, *317*, 44–55.

Matsuo, K., & Heki, K. (2009). Seasonal and inter-annual changes of volume density of Martian CO_2 snow from time-variable elevation and gravity. *Icarus*, *202*(1), 90–94. doi: 10.1016/j.icarus.2009.02.023

Matthies, L., Kennett, A., Kerber, L., Fraeman, A., & Anderson, R. C. (2022). Prospects for very long-range Mars rover missions. In *2022 IEEE Aerospace Conference (AERO)* (pp. 1–11). doi: 10.1109/AERO53065.2022.9843681

McEwen, A. S. (2005). *MRO Mars High Resolution Image Science Experiment EDR V1.0*. NASA Planetary Data System. doi: 10.17189/1520179

McEwen, A. S., Eliason, E. M., Bergstrom, J. W., Bridges, N. T., Hansen, C. J., Delamere, W. A., ... Weitz, C. M. (2007). Mars Reconnaissance Orbiter's High Resolution Imaging Science Experiment (HiRISE). *Journal of Geophysical Research: Planets*, *112*(E5). doi: 10.1029/2005JE002605

McGlasson, R. A., Bramson, A. M., Morgan, G. A., & Sori, M. M. (2023). Varied histories of outlier polar ice deposits on Mars. *Journal of Geophysical Research: Planets*, e2022JE007592. doi: 10.1029/2022JE007592

Mc Keown, L., Diniega, S., Portyankina, G., Hansen, C., Aye, K., Piqueux, S., & Scully, J. E. (2023). Martian araneiforms: A review. *Journal of Geophysical Research: Planets*, *128*(4). doi: 10.1029/2022JE007684

Métivier, L., Karatekin, Ö., & Dehant, V. (2008). The effect of the internal structure of Mars on its seasonal loading deformations. *Icarus*, *194*(2), 476–486. doi: 10.1016/j.icarus.2007.12.001

Mischna, M. A., Richardson, M. I., Wilson, R. J., & McCleese, D. J. (2003). On the orbital forcing of Martian water and CO_2 cycles: A general circulation model study with simplified volatile schemes. *Journal of Geophysical Research: Planets*, *108*(E6). doi: 10.1029/2003JE002051

Mount, C. P., & Titus, T. N. (2015). Evolution of Mars' northern polar seasonal CO_2 deposits: Variations in surface brightness and bulk density. *Journal of Geophysical Research: Planets*, *120*(7), 1252–1266. doi: 10.1002/2014JE004706

Nagle-McNaughton, T. P., Williams, J. M., Gallegos, Z. E., Wilkie, H. A., Martinez, D. C., & Scuderi, L. A. (2020). Geographic information system based detection and quantification of boulders using HiRISE imagery: A case study in Jezero Crater. *Journal of Applied Remote Sensing*, *14*(1), 014522–014522. doi: 10.1117/1.JRS.14.014522

Navarro, T., Madeleine, J.-B., Forget, F., Spiga, A., Millour, E., Montmessin, F., & Määttänen, A. (2014). Global climate modeling of the Martian water cycle with improved microphysics and radiatively active water ice clouds. *Journal of Geophysical Research: Planets*, *119*(7), 1479–1495. doi: 10.1002/2013JE004550

Nerozzi, S., & Holt, J. (2019). Buried ice and sand caps at the north pole of Mars: Revealing a record of climate change in the cavi unit with SHARAD. *Geophysical Research Letters*, *46*(13), 7278–7286. doi: 10.1029/2019GL082114

Nerozzi, S., Ortiz, M. R., & Holt, J. W. (2022). The north polar basal unit of Mars: An Amazonian record of surface processes and climate events. *Icarus*, *373*, 114716. doi: 10.1016/j.icarus.2021.114716

Neukum, G., & Jaumann, R. (2004). HRSC: The high resolution stereo camera of Mars Express. In *Mars Express: The Scientific Payload* (Vol. 1240, pp. 17–35).

Neumann, G. A., Abshire, J. B., Aharonson, O., Garvin, J. B., Sun, X., & Zuber, M. T. (2003). Mars Orbiter Laser Altimeter pulse width measurements and footprint-scale roughness. *Geophysical Research Letters*, *30*(11), 1561. doi: 10.1029/2003GL017048

Neumann, G. A., Rowlands, D. D., Lemoine, F. G., Smith, D. E., & Zuber, M. T. (2001). Crossover analysis of Mars Orbiter Laser Altimeter data. *Journal of Geophysical Research: Planets*, *106*(E10), 23753–23768. doi: 10.1029/2000JE001381

Ojha, L., Nerozzi, S., & Lewis, K. (2019). Compositional constraints on the north polar cap of Mars from gravity and topography. *Geophysical Research Letters*, *46*(15), 8671–8679. doi: 10.1029/2019GL082294

Piqueux, S., Kleinböhl, A., Hayne, P. O., Kass, D. M., Schofield, J. T., & McCleese, D. J. (2015). Variability of the Martian seasonal CO_2 cap extent over eight Mars Years. *Icarus*, *251*, 164–180. doi: 10.1016/j.icarus.2014.10.045

Plaut, J. J., Picardi, G., Safaeinili, A., Ivanov, A. B., Milkovich, S. M., Cicchetti, A., ... Edenhofer, P. (2007). Subsurface radar sounding of the South Polar Layered Deposits of Mars. *Science*, *316*(5821), 92–95. doi: 10.1126/science.1139672

Pommerol, A., Appéré, T., Portyankina, G., Aye, K.-M., Thomas, N., & Hansen, C. (2013). Observations of the northern seasonal polar cap on Mars III: CRISM/HiRISE observations of spring sublimation. *Icarus*, *225*(2), 911–922. doi: 10.1016/j.icarus.2012.08.039

Portyankina, G., Markiewicz, W. J., Thomas, N., Hansen, C. J., & Milazzo, M. (2010). HiRISE

observations of gas sublimation-driven activity in Mars' southern polar regions: III. Models of processes involving translucent ice. *Icarus*, *205*(1), 311–320. doi: 10.1016/j.icarus.2009.08.029

Raguso, M., & Nunes, D. (2021). Monitoring of CO_2 seasonal variations at the Martian polar ice caps using SHARAD data. In *Lunar and Planetary Science Conference* (p. 2438).

Russell, P., Byrne, S., & Hansen, C. J. (2010). Active mass wasting of ice layers and seasonal CO_2 frost in the north polar region of Mars. In *Lunar and Planetary Science Conference*.

Russell, P., Byrne, S., Pathare, A., & Herkenhoff, K. (2012). Active erosion and evolution of Mars north polar scarps. In *Lunar and Planetary Science Conference* (p. 2747).

Russell, P., Thomas, N., Byrne, S., Herkenhoff, K., Fishbaugh, K., Bridges, N., ... Alfred, M. (2008). Seasonally active frost-dust avalanches on a north polar scarp of Mars captured by HiRISE. *Geophysical Research Letters*, *35*(23). doi: 10.1029/2008GL035790

Schmidt, F., Douté, S., Schmitt, B., Vincendon, M., Bibring, J.-P., Langevin, Y., & the OMEGA Team. (2009). Albedo control of Seasonal South Polar Cap recession on Mars. *Icarus*, *200*(2), 374–394. doi: 10.1016/j.icarus.2008.12.014

Schmidt, F., & Portyankina, G. (2018). The exotic processes driving ephemeral seasonal surface change on Mars. In *Dynamic Mars: Recent and current landscape evolution of the Red Planet* (pp. 157–186). Elsevier. doi: 10.1016/B978-0-12-813018-6.00005-4

Schmidt, F., Way, M. J., Costard, F., Bouley, S., Séjourné, A., & Aleinov, I. (2022). Circumpolar ocean stability on Mars 3 Gy ago. *Proceedings of the National Academy of Sciences*, *119*(4), e2112930118. doi: 10.1073/pnas.2112930118

Silverman, B. W. (1986). *Density estimation for statistics and data analysis* (Vol. 26). CRC press.

Smith, D. E., Zuber, M. T., & Neumann, G. A. (2001). Seasonal variations of snow depth on Mars. *Science*, *294*(5549), 2141–2146. doi: 10.1126/science.1066556

Smith, I. B., Hayne, P. O., Byrne, S., Becerra, P., Kahre, M., Calvin, W., ... Siegler, M. (2020). The Holy Grail: A road map for unlocking the climate record stored within Mars' Polar Layered Deposits. *Planetary and Space Science*, *184*(May 2019). doi: 10.1016/j.pss.2020.104841

Sori, M. M., Becerra, P., Bapst, J., Byrne, S., & McGlasson, R. A. (2022). Orbital forcing of Martian climate revealed in a south polar outlier ice deposit. *Geophysical Research Letters*, *49*(6), e2021GL097450. doi: 10.1029/2021GL097450

Sori, M. M., Byrne, S., Hamilton, C. W., & Landis, M. E. (2015). Viscous flow rates of icy topography on the North Polar Layered Deposits of Mars. *Geophysical Research Letters*, *43*(2), 541-549. doi: 10.1002/2015GL067298

Stark, A., Oberst, J., Preusker, F., Gwinner, K., Peale, S. J., Margot, J.-L., ... Solomon, S. C. (2015). Mercury's rotational parameters from MESSENGER image and laser altimeter data: A feasibility study. *Planetary and Space Science*, *117*, 64–72. doi: 10.1016/j.pss.2015.05.006

Steinbrügge, G., Haynes, M. S., Schroeder, D. M., Scanlan, K. M., Stark, A., Young, D. A., ... Blankenship, D. D. (2021). Altimetry measurements from planetary radar sounders and application to SHARAD on Mars. *IEEE Transactions on Geoscience and Remote Sensing*. doi: 10.1109/TGRS.2021.3134638

Su, S., Fanara, L., Xiao, H., Hauber, E., & Oberst, J. (2023). Detection of detached ice-fragments at Martian polar scarps using a Convolutional Neural Network. *IEEE Journal of Selected Topics in Applied Earth Observations and Remote Sensing*. doi: 10.1109/JSTARS.2023.3238968

Su, S., Fanara, L., Zhang, X., Hauber, E., Gwinner, K., & Oberst, J. (2023). Searching for the sources of ice block falls at the Martian north polar scarps. *Icarus*, *390*, 115321. doi: 10.1016/j.icarus.2022.115321

Thomas, N., Cremonese, G., Ziethe, R., Gerber, M., Brändli, M., Bruno, G., ... Wray, J. J. (2017). The Colour and Stereo Surface Imaging System (CaSSIS) for the ExoMars Trace Gas Orbiter. *Space Science Reviews*, *212*(3), 1897–1944. doi: 10.1007/s11214-017-0421-1

Thomas, P. C., Calvin, W., Cantor, B., Haberle, R., James, P. B., & Lee, S. W. (2016). Mass balance of Mars' residual south polar cap from CTX images and other data. *Icarus*, *268*, 118–130. doi: 10.1016/j.icarus.2015.12.038

Van den Acker, E., Van Hoolst, T., de Viron, O., Defraigne, P., Forget, F., Hourdin, F., & Dehant, V. (2002). Influence of the seasonal winds and the CO_2 mass exchange between atmosphere and polar caps on mars' rotation. *Journal of Geophysical Research: Planets*, *107*(E7), 9–1. doi: 10.1029/2000JE001539

Wagner, N. L., James, P. B., Ermakov, A. E., & Sori, M. M. (2023). Evaluating the use of seasonal surface displacements and time-variable gravity to constrain the interior of Mars. In *Authorea*. doi: 10.22541/essoar.169230247.71360068/v1

Wang, H., & Ingersoll, A. P. (2002). Martian clouds observed by Mars Global Surveyor Mars Orbiter Camera. *Journal of Geophysical Research: Planets*, *107*(E10), 8–1. doi: 10.1029/2001JE001815

Xiao, H., Stark, A., Schmidt, F., Hao, J., Steinbrügge, G., Wagner, N. L., ... Oberst, J. (2022). Spatio-temporal level variations of the Martian Seasonal North Polar Cap from co-registration of MOLA profiles. *Journal of Geophysical Research: Planets*, *127*(10), e2021JE007158. doi: 10.1029/2021JE007158

Xiao, H., Stark, A., Schmidt, F., Hao, J., Steinbrügge, G., Cheng, Y., & Oberst, J. (2021). Spatio-temporal level variations of the Martian Seasonal North Polar Cap. *Mendeley Data*. doi: 10.17632/x953mzxxvv.1

Xiao, H., Stark, A., Schmidt, F., Hao, J., Su, S., Steinbrügge, G., & Oberst, J. (2022). Spatio-temporal level variations of the Martian Seasonal South Polar Cap from co-registration of MOLA profiles. *Journal of Geophysical Research: Planets*, e2022JE007196. doi: 10.1029/2022JE007196

Xiao, H., Stark, A., Steinbrügge, G., Hussmann, H., & Oberst, J. (2021). Processing of laser altimeter Time-of-Flight measurements to geodetic coordinates. *Journal of Geodesy*. doi: 10.1007/s00190-020-01467-4

Xiao, H., Stark, A., Steinbrügge, G., Thor, R., Schmidt, F., & Oberst, J. (2022). Prospects for mapping temporal height variations of the seasonal CO_2 snow/ice caps at the Martian poles by co-registration of MOLA Profiles. *Planetary and Space Science*, *214C*. doi: 10.1016/j.pss.2022.105446

Zurek, R., Campbell, B., Byrne, S., Calvin, W., Carter, L., Clancy, R., ... Pratt, L. (2021). Mars Next Orbiter Science Analysis Group (NEX-SAG): White Paper Report to the 2023-2032 Planetary Sciences and Astrobiology Decadal Survey. *Bulletin of the American Astronomical Society*, *53*(4), 038.

Figure 1.

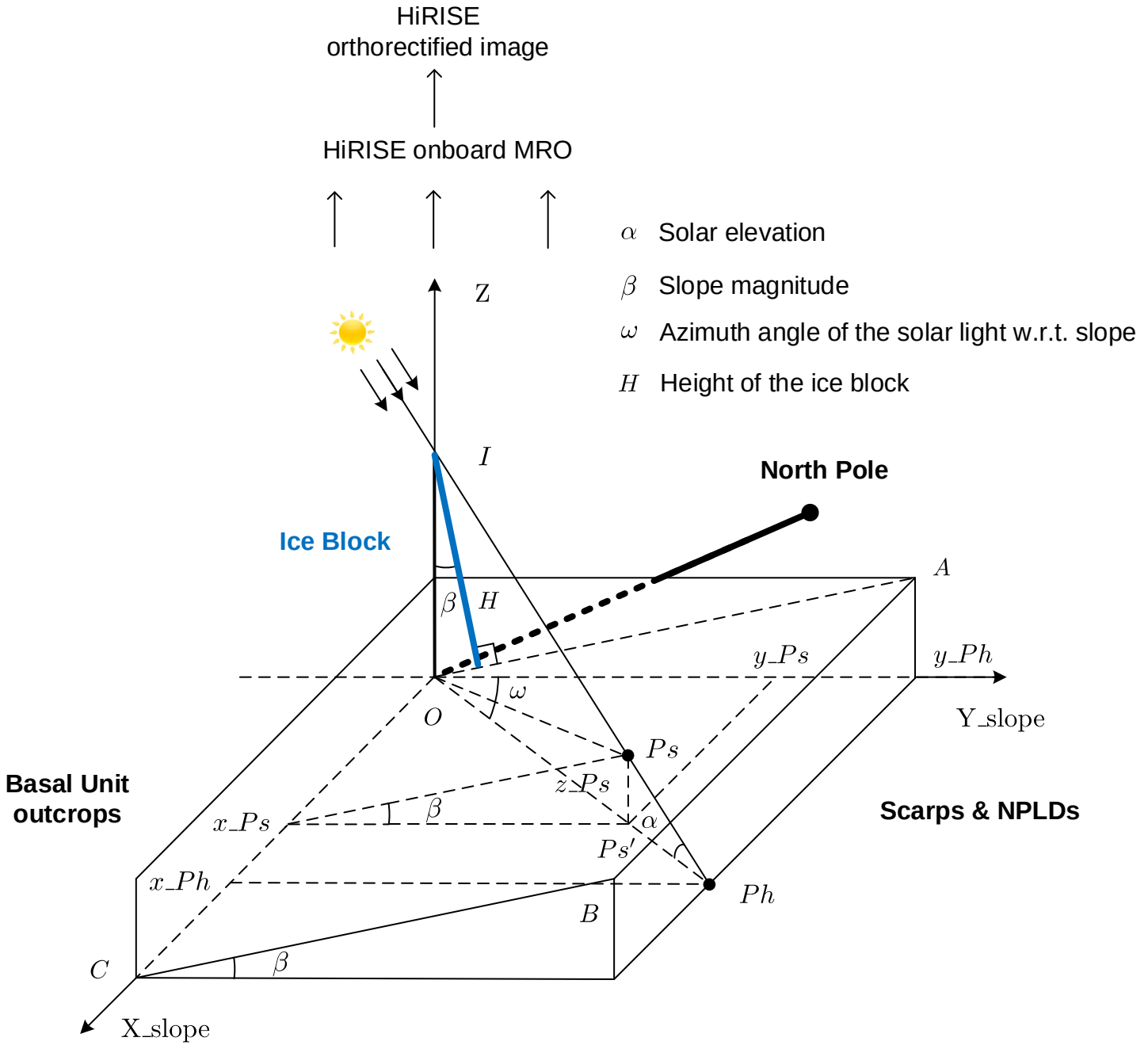
HiRISE
orthorectified image
HiRISE onboard MRO
α Solar elevation
β Slope magnitude
ω Azimuth angle of the solar light w.r.t. slope
H Height of the ice block
Z
I
North Pole
Ice Block
A
β H
y_Ps
y_Ph
ω
O
Y_slope
Ps
z_Ps
Basal Unit
outcrops
x_Ps
β
α
Scarps & NPLDs
Ps'
x_Ph
Ph
B
C
β
X_slope

Figure 2.

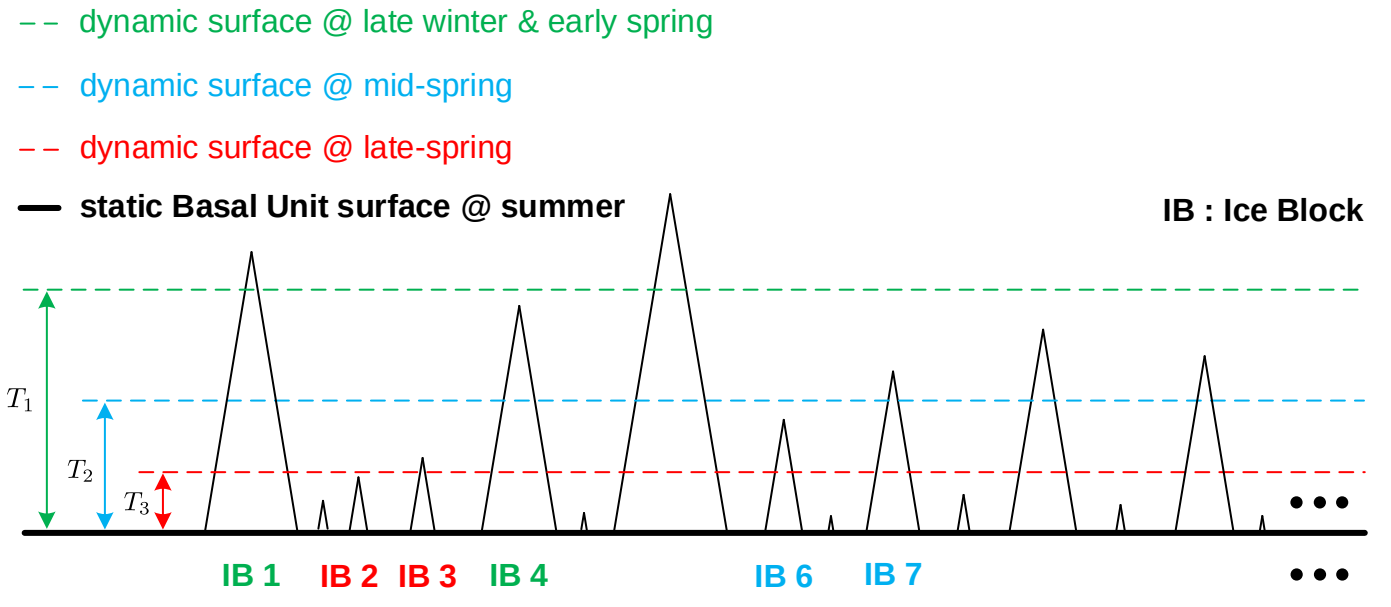
dynamic surface @ late winter & early spring
dynamic surface @ mid-spring
dynamic surface @ late-spring
static Basal Unit surface @ summer
IB : Ice Block
T_1
T_2
T_3
IB 1
IB 2
IB 3
IB 4
IB 6
IB 7

Figure 3.

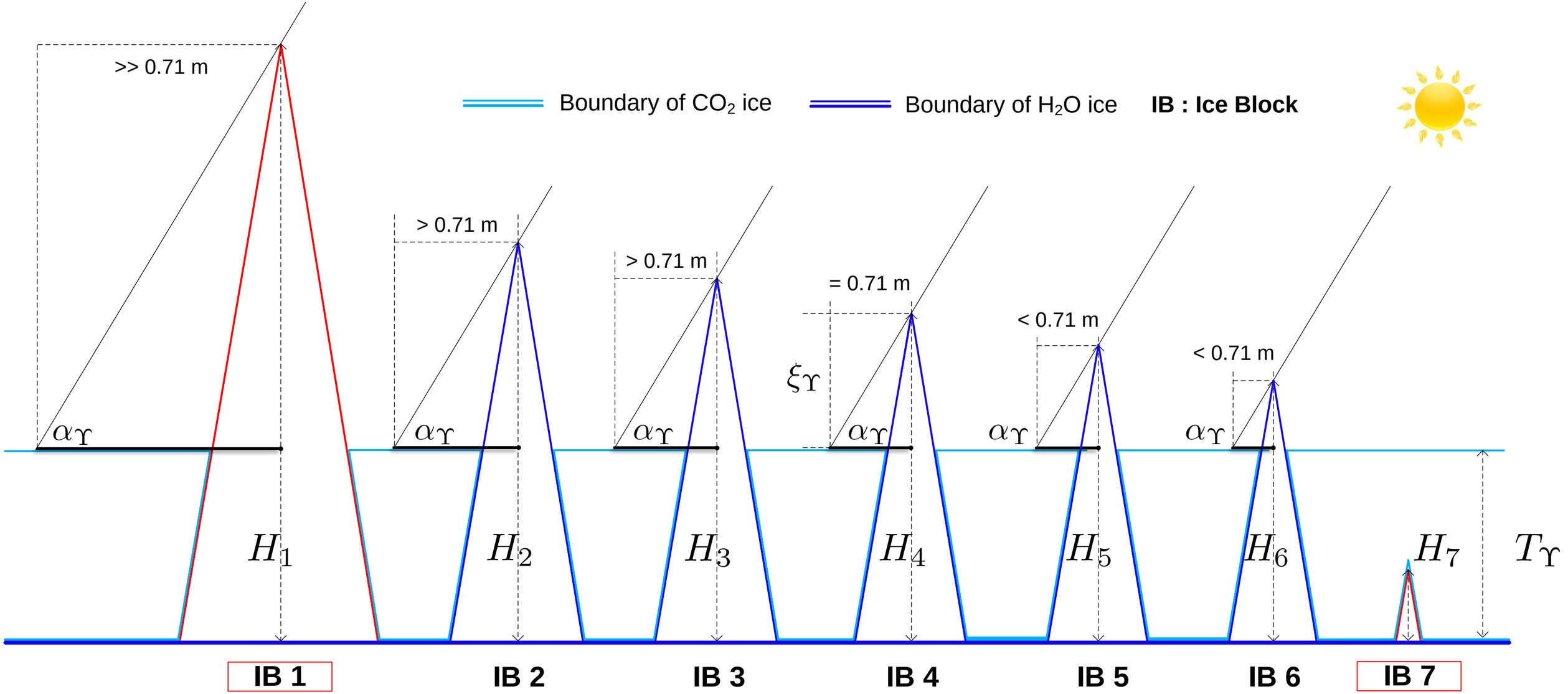
>> 0.71 m
Boundary of CO_2 ice
Boundary of H_2O ice
IB : Ice Block
> 0.71 m
> 0.71 m
= 0.71 m
< 0.71 m
< 0.71 m
$\alpha\Upsilon$
$\xi\Upsilon$
H_1
H_2
H_3
H_4
H_5
H_6
H_7
$T\Upsilon$
IB 1
IB 2
IB 3
IB 4
IB 5
IB 6
IB 7

Figure 4.

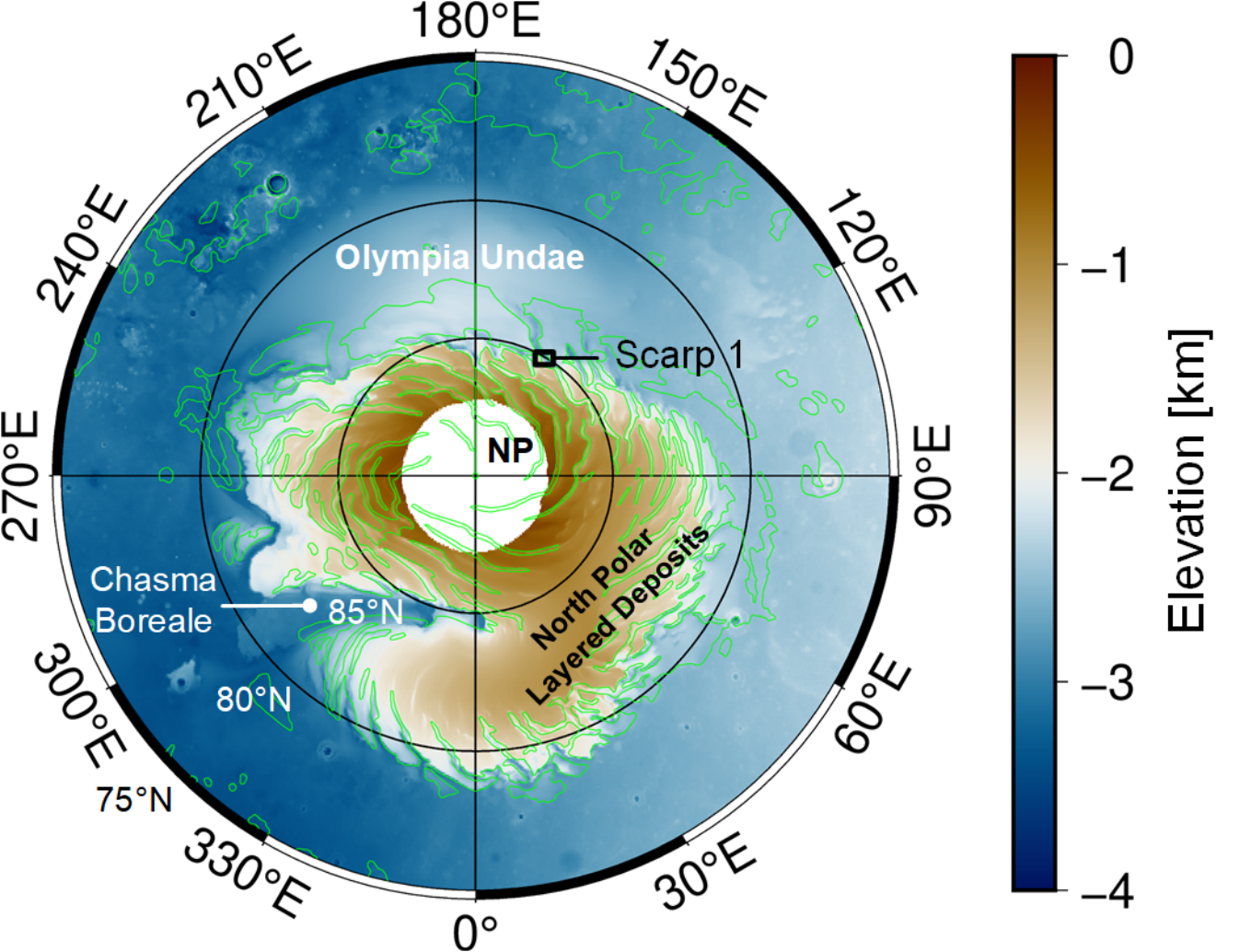
180°E
210°E
150°E
240°E
120°E
270°E
90°E
300°E
60°E
330°E
30°E
0°
Olympia Undae
Scarp 1
NP
Chasma
Boreale
85°N
80°N
75°N
North Polar
Layered Deposits
0
−1
−2
−3
−4
Elevation [km]

Figure 5.

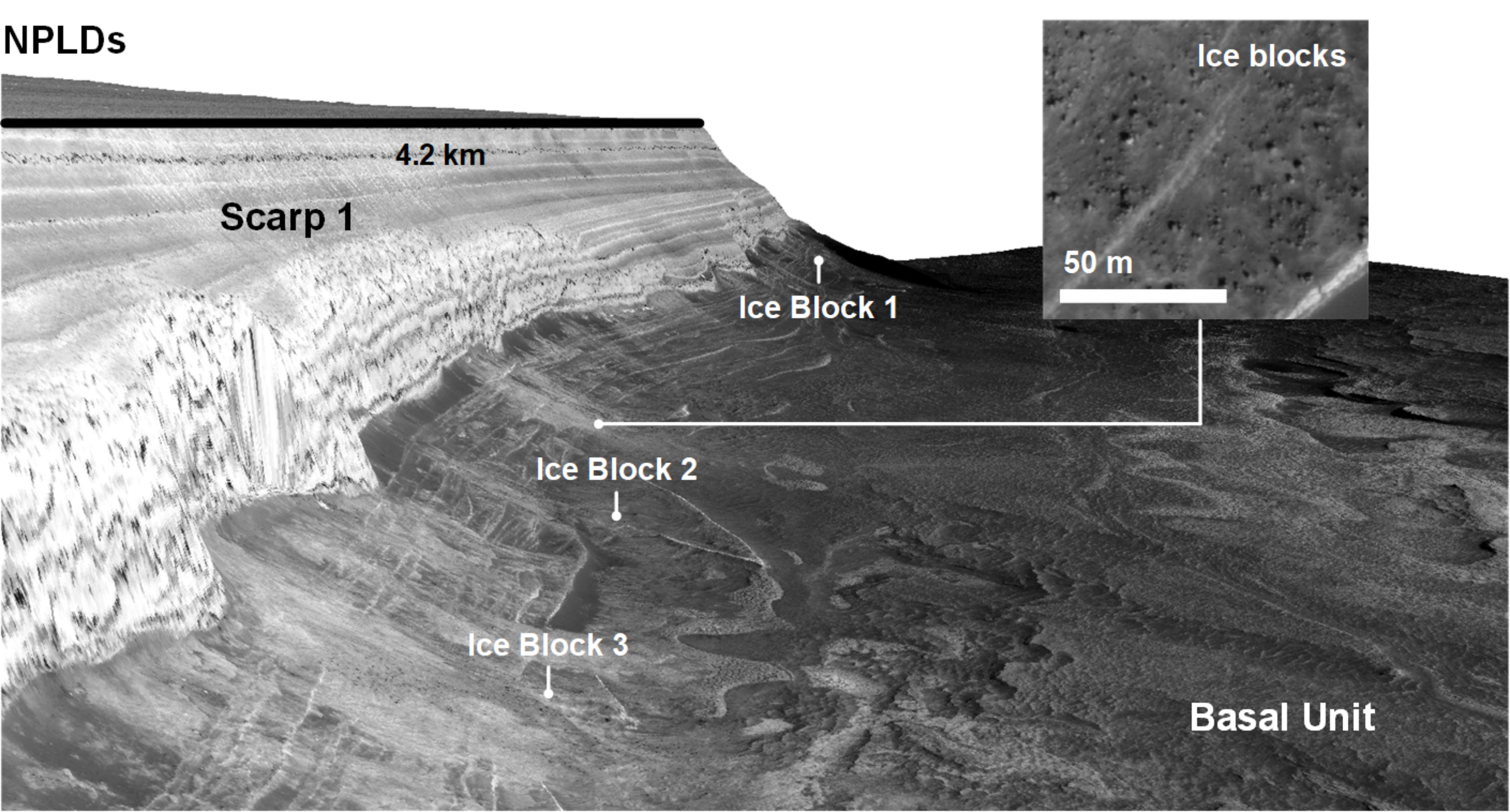
NPLDs
4.2 km
Scarp 1
Ice blocks
50 m
Ice Block 1
Ice Block 2
Ice Block 3
Basal Unit

Figure 6.

late winter | early spring | mid-to-late spring | summer

Ice Block 1

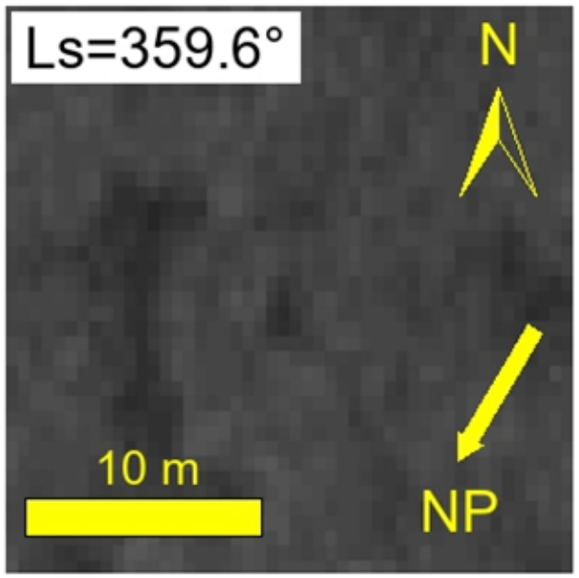

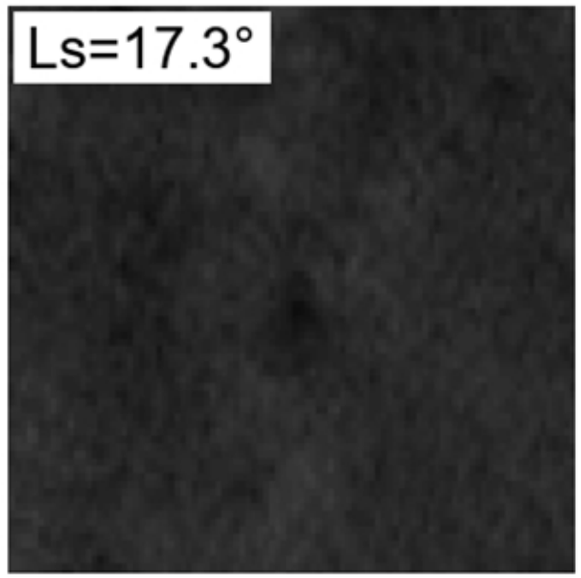

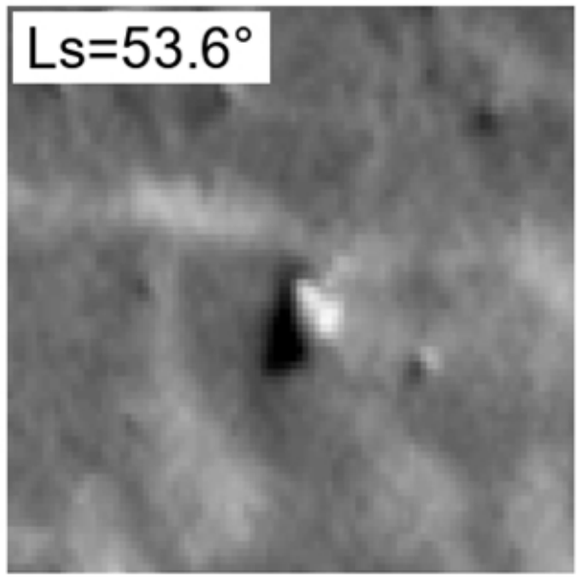

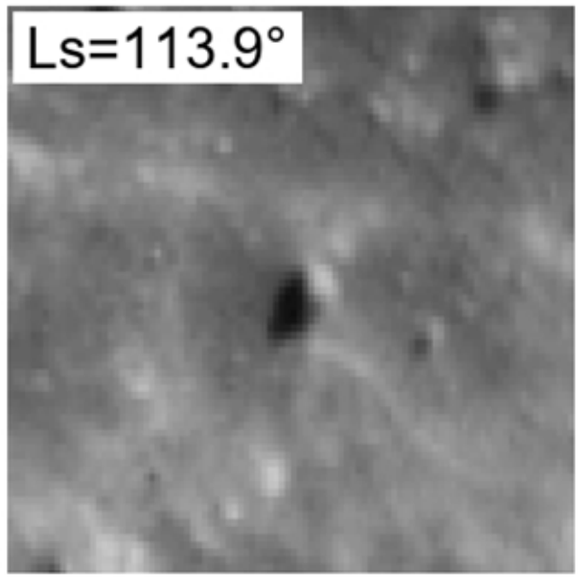

Ice Block 2

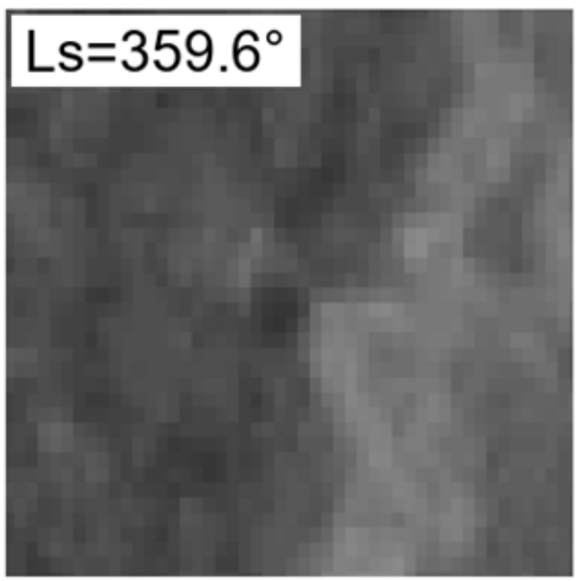

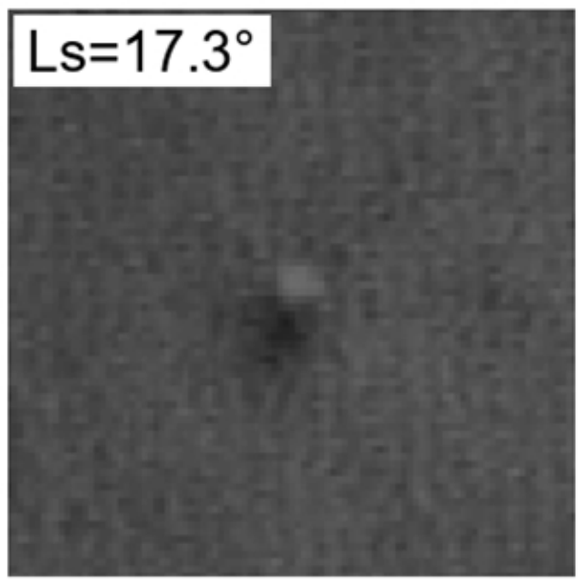

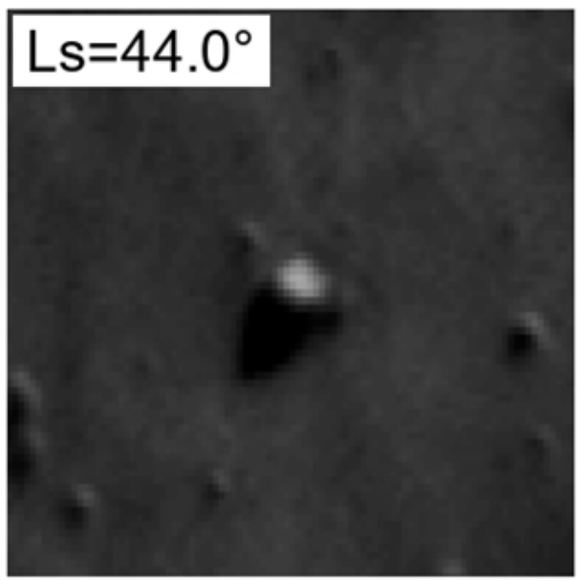

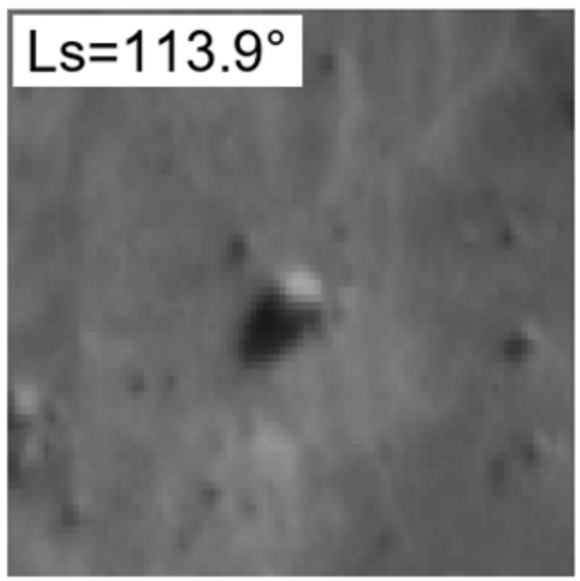

Ice Block 3

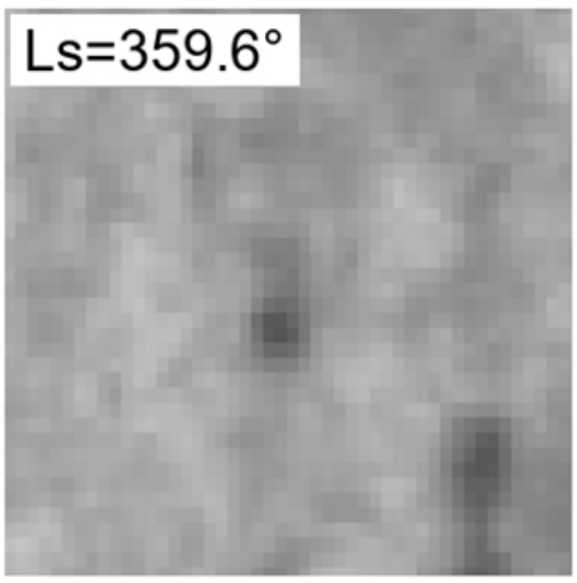

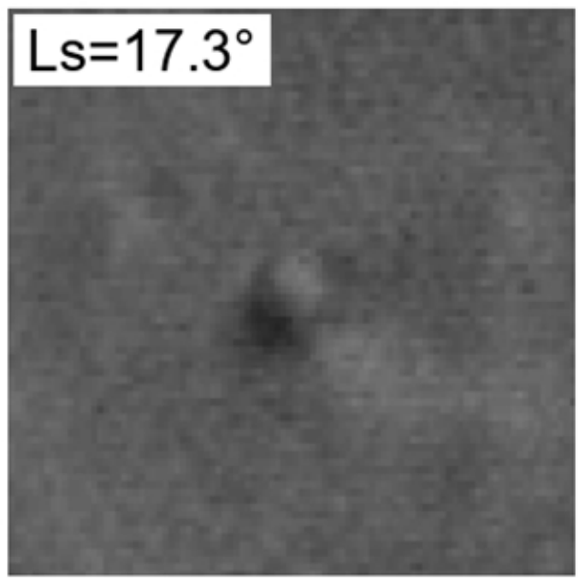

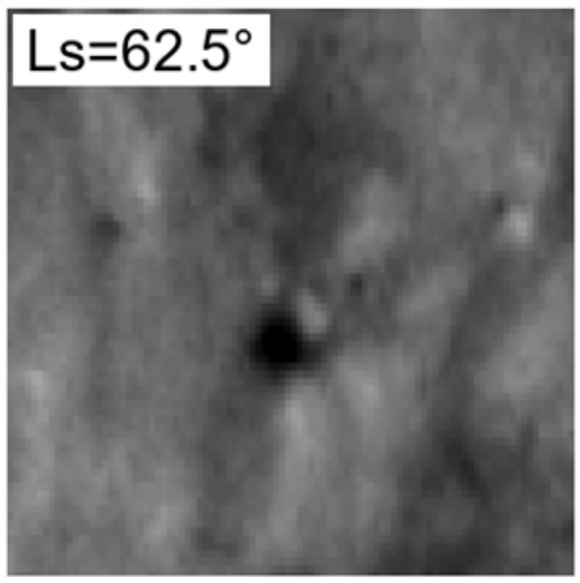

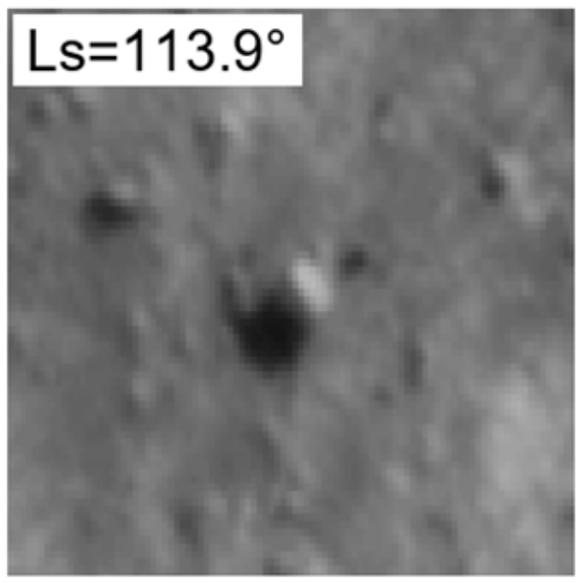

Figure 7.

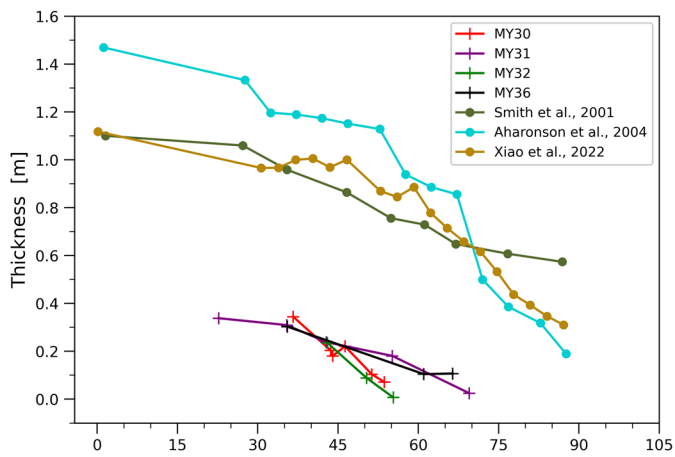
Thickness [m]
MY30
MY31
MY32
MY36
Smith et al., 2001
Aharonson et al., 2004
Xiao et al., 2022

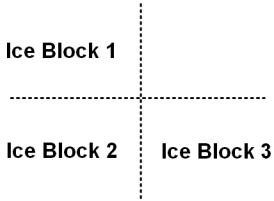
Ice Block 1
Ice Block 2
Ice Block 3

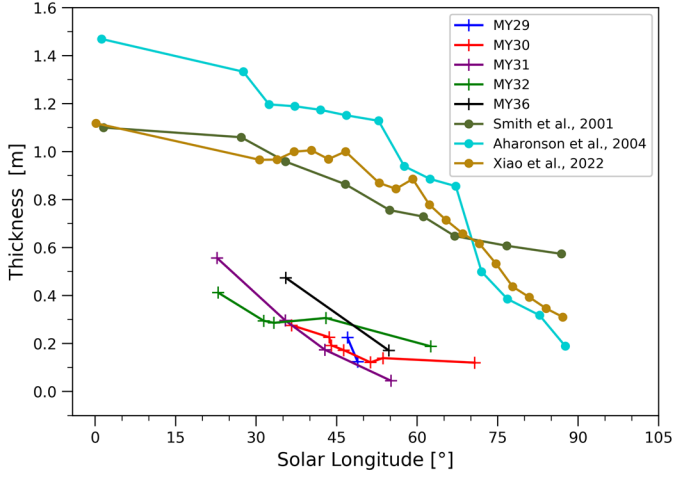
Thickness [m]
Solar Longitude [°]
MY29
MY30
MY31
MY32
MY36
Smith et al., 2001
Aharonson et al., 2004
Xiao et al., 2022

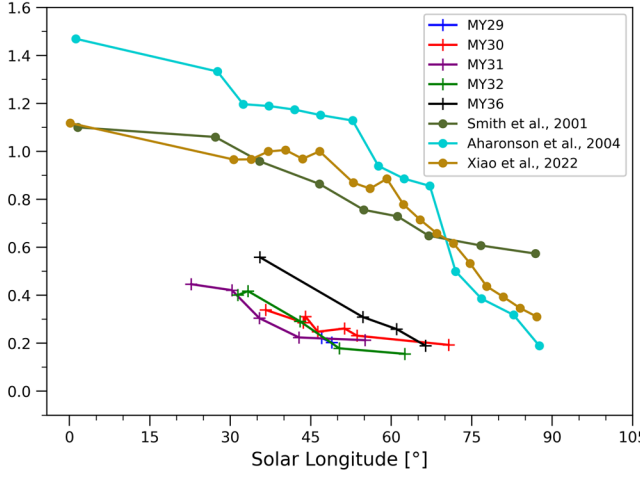
Solar Longitude [°]
MY29
MY30
MY31
MY32
MY36
Smith et al., 2001
Aharonson et al., 2004
Xiao et al., 2022

Figure 8.

Ice blocks fully covered

Ice blocks NOT fully covered

early spring

summer

early spring

summer

Ice Block Ib1

Ice Block ub1

Ice Block Ib2

Ice Block ub2

Ice Block Ib3

Ice Block ub3

Ls=7.0°

Ls=128.3°

Ls=7.0°

Ls=128.3°

Ls=7.0°

Ls=128.3°

Ls=7.0°

Ls=128.3°

Ls=7.0°

Ls=128.3°

Ls=7.0°

Ls=128.3°

N

NP

10 m

Figure 9.

Ice blocks fully covered

Ice blocks NOT fully covered

middle spring

summer

middle spring

summer

Ice Block Ib4

Ice Block ub4

Ice Block Ib5

Ice Block ub5

Ice Block Ib6

Ice Block ub6

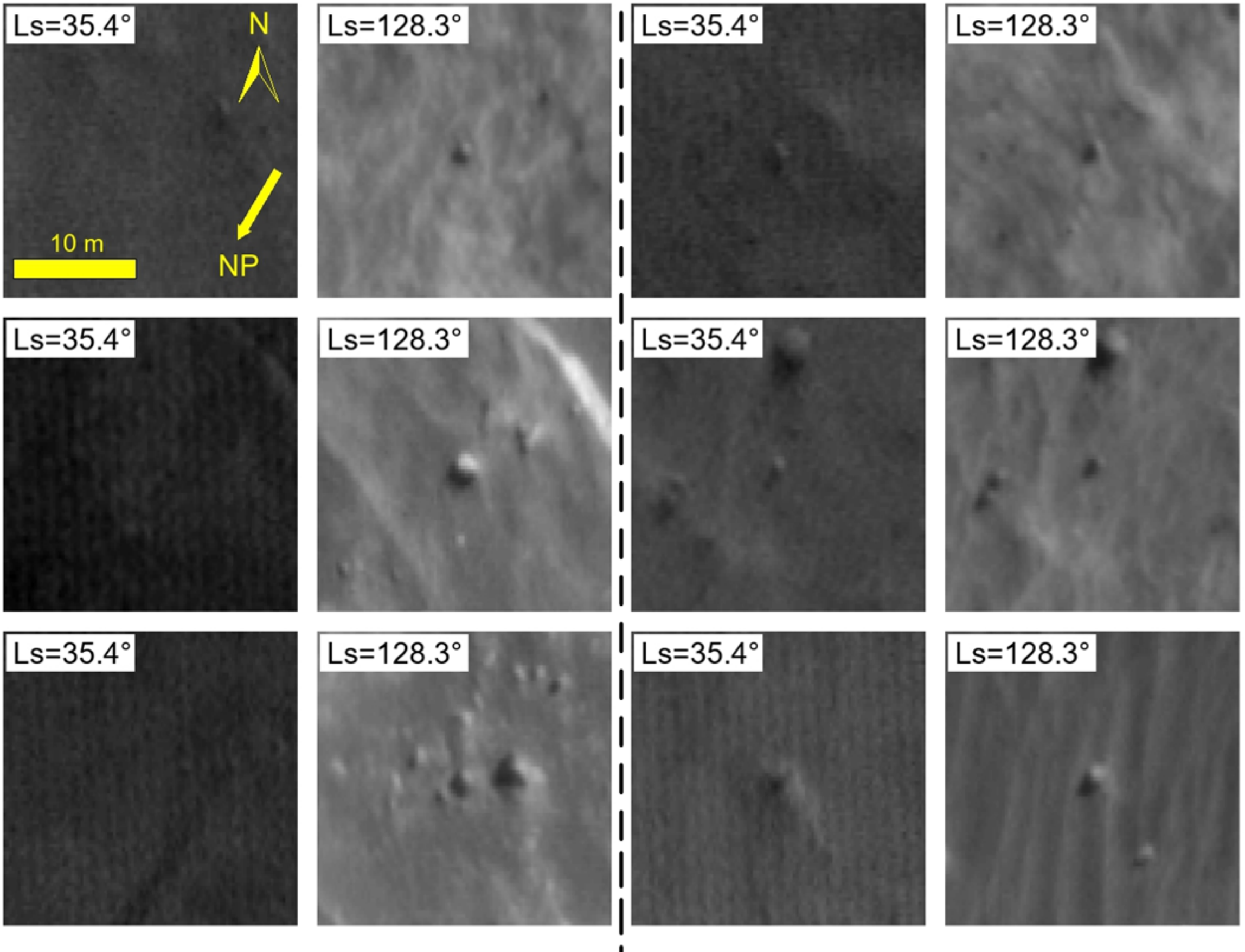

Figure 10.

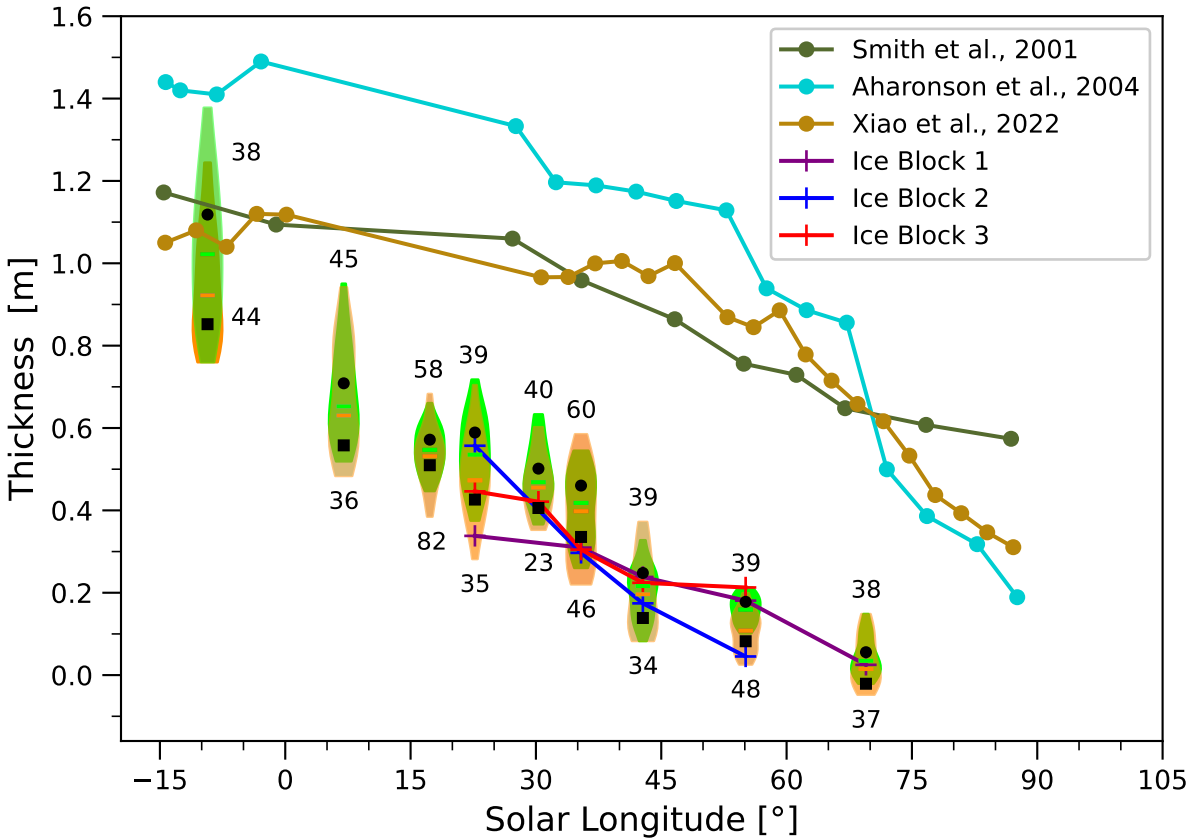
Smith et al., 2001
Aharonson et al., 2004
Xiao et al., 2022
Ice Block 1
Ice Block 2
Ice Block 3
Thickness [m]
Solar Longitude [°]
1.6
1.4
1.2
1.0
0.8
0.6
0.4
0.2
0.0
−15
0
15
30
45
60
75
90
105
38
44
45
36
58
82
39
35
40
23
60
46
39
34
39
48
38
37

Figure 11.

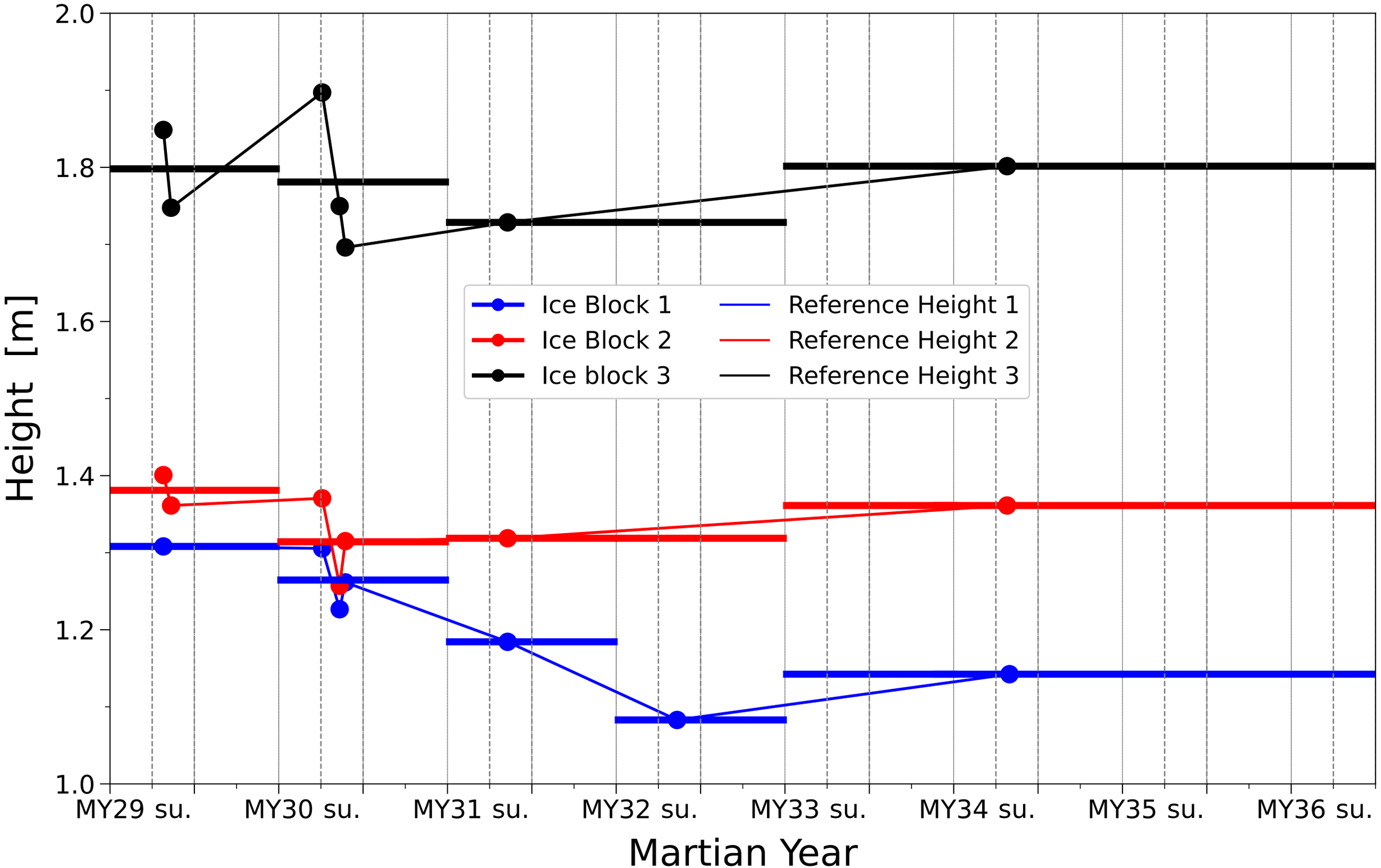
2.0
1.8
1.6
1.4
1.2
1.0
Height [m]
MY29 su.
MY30 su.
MY31 su.
MY32 su.
MY33 su.
MY34 su.
MY35 su.
MY36 su.
Martian Year
Ice Block 1
Ice Block 2
Ice block 3
Reference Height 1
Reference Height 2
Reference Height 3

Figure 12.

Smith et al., 2001
Aharonson et al., 2004
Xiao et al., 2022
38
44
19
45
22
21
58
24
36
82
MY31
MY36
MY31
MY32
MY31
Thickness [m]
Solar Longitude [°]
1.6
1.4
1.2
1.0
0.8
0.6
0.4
0.2
0.0
−15
0
15
30
45
60
75
90
105

Figure 13.

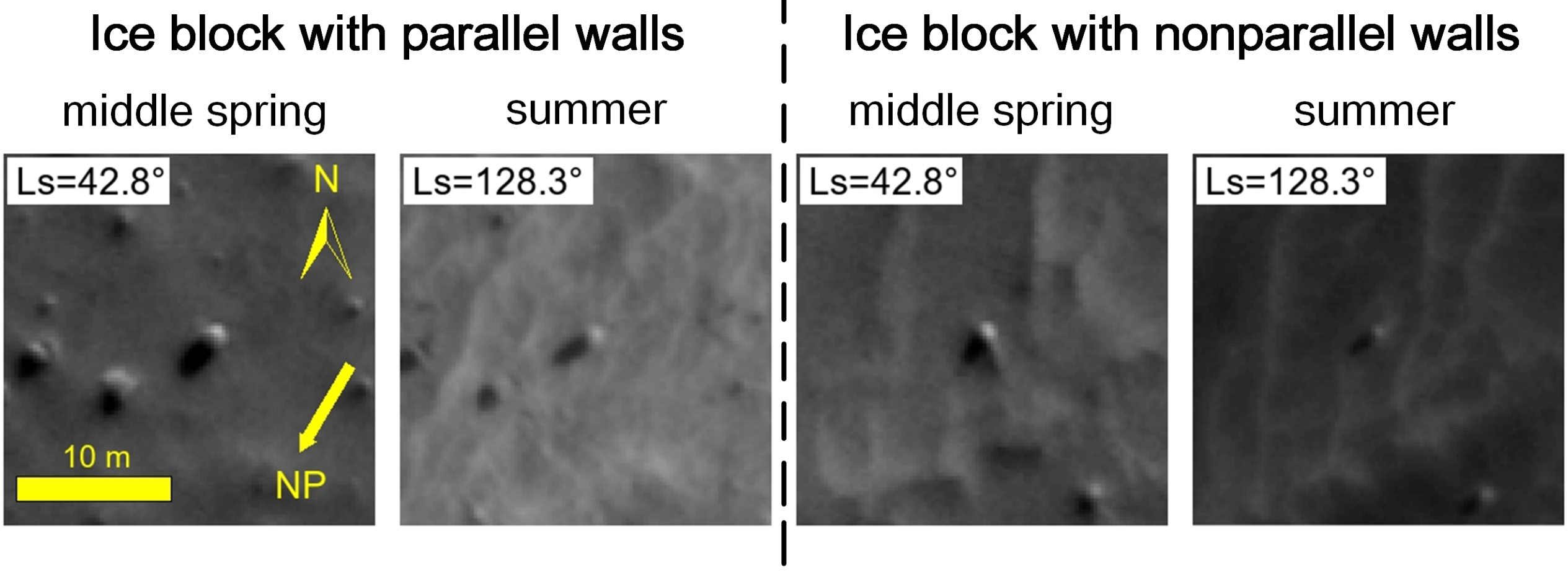
Ice block with parallel walls
Ice block with nonparallel walls
middle spring
summer
middle spring
summer
Ls=42.8°
N
Ls=128.3°
Ls=42.8°
Ls=128.3°
10 m
NP

Figure 14.

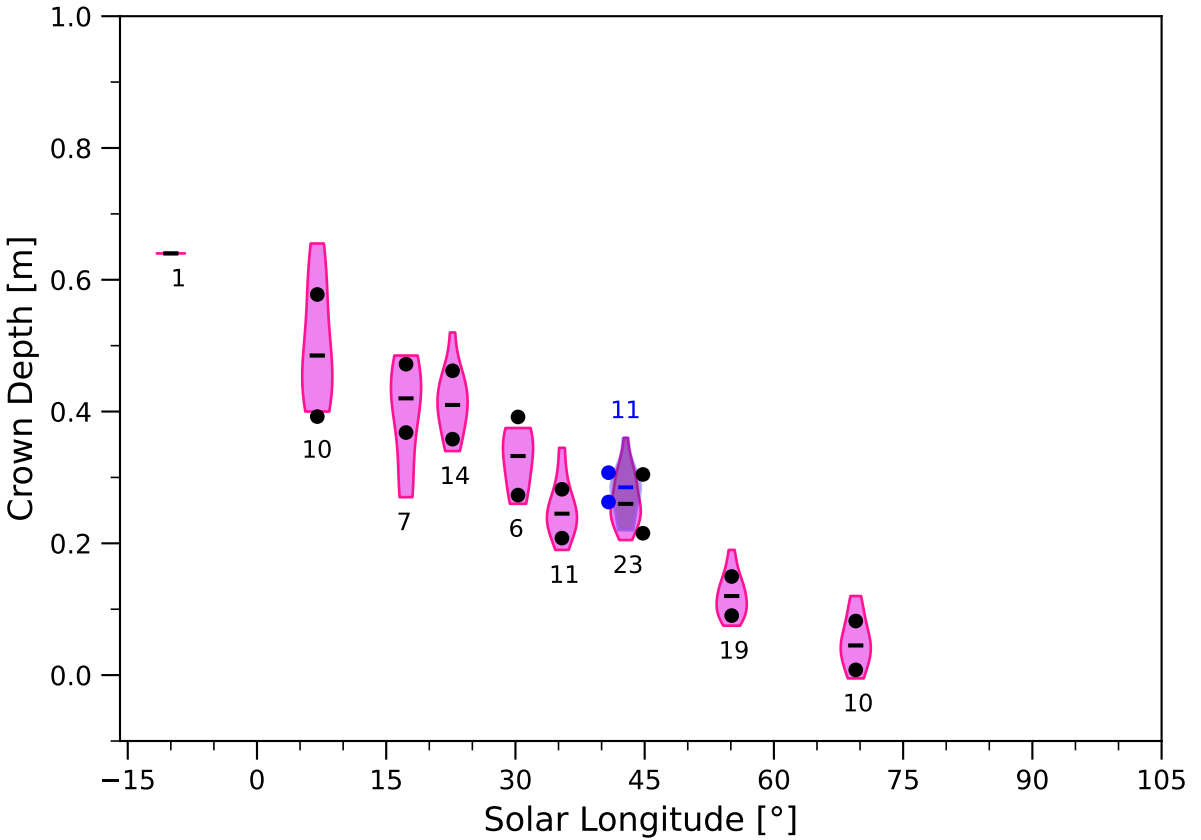
1.0
0.8
0.6
0.4
0.2
0.0
Crown Depth [m]
1
10
7
14
6
11
11
23
19
10
−15
0
15
30
45
60
75
90
105
Solar Longitude [°]

Figure 15.

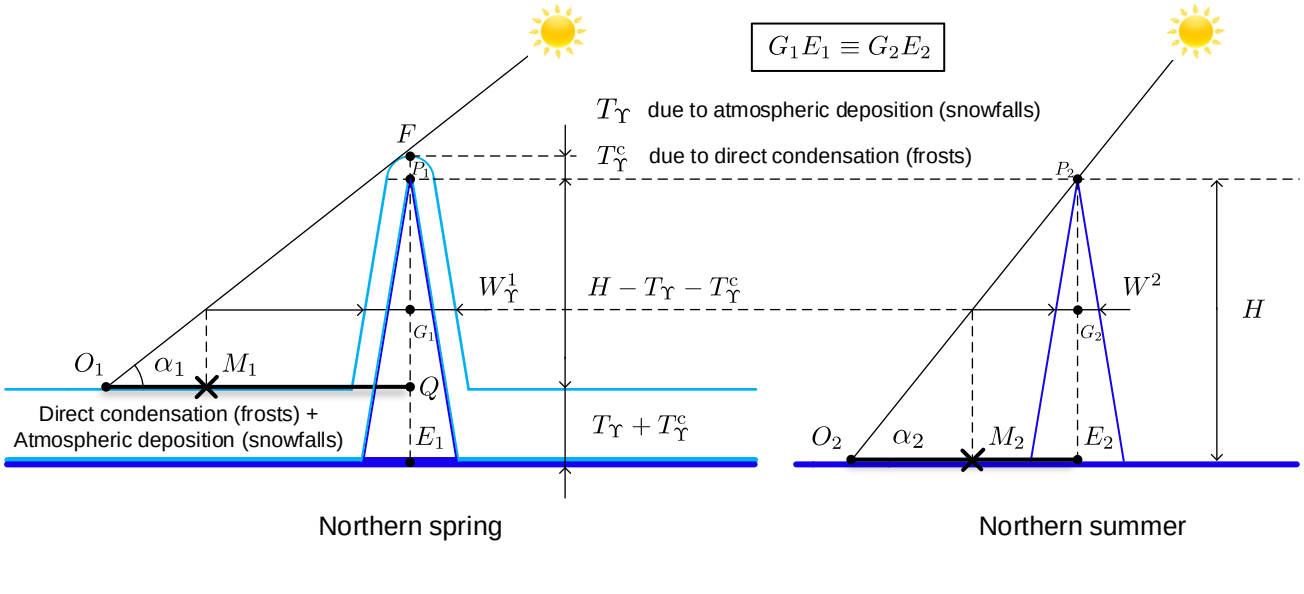
$G_1E_1 \equiv G_2E_2$
T_Υ due to atmospheric deposition (snowfalls)
T_Υ^c due to direct condensation (frosts)
F
P_1
P_2
W_Υ^1
$H - T_\Upsilon - T_\Upsilon^c$
W^2
H
G_1
G_2
O_1
α_1
M_1
Q
Direct condensation (frosts) +
Atmospheric deposition (snowfalls)
E_1
$T_\Upsilon + T_\Upsilon^c$
O_2
α_2
M_2
E_2
Northern spring
Northern summer
Boundary of CO_2 ice
Boundary of H_2O ice
Shadow width measuring point

Figure 16.

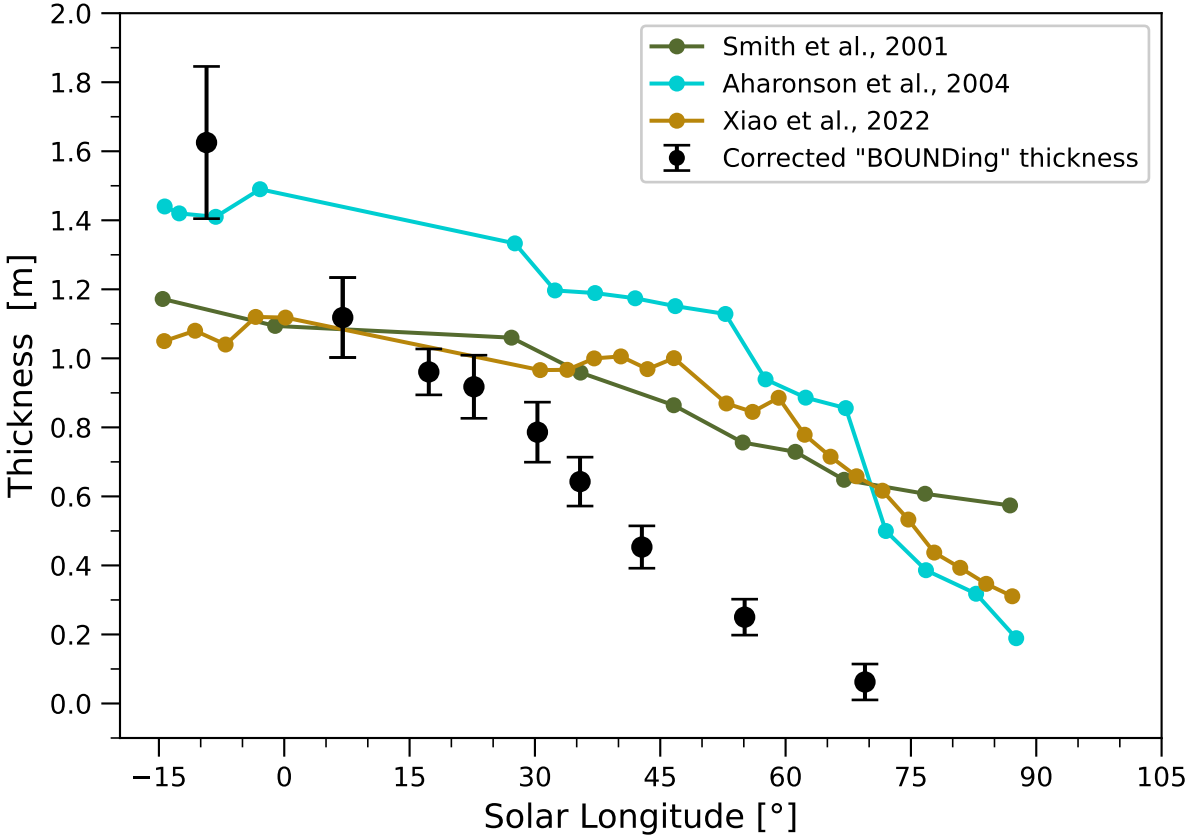
Smith et al., 2001
Aharonson et al., 2004
Xiao et al., 2022
Corrected "BOUNDing" thickness
Thickness [m]
Solar Longitude [°]
2.0
1.8
1.6
1.4
1.2
1.0
0.8
0.6
0.4
0.2
0.0
−15
0
15
30
45
60
75
90
105

Figure 17.

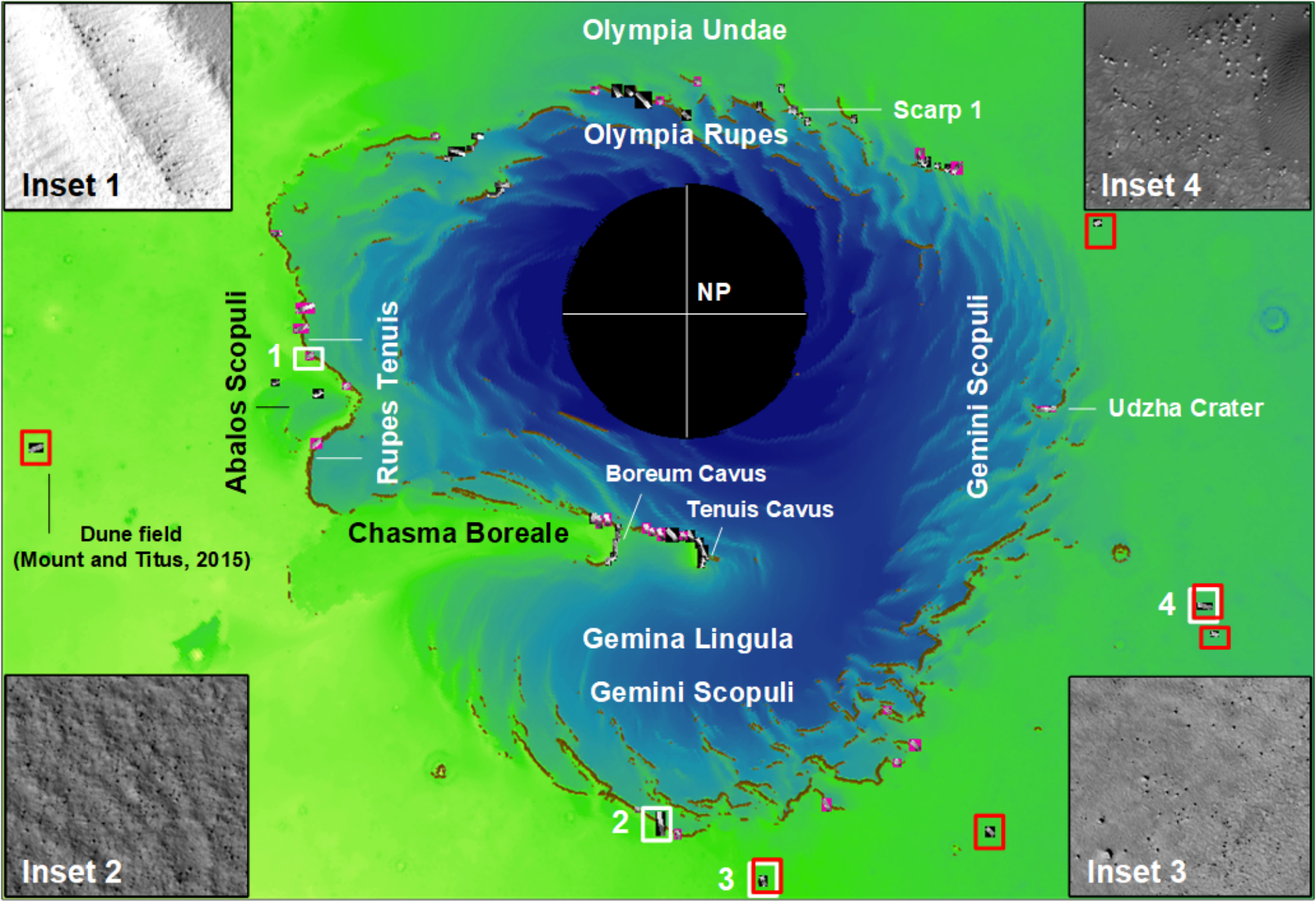
Olympia Undae
Scarp 1
Olympia Rupes
Inset 1
Inset 4
NP
Abalos Scopuli
Rupes Tenuis
Gemini Scopuli
Udzha Crater
1
Boreum Cavus
Tenuis Cavus
Chasma Boreale
Dune field
(Mount and Titus, 2015)
4
Gemina Lingula
Gemini Scopuli
2
3
Inset 2
Inset 3